A Computational Physiology Approach to Understanding Cerebrospinal Fluid and Solute Dynamics in the Central Nervous System

Dissertation

zur

Erlangung der naturwissenschaftlichen Doktorwürde
(Dr. sc. nat.)

vorgelegt der

Mathematisch-naturwissenschaftlichen Fakultät

der

Universität Zürich

von

Mahdi Asgari

aus

dem Iran

Promotionskommission

Prof. Dr. Vartan Kurtcuoglu (Leitung der Dissertation)

Prof. Dr. Sebastian Kozerke

Dr. Aldo Ferrari

Zürich, 2017

Abstract

Homeostasis of the central nervous system (CNS) is critically dependent on cerebrospinal and interstitial fluid dynamics and therewith associated transport processes. While our understanding of these processes relies heavily on in vivo tracer experiments and cerebrospinal fluid (CSF) protein analysis, interpretation of the corresponding data is far from trivial, challenged by the number of transport pathways and unknown underlying transport mechanisms. In the framework of this thesis, we have developed as well as applied computational techniques to shed light on the physiological mechanisms underlying the observed solute distributions, and to advance our understanding of CNS solutes dynamics. In vivo observations of rapid tracer transport along the cerebral paravascular spaces (PVS) have led to the hypothesis of a fast clearance system driven by bulk flow. We demonstrate that this so-called glymphatic system would require substantial intracellular water flux through a network of astrocytes maintained by a thus far unknown driving force. We further show that arterial pulsations alone are not sufficient to generate this force. However, even in the absence of a net force and directed bulk flow, pulsations of the arterial wall and thereby generated periodic fluid motion still enhance transport in the PVS via dispersion. Such a mechanism may reconcile various tracer studies that have thus far been considered contradictory. Finally, we show that pathological alterations in CSF protein content may be related both to alterations of the blood-CSF barrier and CSF dynamics, with potential implications for the treatment of neurological disorders.

Zusammenfassung

Die Homöostase des zentralen Nervensystems ist eng mit der Strömungsdynamik von Liquor (engl.: cerebrospinal fluid, CSF) und interstitieller Flüssigkeit und den damit verbundenen Transportprozessen verknüpft. Während das aktuelle Verständnis dieser Prozesse auf *in vivo* Tracer-Experimenten und Proteinanalysen des Liquors beruht, ist die Interpretation der experimentellen Daten aufgrund der vielen möglichen Transportwege und den zugrundeliegenden, teilweise noch unbekannten Transportmechanismen nicht trivial. Im Rahmen dieser Doktorarbeit haben wir rechnergestützte Methoden entwickelt, welche jene physiologischen Prozesse beschreiben, die der beobachteten Konzentrationsverteilung von gelösten Stoffen im CSF zu Grunde liegen, um dadurch schliesslich das Verständnis für die Stofftransporte im Gehirn zu verbessern. Die *in vivo* Beobachtung von schnellem Transport von Tracern innerhalb des zerebralen paravaskulären Raums (engl.: *paravascular space*, PVS) bildet die Grundlage der Hypothese, dass ein strömungsabhängiges zerebrales Reinigungssystem existiert. Wir veranschaulichen, dass dieses sogenannte glymphatische System einen beträchtlichen intrazellulären Fluss durch ein Netzwerk von Astrozyten erfordert, das von einem bis anhin unbekannten Mechanismus angetrieben wird. Wir zeigen weiter, dass die arterielle Pulsation allein nicht ausreicht, um diesen geforderten Antrieb zu erzeugen. Dennoch können das Pulsieren der Arterienwände und das dadurch induzierte periodische Strömungsfeld den Stofftransport im PVS verstärken, und zwar mittels Dispersion. Ein solcher Mechanismus wäre dazu imstande, verschiedene Tracer-Studien, die bis anhin als widersprüchlich galten, miteinander in Einklang zu bringen. Schliesslich zeigen wir, dass pathologische Veränderungen im Proteingehalt des CSFs möglicherweise auf Veränderungen der Blut-CSF-Schranke oder der CSF Dynamik zurückzuführen sind, was Implikationen auf die Behandlung neurologischer Störungen hätte.

Acknowledgements

This project would not have been possible without the support of many people. First of all, many thanks to my supervisor, Prof. Vartan Kurtcuoglu, who gave me the chance to join his group, directed this research, and has been always open for the discussions. Also thanks to my co-supervisor, Dr. Diane de Zélicourt who read my numerous papers revisions and helped me with her fruitful comments and edits. I also thank my other doctoral committee members, Dr. Aldo Ferrari and Prof. Sebastian Kozerke who offered guidance and support for the doctoral project. I appreciate very much the support I received from my PhD program, Neuroscience Center Zurich (ZNZ), which provides interesting courses, symposiums and retreats for the doctoral students.

Thanks to my officemates, colleagues and friends at The Interface Group, Mr. Mehdi Taslimifar, Mr. Willy Kuo, Ms. Lena Wiegmann, Dr. Ufuc Olgac, Dr. Anastasios Marmaras, Mr. Manuel Gehlen, Dr. Virginia Meskenaite, Ms. Helen Hammad, Mr. Norman Juchler, Dr. Andreas Spiegelberg, Dr. Claudia Danzer, Dr. Kartik Jain, Dr. Stefano Buoso, Dr. Farhad Rikhtegar, Dr. Wolfgang Wiedemair and Mr. Miles Aron for providing a nice and friendly environment to work and do research. The similar gratitude goes to the colleagues at the physiology institute with whom I shared lots of good moments and social events. I also thank Ms. Tara Gschwend of MELS, University of Zurich, for contributing Figure 3.2.

My sincerest thanks to my family who endured this long process with me. I do not know how to express my gratitude in the form of words to my parents, my heroes in life, for their generous love and support without any expectation for return. I have missed them and my two younger sisters very much in the years of being away from home, but I hope they are happy with my effort to learn, progress and explore new things. And finally, my special thanks to my girlfriend who presented me the new taste of life and accompanied me in rises, falls and adventures of the PhD years.

I gratefully acknowledge the Swiss National Science Foundation for the financial support of this project through grant 200021_147193 CINDY.

Chapter 1 Introduction

Cerebrospinal fluid is the second large liquid compartment of the brain after blood. This liquid flows in the core of the brain in the ventricular system from where it connects to cranial and spinal subarachnoid spaces (SAS) and surrounds the whole central nervous system as shown in the schematic of Figure 1.1. Investigation of cerebrospinal fluid (CSF) physiology has attracted scientists for a long time since it is thought to be very essential for the normal functioning of the central nervous system. While CSF is considered crucial for mechanical protection of the brain and spine from incidents, it is also seen very important for chemical balance of the organ.

Traditional model of the cerebrospinal fluid physiology

The classical model of the CSF physiology pictures a continuous CSF pathway originating in the ventricular system, flowing through the cisternal space into subarachnoid spaces. This classical flow pathway is demonstrated with the arrows in Figure 1.1. In this view, CSF would be produced mainly by the choroid plexus layer in the ventricles. This assumption was supported by the animal studies of Dandy [1] in which removal of the choroid plexus layer from one of the lateral ventricles in a dog brain lead to the collapse of that ventricle while the other ventricle started dilating. In the subarachnoid space, CSF would ultimately be reabsorbed into the venous system through the arachnoid granulations [2]. The anatomical structure of these granulations resemble the pressure sensitive one way valves which allow for the bulk transcellular drainage of the liquid [3].

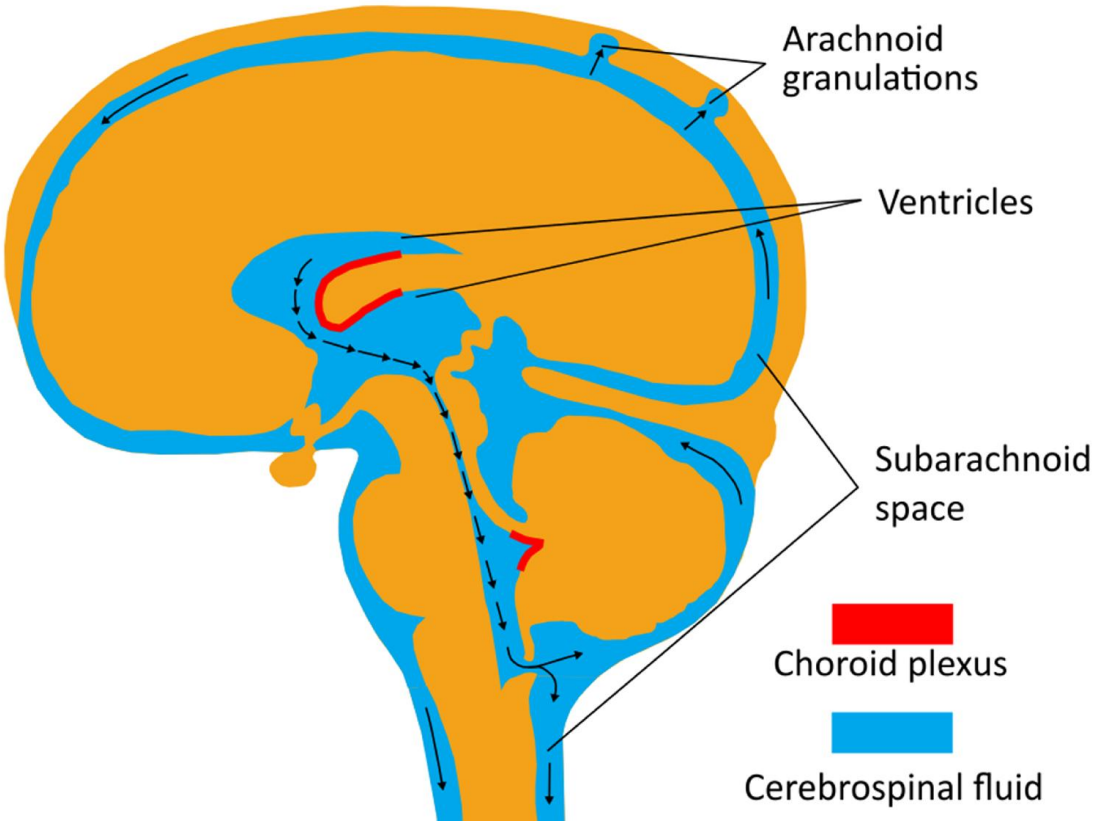

Figure 1.1: The schematic of the CSF compartments in the central nervous system and their connectivity. The classical flow pathway described for the CSF is shown with the black arrows starting from the choroid plexus layer as the major production site and ending to arachnoid granulations as the major absorption site.

New understanding of the CSF physiology

While the classical model of a directed circulation from lateral ventricles to subarachnoid space has been assumed even by some recent reviews [4], there are pool of evidences that this directed flow of CSF is only a rough simplification of a much more complicated flow system. Dandy's experiments have been also criticized because of intrinsic large possible errors in the experimental procedure since several preparations required considerable operative manipulations [5, 6]. Some experimental studies including radioactive water studies indicated that at least some of the CSF originates from another source than the choroid plexus. This secondary source of CSF could be the ependymal surface or the blood brain barrier of the capillary network within the brain tissue [7]. The interstitial liquid secreted by capillaries might drain to the pool of CSF [8] and increase the net CSF production rate. The rate of interstitial liquid clearance has been estimated by measuring the rate of the tracers removal from the tissue after tracers injection [9].

The drainage pathways for the cerebrospinal fluid are vast and do not restrict to the arachnoid granulations. It is shown that considerable amount of CSF might drain along perineural spaces to the cervical lymphatics [10]. Dural lymphatic vessels have been recently discovered adjacent to the cortical subarachnoid space [11]. The finding of these lymphatic vessels might solve the old puzzle of whether brain is an immune privilege organ or not. Antigens available in the cerebrospinal fluid could stimulate immune reactions by draining through these dural lymphatic vessels.

The circulation of the cerebrospinal fluid has been also extensively revisited. Advances in magnetic resonance flow studies made it possible to measure the CSF flow velocities in the ventricular system [12]. These measurements revealed that on top of the directed CSF flow in the ventricular system, there are relatively large amplitude flow pulsations [13]. Next to these macro-scale complexities in the CSF dynamics, high resolution imaging techniques have revealed that CSF transport might also occur in micro-circulations. Cilia beating could induce complex micro-flows in vicinity of the ventricles walls [14]. It has been shown that network of paravascular spaces surrounding the penetrating arteries provides micro-pathways connecting the interstitial liquid in the extracellular spaces to the surrounding CSF pool [15]. This complex network serves as the secondary circulation pathway for the cerebrospinal fluid in the brain. Since this circulation connects the cellular environment of the brain to the peripheral lymphatic system, it is called as glymphatic system. We will discuss this system in more details in the following section.

Cerebrospinal fluid circulation in the paravascular spaces network

Zhang et al. [16] showed that subarachnoid space extends to the cerebral cortex along the penetrating vessels branching from the larger surficial vessels in the SAS. This anatomical extension of SAS was called paravascular space (PVS) [15], also perivascular space [16] and Virchow robin space [16]. This space surrounding the arteries and arterioles was shown to be covered with a thin sheath of pia mater. Therefore, the borders of the PVS are restricted innerly by the outermost layer of the blood vessel wall (adventitia) and outerly by the thin sheath of pia layer wrapped with the glial endfeet layer. Similar paravascular spaces were also found in other human brain regions such as basal ganglia [17]. Regional differences were observed in the structure of the covering leptomeningeal layers. Two leptomeningeal layers cover the paravascular spaces in the basal ganglia while there is only one in the cerebral cortex region. Since discovery of PVS, these cerebral channels attracted lots of attention as they serve as transport pathways for CSF and its solutes content between brain interstitial space and subarachnoid space. The direction of this transport and its rate, however, has been debated among the investigators [18-20].

Recently, Iliff et al. [15] revived this long-standing discussion about transport mechanisms in the paravascular spaces with their tracer studies after cisternal solutes injection. They showed the rapid movement of the large tracers from subarachnoid space into the parenchyma along periarterial pathway and eventually drainage of these solutes along perivenous pathway. This potential circulation of the cerebrospinal fluid and its solutes content in PVS network could come along the recent discovery of the dural lymphatic drainage of the cerebrospinal fluid to build the immune reaction system of the brain. Due to this potential connection to lymphatic function of the brain, this circulation system is called “glymphatic system”. However, since the state of the art imaging techniques could not resolve the single molecules transport in the brain tissue, the real transport mechanisms functioning in this pathway are still unclear. This has even led to contradicting interpretations about the solutes transport direction in the PVS obtained by similar set of experiments. Arbel-Ornath et al. has shown that intraparenchymal injection of the tracers leads to rapid transport of these molecules along the periarterial space from parenchyma towards subarachnoid space [21] which is in the reverse direction of what Iliff et al. [15] showed. This motivates us to use our computational modeling tools developed based on the biophysical principles in order to clarify the transport mechanisms for the CSF and its solutes content in this network.

Cellular and molecular mechanisms

Aquaporins (AQP) are specific water channels expressed on the cellular membranes which facilitate water transport through the hydrophobic cell membrane [22]. In the central nervous system, AQP4 is highly expressed on the astrocytes membranes. The expression of these channels is highly localized on the endfeet processes of the astrocytes which wrap the outer surface of the PVS [23]. This localized expression of AQP4 water channels adjacent to the paravascular spaces points towards a potential important role of these channels in cerebral water transport [22]. Astrocytes are shown to be involved in several regulatory mechanisms which are essential for maintaining the central nervous system homeostasis [24]. Due to their connections including the endfeet processes covering the blood capillaries and their synaptic connections with neurons, they are nominated as a key messenger and regulator in the neurovascular unit [25].

Iliff et al. demonstrated that AQP4 knocked out animals inhibit the fast transport of the tracers through the glymphatic system of the brain [15]. However, it is not trivial to explain why aquaporin water channels removal could lead to less solute transport in the brain. These channels are directly involved in water transport, but cannot transport large molecules such as tracers. Tracers could only move along the gaps between the astrocytes endfeet processes. Therefore in chapter 2 of this thesis, we try to answer the question of how AQP4 water channels and astrocytes could contribute to solutes transport in the brain.

The possibility of CSF bulk flow in paravascular spaces and its driving force

The idea of bulk CSF flow in paravascular spaces in the brain raised from the observation of rapid transport of injected tracers along this network [9, 20]. This rapid solute transport was assumed to result from directional advective transport induced by bulk flow of CSF in that space. However, the direction of this bulk flow was not concluded due to contradictory observations from tracer studies. While injection in the subarachnoid space led to fast transport of the tracers in the paravascular spaces towards the parenchyma [20], intraparenchymal injection resulted in a reverse transport towards the subarachnoid space [21]. This confusion was reinforced since the driving force for the CSF bulk flow in both directions was introduced as the arterial blood pulsations. Ligation of the main cerebral arteries led to dampening of the arterial pulsation and consequently inhibited the rapid transport of the tracers [20]. Several experimental and theoretical studies have been conducted to justify the bidirectional bulk flow of CSF in the paravascular spaces [26-28]. In chapter 3 of this thesis, we demonstrate that, under physiological conditions, arterial pulsations are unlikely to generate substantial bulk flow and advective transport, but may still be contribute to enhanced solute

transport by dispersion. This hypothesis could explain the bidirectional rapid solute transport and therefore solve the intrinsic conflict with the CSF bulk flow assumption.

CSF dynamics role in distribution of the natural solutes such as proteins

The role of CSF dynamics in macro-scale solutes transport in the central nervous system is already shown [29, 30]. However, its influence on the CNS natural protein levels and distribution is missing. Since albumin protein is purely blood derived, its level in cerebrospinal fluid is seen as a reference value to characterize the central nervous system barriers permeability to proteins. Abnormal variation of albumin and immunoglobulin antibodies concentration in CSF is considered as hallmark of neurological diseases [31]. While the pathophysiological origins of CSF protein levels variation are still debated, both change in CSF drainage and dynamics in the cranio-spinal space [32, 33] as well as dysfunction of the blood-CNS barrier [31] have been suggested as possible causes of increased concentration of blood-derived proteins. In chapter 4, we show that both barrier dysfunction and CSF drainage change could lead to CSF protein levels variation, but this is only barrier dysfunction which could explain the characteristic behaviours observed for the protein variation in the experimentally derived CSF quotient diagrams.

Chapter 2 How astrocyte networks may contribute to cerebral metabolite clearance

This chapter has been published as:

Asgari, Mahdi, Diane de Zélicourt, and Vartan Kurtcuoglu. "How astrocyte networks may contribute to cerebral metabolite clearance." Scientific reports 5 (2015).

Abstract

The brain possesses an intricate network of interconnected fluid pathways that are vital to the maintenance of its homeostasis. With diffusion being the main mode of solute transport in cerebral tissue, it is not clear how bulk flow through these pathways is involved in the removal of metabolites. In this computational study, we show that networks of astrocytes may contribute to the passage of solutes between tissue and paravascular spaces (PVS) by serving as low resistance pathways to bulk water flow. The astrocyte networks are connected through aquaporin-4 (AQP4) water channels with a parallel, extracellular route carrying metabolites. Inhibition of the intracellular route by deletion of AQP4 causes a reduction of bulk flow between tissue and PVS, leading to reduced metabolite clearance into the venous PVS or, as observed in animal studies, a reduction of tracer influx from arterial PVS into the brain tissue.

Key words: Cerebral fluid flow, Aquaporin-4, Paravascular space, Astrocyte network, Extracellular flow, Computational model

Introduction

Homeostasis of the central nervous system is critically dependent on cerebrospinal and interstitial fluid flows and therewith associated transport processes. While it is possible to measure cerebrospinal fluid (CSF) flow in vivo at some locations [34], flow of the interstitial fluid (ISF) cannot be acquired directly, but only be inferred from the evolution of tracer distribution patterns [9, 18, 21]. However, tracers can spread in absence of flow simply driven by diffusion [35], and they can also spread in the absence of both diffusion and net flow by local advective mixing [30]. Consequently, a given tracer distribution in the brain could be the result of one of several possible flow fields. The interpretation of tracer studies with respect to the underlying flow field is thus anything but trivial.

Recent in vivo two-photon excitation microscopy studies in mice have addressed the role of aquaporin-4 (AQP4) water channels on the transport of fluorescent tracers in the brain [15]. In mice lacking AQP4, the time for tracers injected into the CSF to reach the ISF through paravascular spaces (PVS) was increased, which was interpreted as a consequence of reduced CSF influx into the PVS. While this interpretation appears intuitive at first, it becomes much less evident on second thought: Both fluid and tracers pass from the PVS to the ISF via gaps between astrocyte endfeet, but only fluid leaves the PVS additionally through AQP4. If this second pathway is removed, there should not be reduced fluid passage through the first and the time for tracers to reach the ISF should not increase.

Light may be shed onto this challenging constellation if one considers that AQP4 does not connect the PVS directly to the ISF, but rather connects it to the intracellular space of astrocytes through their endfeet first [23]. The intracellular space then communicates with the ISF via AQP4 expressed on the entire plasma membrane. Since astrocytes can exchange water both through the surrounding ISF and directly through gap junction connections with neighbouring astrocytes, fluid originating in the arterial PVS may flow through a network of astrocytes before reaching the venous PVS [24, 36]. As tracers will not pass through AQP4, and tracking of labelled water cannot be achieved in vivo with sufficiently high resolution, a computational approach to the analysis of water flow between paravascular spaces is warranted. Computational methods for the study of cerebral fluid dynamics have made great strides in recent years, and have become valuable tools that can complement experimental approaches [37-40].

Herein we aim to elucidate through numerical experiments the changes in fluid flow that lead to altered tracer distribution patterns upon AQP4 deletion observed in vivo. The underlying mathematical model considers both intra- and extracellular water pathways in a network of astrocytes between two neighbouring arterial and venous PVS. Based on the calculated fluid flow, we

further comment on the relative contributions of advection and diffusion on solute transport in the extracellular and paravascular spaces.

Methods

The model represents the space between a penetrating cortical arteriole and its venous counterpart in a mouse brain as shown in Figure 2.1. The vessels are spaced 300 μm apart [24]. In vivo, astrocytes form a structured network between adjacent larger blood vessels [25]. Each astrocyte can be thought of possessing its own domain with nominal diameter of 50 μm [24]. We refer to this domain as astrocyte unit (AU). An AU contains one astrocyte, parts of other cerebral cell types such as neurons, oligodendrocytes and microglia, as well as extracellular space at an overall ratio of 1:4 between extra- and intracellular spaces. Each AU is associated with one capillary blood vessel (see Supplementary Information S1).

There are nominally six AUs between arteriole-venule pairs, where one AU is in direct contact with the arterial and one with the venous PVS. These two units are referred to as perivascular AUs, while the remaining four constitute the central astrocyte units. All AUs are in contact with the basement membrane (BM) of their own associated capillary [41]. Capillary basement membranes of neighbouring AUs are in direct contact, representing the connectivity of the capillary bed. The capillary basement membranes of the two perivascular AUs connect additionally to their respective adjacent PVS.

Astrocyte endfeet establish the contact between AU and PVS, as well as between AU and capillary basement membrane [42], and thereby define two parallel fluid pathways: One through AQP4 expressed on the endfoot plasma membrane, and one through gaps between adjacent endfeet. Such inter-endfeet gaps (IEG) also allow the passage of solutes with hydrodynamic diameter of up to 20 nm [15, 42], whereas AQP4 only carries water. In the central part of the network, intra- and extracellular spaces and capillary basement membranes act as parallel fluid pathways that are in a constant exchange of water through AQP4 expressed on the astrocyte plasma membrane. The intracellular spaces of neighbouring astrocytes can further communicate directly through gap junction proteins, which are fairly large channels with hydrodynamic diameter of 2.5-4.5 nm [43] that allow for passage of molecules with molecular mass less than 1000 Da [24].

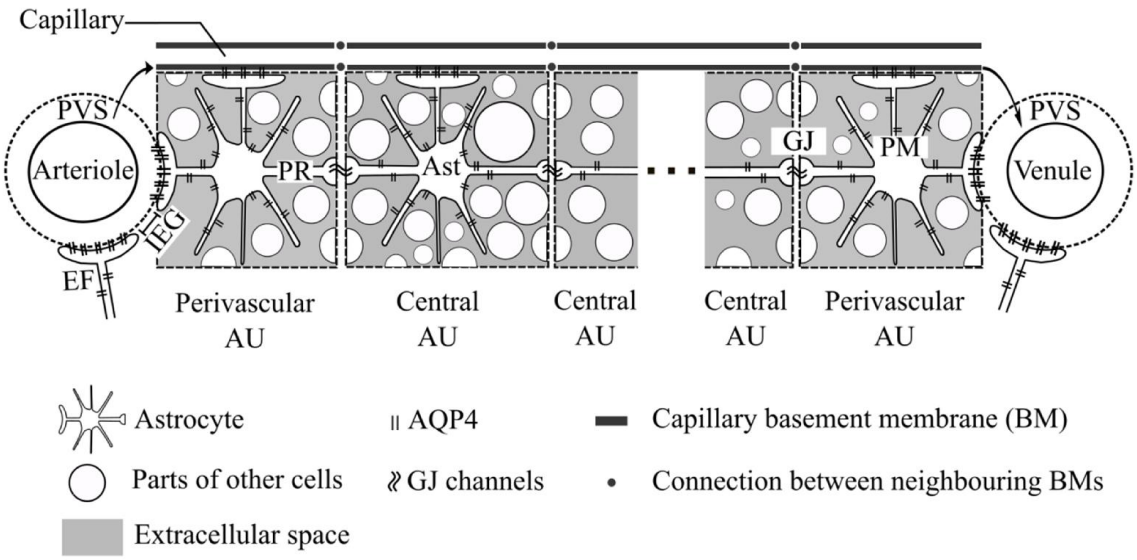

Figure 2.1: Sketch of the model domain consisting of an astrocyte network between arterial and venous paravascular spaces (PVS). The network consists of several astrocyte units (AU) that each include one astrocyte (Ast) expressing aquaporin-4 (AQP4) water channels, extracellular space (ECS) and parts of the intracellular space of other cells including neurons, oligodendrocytes and microglia. Note that the schematic is not drawn to scale and does not represent the true ratio between intra- and extracellular space. The perivascular AUs are in direct contact with their neighbouring PVS via the respective astrocyte's endfoot (EF). All astrocytes connect via endfeet to the basement membrane (BM) of the capillary associated with their AU. Neighbouring BMs connect to each other, and the perivascular BMs are additionally connected to the corresponding PVS (indicated by arrows in the figure). AQP4 covering each of these endfeet connect the capillary BMs or the PVS to the intra-astrocyte space. The intra-astrocyte and extracellular spaces within a given AU are in constant exchange of water through AQP4 water channels expressed in the astrocyte plasma membrane (PM). Gap junctions (GJ) connect the intracellular spaces of two adjacent astrocytes. PR: Astrocyte process. IEG: Inter-endfeet-gap.

In vivo tracer studies suggest the existence of net flow from the arterial to venous PVS, and therefore of a driving force gradient between the two spaces [15]. Neither origin nor magnitude of this purported gradient is known: next to arterial wall pulsations that are hypothesized to produce a driving hydrostatic pressure gradient, other driving forces are plausible as well. To reproduce the net effect of several possible forces and to employ a reasonable gradient magnitude, we set a pressure difference between arterial and venous PVS that yields a baseline extracellular fluid flow velocity in line with experimentally estimated values in grey matter [44]. As we will discuss in Supplementary Information S3, variation of the gradient magnitude within a reasonable range does not affect the conclusions of our investigation.

The computational implementation of the model is based on electrical analogy to fluid flow: pressure, resistance to flow and flow rate are represented by electric potential, resistance and current, respectively. Figure 2.2 shows the corresponding electrical network. The overall pressure drop is set to where under nominal conditions ISF flow velocity reaches $1\ \frac{\mu m}{min}$, corresponding to experimental estimates in the grey matter [44]. A sensitivity analysis reported in Supplementary Information S3 shows that changing the nominal ISF flow velocity within the range of values reported in the literature [45] does not affect the conclusions drawn in this study.

The distribution of flow between pathways depends on the resistances along those pathways. These include a) the resistances within the intra- and extracellular spaces and capillary basement membranes determined by their respective characteristic dimensions and properties; b) the interfacial resistances between astrocyte intracellular space and ECS, PVS or BM, divided between endfoot and the remainder of the plasma membrane; and c) the interfacial resistance between neighbouring astrocytes determined by the gap junction resistance to water passage. Values of the resistances and the driving pressure gradient are shown in Table 2.1 along with their derivation in concise form. Details are given in Supplementary Information S1. The underlying experimental values are listed in Table 2.2.

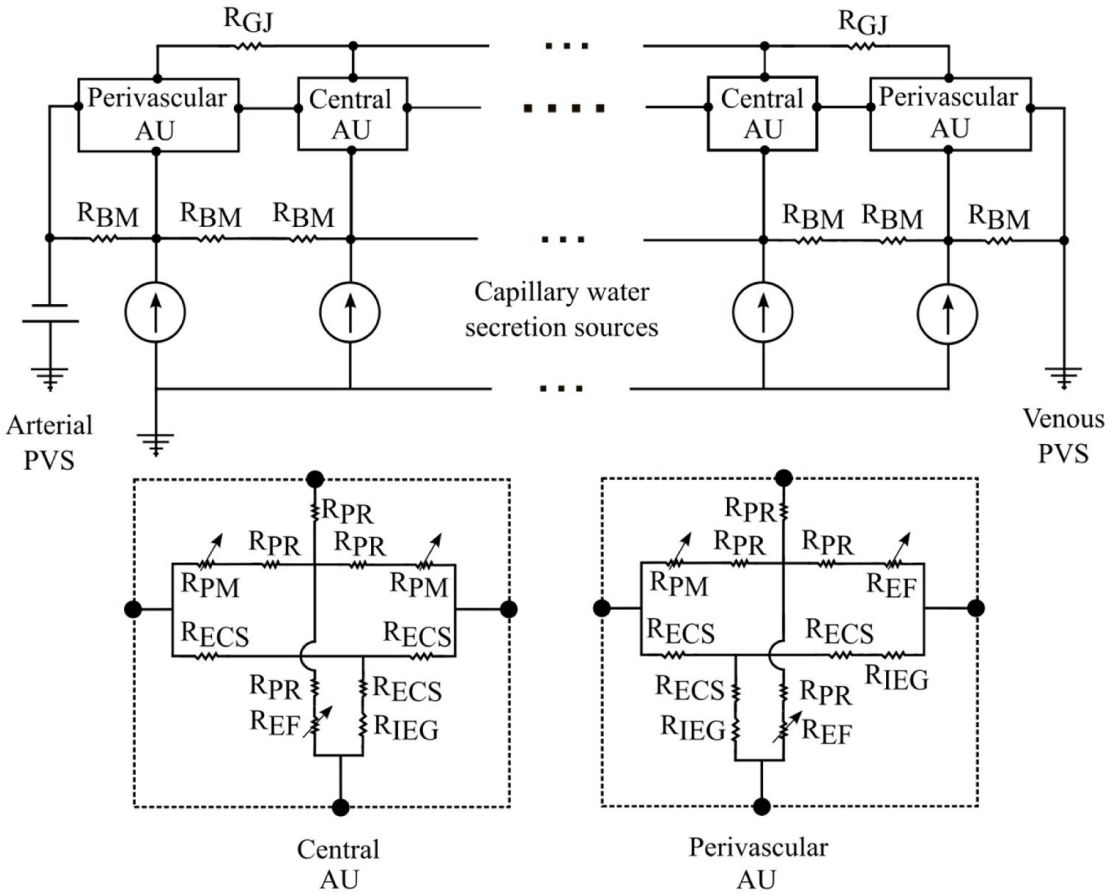

Figure 2.2: Electrical analogue model of cerebral water transport between arterial and venous paravascular spaces (PVS). Definitions of the abbreviations referring to the physical model domain are given in Figure 2.1. The voltage source represents the driving pressure difference between arterial and venous paravascular spaces that are connected by resistances (R) representing the resistance to fluid flow of capillary basement membrane (BM) segments and astrocyte units (AU). Each astrocyte unit (AU) includes resistances of both intracellular (cell processes, PR) and extracellular (ECS) pathways which are linked by membrane resistances, namely those of the astrocyte endfoot membrane (EF) and the remainder of the astrocyte plasma membrane (PM). Since these membrane resistances are dependent on the AQP4 expression level, they are indicated as variable resistances (arrows). Gap junction (GJ) resistances connect the intracellular spaces of two neighbouring astrocytes.

Next to water inflow from the arterial PVS, there is also the possibility of water secretion from capillaries into the parenchyma [9]. Since the experimental evidence for such secretion is unsatisfactory and no reliable quantitative data on the corresponding flow rate exist [46], we exclude capillary water secretion in the main calculations, but investigate its possible effects with an expanded model shown in Supplementary Fig. S2 and described in detail in Supplementary Information S1. Briefly, water secretion from the capillaries into the AUs is enforced and the pressure gradient between arterial and venous PVS is reduced so that the nominal flow rate through the tissue (combination of influx from the arterial PVS and secretion by capillaries) is maintained. As in the main model, AQP4 deletion is taken into account through a sevenfold increase in the astrocyte membrane resistances and, in addition, through a 31% reduction in capillary secretion rate as observed in glial-conditional AQP4 knockout mice after systemic hypoosmotic stress [47]. This explicit reduction is necessary because the capillary water secretion rate rather than a driving pressure gradient is prescribed. As shown in the sensitivity analysis in Supplementary Information S3, variation of the capillary secretion rate reduction within reasonable bounds does not affect the conclusions drawn in this study as long as the arterial PVS is the main source of water flux into the parenchyma.

Table 2.1: Definitions and nominal values of parameters used in the model. Derivations are documented in Supplementary Information S1.

Parameter	Equation	Nominal value
Pressure gradient between arterial and venous PVS	$\Delta P_{pvs} = R_{ISF\_total}\, Q_{ISF\_baseline}$	226 Pa
Capillary basement membrane resistance for half the length of one AU	$R_{BM} = \frac{(\frac{D_{AU}}{2})\,\mu}{K_{BM}\, A_{BM}\, n_{capillary}}$	$7.1 * 10^3 \ \frac{Pa}{\mu m^3/_s}$
ECS resistance for half the length of one AU	$R_{ECS} = \frac{R_{ECS,s}}{n_{ECS}}$	$1.12 * 10^3 \ \frac{Pa}{\mu m^3/_s}$
IEG resistance for the thickness of an endfoot	$R_{IEG} = \frac{12\ \mu\ T_{EF}}{{H_{IEG}}^3 L_{EF}}$	$9.5 * 10^1 \ \frac{Pa}{\mu m^3/_s}$
Resistance of intracellular pathway in the astrocyte processes for half the length of one AU	$R_{PR} = \frac{128\mu\tau_{PR}(\frac{D_{AU}}{2})}{\pi {D_{PR}}^4}$	$2.56 * 10^1 \ \frac{Pa}{\mu m^3/_s}$
Endfoot membrane resistance	$R_{EF} = \frac{6}{7}\frac{1}{S_{EF} * d_{AQP4\_EF} * C_{AQP4}}$	$6.43 * 10^3 \ \frac{Pa}{\mu m^3/_s}$
Resistance of the plasma membrane in half of the astrocyte unit	$R_{PM} = \frac{6}{7} \cdot \frac{2}{S_{PM} * d_{AQP4\_PM} * C_{AQP4}}$	$3.2 * 10^2 \ \frac{Pa}{\mu m^3/_s}$
Gap junction resistance	$R_{GJ} = \frac{R_{GJ,s}}{d_{GJ} * S_{GJ}}$	$1.35 * 10^4 \ \frac{Pa}{\mu m^3/_s}$

R_{ISF_total} Total flow resistance in the ISF space between arterial and venous PVS; $Q_{ISF\_baseleine}$ Nominal Interstitial fluid flow rate; $R_{ECS,s}$ Resistance of a single ECS pathway for half the length of one AU; D_{AU} Diameter of the astrocyte unit; $n_{capillary}$ Average number of capillaries in one AU; K_{BM} hydraulic permeability of the capillary basement membrane ; A_{BM} the cross section area of basement membrane; n_{ECS} Number of parallel ECS pathways in one AU; μ dynamic viscosity of ISF; T_{EF} endfoot thickness; L_{EF} endfoot length; H_{IEG} thickness of IEG; τ_{PR} Tortuosity of the astrocyte processes; D_{PR} Diameter of astrocyte process; C_{AQP4} Water conductivity of a single AQP4; S_{EF} and S_{PM} Endfoot and plasma membrane surface areas, respectively; d_{AQP4_EF} and d_{AQP4_PM} AQP4 densities over the endfoot and plasma membrane, respectively; $R_{GJ,s}$ Water resistance of single gap junction channel; d_{GJ} density of gap junction channels; S_{GJ} surface area of the contact region between neighbouring astrocytes.

Table 2.2: Parameters used for the derivation of the model parameters in Table 2.1. The most prominent spatial dimensions are illustrated in the Supplementary Figure S1. Derivations are all documented in details in Supplementary Information S1.

Parameter	Equation and nominal value	Ref
Pressures gradient		
ISF baseline velocity in the brain grey matter	$V_{ISF\_baseline} = 1\,\frac{\mu m}{min}$	[44]
Range of reported ISF velocities	$\tilde{V}_{ISF} = 0 - 14.5\,\frac{\mu m}{min}$	[44, 45]
Vascular dimensions		
Distance between arteriole-venule pair	$L_{AV} = 300$ µm	[24]
Capillary diameter	$D_{capillary} = 5$ µm	[48]
Capillary volume fraction in the brain	$\varphi_{capillary} = 1\%$	[49]
Cortical penetrating arteriole diameter	$D_{arteriole} = 25$ µm	[49]
Astrocyte dimensions		
AU diameter	$D_{AU} = 50$ µm	[24]
AU volume	$V_{AU} = \pi\frac{{D_{AU}}^3}{4} = 98125$ µm^3	
Astrocyte soma diameter	$D_{soma} = 10$ µm	[24]
Surface area of astrocyte soma	$S_{soma} = 4\pi\left(\frac{D_{soma}}{2}\right)^2 = 314\ \mu m^2$	
PM to soma surface ratio	$r_{PM/soma} = 100$	[24]
PM surface area	$S_{PM} = r_{PM/soma} * S_{soma} = 31400\ \mu m^2$	
Astrocyte process diameter	$D_{PR} = 0.5$ µm	[50]
Process intracellular space tortuosity assuming cylindrical structures	$\tau_{PR} = \frac{\pi}{2} = 1.57$	
AQP4		
Single AQP4 channel water conductivity	$C_{AQP4} = 24 * 10^{-14}\ cm^3$/s	[51]
AQP4 density on EF	$d_{AQP4\_EF} = 1000\ \mu m^{-2}$	[52]
AQP4 density on PM (except EF)	$d_{AQP4\_PM} = 100\ \mu m^{-2}$	[53]

EF length (estimated from the fact that EF fully wraps around capillaries)	$L_{EF} = \pi D_{capillary} = 15.7\ \mu m$	[42]
EF width	$W_{EF} = 5\ \mu m$	[42]
EF surface area	$S_{EF} = L_{EF} \cdot W_{EF} = 78\ \mu m^2$	
EF thickness	$T_{EF} = 1$ µm	[42]
GJ		
Hydraulic diameter of a GJ channel	$D_{GJ} = 3.5$ nm	[43]
PM thickness	$H_{membrane} = 5$ nm	[54]
Resistance of single GJ channel to water flow	$R_{GJ,s} = \frac{128\mu(2H_{membrane})}{\pi {D_{GJ}}^4} = 2.7 * 10^6\ \frac{Pa}{\mu m^3/_s}$	
GJ channel density in the contact region between neighbouring astrocytes	$d_{GJ} = 200\ \mu m^{-2}$	[55]
Surface area of the contact region between neighbouring astrocytes	$S_{GJ} = 1 \mu m^2$	[55]
ECS		
ECS thickness	$H_{ECS} = 20$ nm	[56]
Inter-endfeet gap thickness	$H_{IEG} = H_{ECS} = 20$ nm	[15, 57]
ECS volume fraction	$\varphi_{ECS} = 20\%$	[35]
Width of ECS channel surrounding typical cellular features (processes)	$W_{ECS} = \pi D_{PR} = 1.57$ µm	
ECS tortuosity assuming cylindrical structures	$\tau_{ECS} = \frac{\pi}{2} = 1.57$	
Resistance of a single ECS pathway for half the length of one AU	$R_{ECS,s} = \frac{12\mu\tau_{ECS}D_{AU}}{{H_{ECS}}^3 W_{ECS}} = 3.5 * 10^4\ \frac{Pa}{\mu m^3/_s}$	
Volume of a single ECS pathway for the length of one AU	$V_{ECS,s} = S_{PM}\ H_{ECS}$	
Total ECS volume in one AU	$V_{ECS,T} = \varphi_{ECS} * V_{AU} = 19625\ \mu m^3$	

Number of parallel ECS pathways in one AU	$n_{ECS} = \frac{V_{ECS,T}}{V_{ECS,s}} = 31.25$	
PVS		
Length of PVS segment considered for a penetrating vessel	$L_{PVS} = 500\ \mu m$	[49]
Thickness of PVS channel	$H_{PVS} = 1\ \mu m$	[19]
Hydraulic permeability of PVS	$K_{PVS} = 2 * 10^{-11}\ \frac{m^2}{Pa.s}$	[28]
Capillary BM		
BM thickness	$H_{BM} = 100\ nm$	[58]
Hydraulic permeability of BM	$K_{BM} = 2.25 * 10^{-15}\ \frac{m^2}{Pa.s}$	[59]
Volume of single capillary with the length of one AU	$V_{Capillary,s} = \pi \left(\frac{D_{capillary}}{2}\right)^2 * L_{AU} = 981.25\ \mu m^3$	
Number of capillaries in one AU	$n_{Capillary} = \frac{\varphi_{capillary} * V_{AU}}{V_{capillary,s}} = 1$	
Cross section area of BM layer	$A_{BM} = \pi\ D_{capillary}\ H_{BM} = 1.57\ \mu m^2$	
Diffusion		
Diffusion coefficient for natural solutes and tracers in the brain parenchyma	$D\ = 0.5 \text{ to } 5\ * 10^{-10}\ \frac{m^2}{s}$	[35]
Fluid properties		
Dynamic viscosity	$\mu = 1 * 10^{-3}\ {}^{kg}/_{m.s}$	
Density	$\rho = 1000\ {}^{kg}/_{m^3}$	

Results

Baseline flow rates and flow distribution between intra- and extracellular routes

To analyse the relative contributions of the intra- and extracellular fluid routes, we probed the model under baseline conditions with all pathways open and all resistances set to their nominal value as described in the Methods section. Water enters the brain tissue from the arterial PVS through gaps between astrocyte endfeet and through AQP4 expressed on astrocyte endfeet at a ratio of about 3:1. This is illustrated in Figure 2.3 astrocyte unit (AU) position 1. Once inside the tissue, there is continuous exchange of water between the intra- and extracellular spaces through AQP4 channels covering the astrocyte cell body and processes. With the ECS and capillary basement membrane having a higher resistance to fluid flow than the intracellular space, water moves preferentially through the latter at a ratio of 3:1 (see Figure 2.3, AU positions 2 to 5). Flow distribution at the exit into the venous PVS is similar to the one at entry from the arterial PVS (AU position 6). At these entry and exit positions, flow rate through the ECS is $2.94 * 10^{-2}\,\mu m^3/s$, and reduces to $1 * 10^{-2}\ \mu m^3/s$ deeper in the brain tissue, yielding a mean ECS flow rate of $1.64 * 10^{-2}\ \frac{\mu m^3}{s}$. In absence of the intracellular route, the flow rate through the ECS would reach a similar value of $1.68\ * 10^{-2}\,\mu m^3/s$ at all probed positions, but this would correspond to the overall flow rate from arterial to venous PVS (Figure 2.3, dashed horizontal line) through the parenchyma and would be less than half of the total water flow rate achieved with the astrocytes present (intra- and extracellular flows combined, $4.16 * 10^{-2}\,\mu m^3/s$).

Dependence of flow rate on number of astrocytes between arterial and venous PVS

To quantify the contribution of the central astrocytes on fluid flow, we gradually reduced the number of astrocytes between adjacent PVS from six (baseline) to two (only perivascular astrocytes). The resulting gaps were filled with generic cells that do not express AQP4. Since in the central nervous system AQP4 channels were shown to be predominantly expressed in astrocytes [60, 61], these generic cells can be neurons, oligodendrocytes, microglia or any cells of the central nervous system other than astrocytes. As illustrated in Figure 2.4, lowering the number of central astrocytes leads to reduced flow between paravascular spaces, affecting water entry from the arterial PVS through IEG more than it affects entry through endfeet.

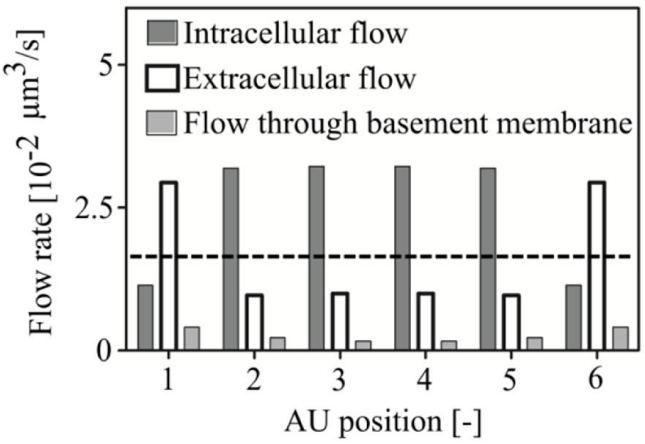

Figure 2.3: Flow rate distribution between intracellular, extracellular and capillary basement membrane pathways under normal conditions. AU Positions 1 and 6 refer the arterial and venous perivascular astrocyte units, respectively. The remaining positions refer to the central AUs. The dashed line indicates hypothetical extracellular flow rate (not including flow through basement membrane) in absence of the parallel, interconnected intracellular pathway.

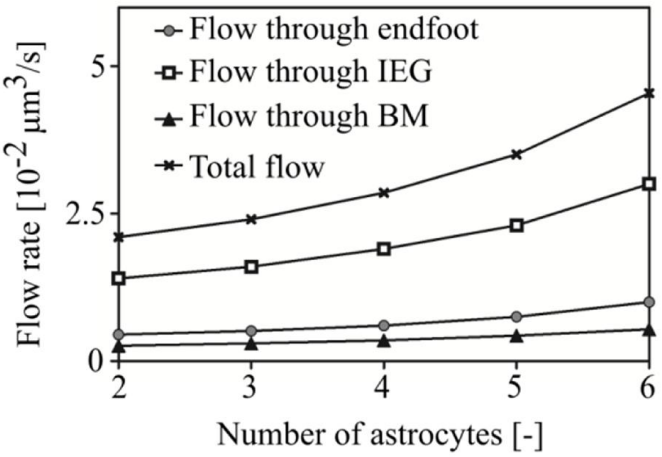

Figure 2.4: Water flow rate from arterial PVS into the parenchyma as a function of the number of astrocytes between adjacent PVS. 6 astrocytes in this space correspond to the baseline, whereas the lowest shown number of 2 only includes the perivascular astrocytes. In configurations with less than 6 astrocytes, the resulting gaps are assumed to be filled with generic cells that do not express AQP4.

Dependence of flow rate on AQP4 expression

To analyse the dependence of flow on AQP4, we disabled flow through these water channels, thereby replicating the experimental situation found in the in vivo tracer distribution study in AQP4 knock-out mice by Iliff and colleagues [15]. Deletion of AQP4 does not render the astrocyte membrane completely impermeable to water, but rather translates into a sevenfold reduction in overall water conduction of the astrocyte membrane [62]. We modelled this as a sevenfold increase in overall plasma and endfoot membrane resistances (see Supplementary Information S1). As one would expect, deletion of AQP4, which are polarized on the astrocyte endfeet, reduces water entry into the brain tissue through the endfeet substantially (Figure 2.5a, 90% reduction). Far less intuitive, but in agreement with the mentioned experimental study [15], AQP4 deletion also reduces flow through IEG markedly (Figure 2.5a, 30% reduction) and flow through the capillary basement membrane by 33%. The combined effect is a 43.4% reduction in the total flow rate. When the number of astrocytes between arterial and venous PVS is reduced from the baseline number of six to two, AQP4 deletion leads to a 14% increase (rather than decrease) in flow through IEG (Figure 2.5b) and a reduction of total flow rate by only 7%. The flow rate changes in response to AQP4 knock-out as a function of the astrocyte coverage is shown in Figure 2.5c.

Deletion of AQP4 also affects flow through gap junctions, as shown in Figure 2.6. Consistent with experimental observations of increased inter-cellular tracer spread in AQP4 knock-out [63], flow through GJ is increased when AQP4 is deleted.

Dependence of flow rate on AQP4 polarization

To assess the influence of AQP4 polarization on flow rate and flow distribution, we distributed AQP4 uniformly over the entire astrocyte plasma membrane. This is in contrast to the baseline situation in which AQP4 populates the endfoot with ten times higher density than it does the remainder of the plasma membrane [52]. AQP4 depolarization thus leads to a tenfold increase in resistance to water flow through the endfoot compared to baseline (from $6.43 * 10^3 \ \frac{Pa}{\mu m^3/_s}$ to $6.43 * 10^4 \ \frac{Pa}{\mu m^3/_s}$), while the resistance of the remaining membrane is only marginally reduced (from $3.2 * 10^2 \ \frac{Pa}{\mu m^3/_s}$ to $3.13 * 10^2 \ \frac{Pa}{\mu m^3/_s}$), owing to its large surface area compared to that of the endfoot.

Depolarization of AQP4 causes an 89% reduction in water entry from the PVS through the endfoot (Figure 2.7). This is accompanied by a 6% increase in inflow through IEG and a 3.7% reduction in flow through the capillary basement membrane. The total flow rate is reduced by 15.9%.

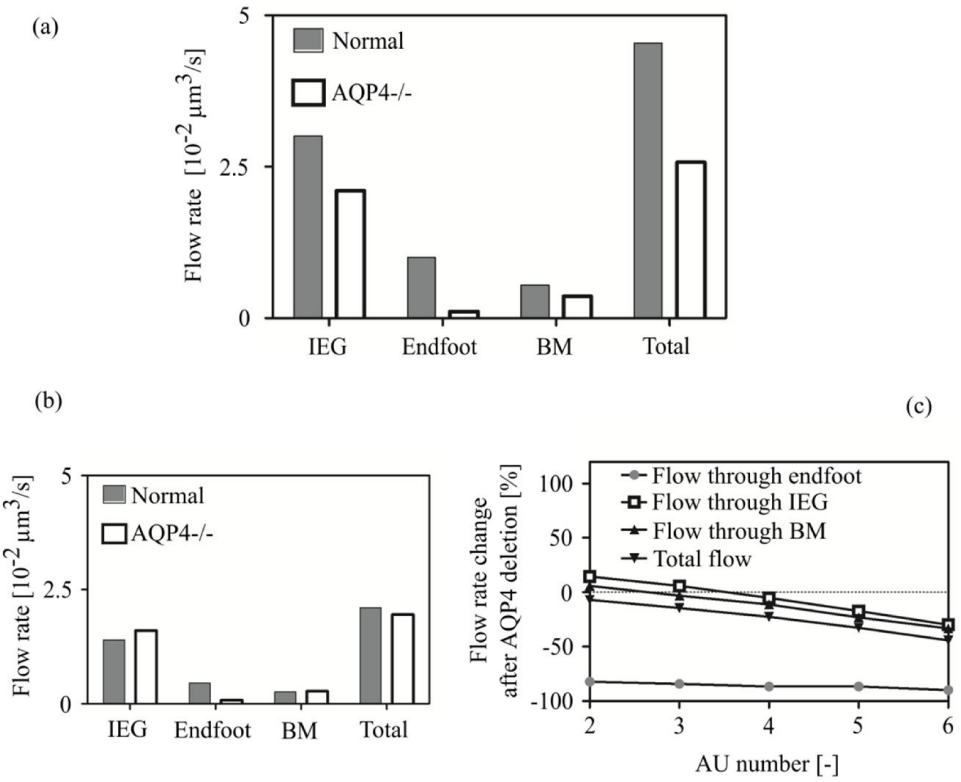

Figure 2.5: Effect of AQP4 deletion on water flow rate from PVS to the parenchyma through endfoot AQP4 channels, inter-endfeet-gaps (IEG), capillary basement membrane (BM) and in total. (A) Baseline configuration with 6 astrocytes. (B) Configuration with only the two perivascular astrocytes with the remaining space filled with other cells not expressing AQP4. (C) Percentage change in flow rates from PVS to tissue after AQP4 deletion as a function of the number of AUs included in the network.

Influence of capillary water secretion on flow rate

To test the influence of water secretion from capillaries on changes in flow rate through inter-endfeet gaps upon AQP4 deletion, we employed the expanded model shown in Supplementary Fig. S2. Having now two sources of inflow into the modelled space between arterial and venous PVS, we varied the contribution of capillary secretion to total inflow from 0 to 100% in six steps, recording the flow rate through perivascular inter-endfeet gaps (Figure 2.8). Increasing the contribution of capillary secretion reduces inflow through IEG on the arterial side (Figure 2.8a), but does not change outflow through perivenous IEG noticeably (Figure 2.8b).

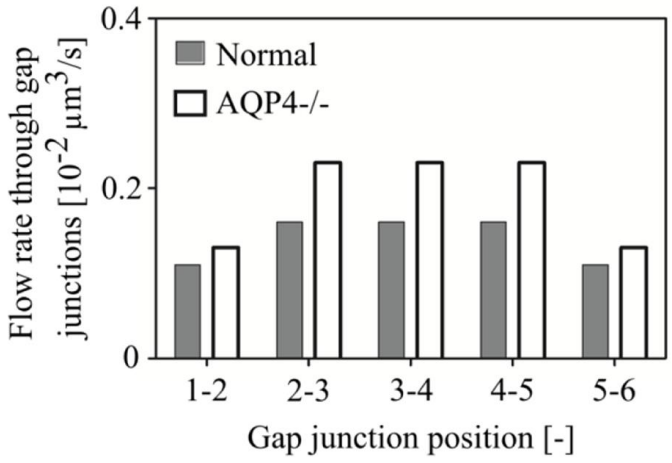

Figure 2.6: The effect of AQP4 deletion on water flow rate through the direct GJ connections between neighbouring astrocytes in the network. Gap junction positions 1-2 and 5-6 refer to the connection between the arterial perivascular astrocyte and the first central astrocyte, and between the last central astrocyte and venous perivascular astrocyte, respectively.

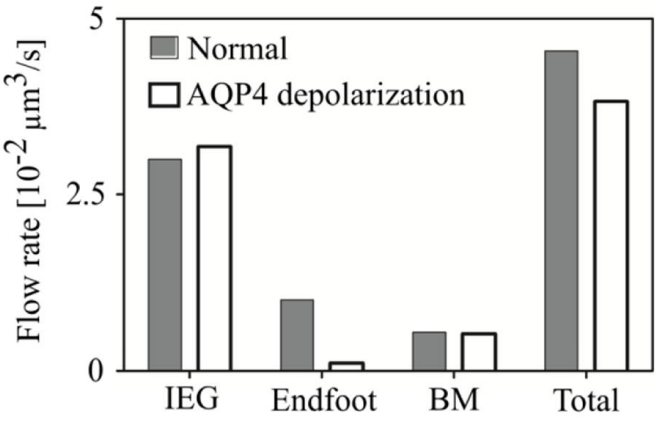

Figure 2.7: Effect of AQP4 depolarization on water flow rate from PVS to the parenchyma through endfoot AQP4 channels, inter-endfeet-gaps (IEG), capillary basement membrane (BM) and in total. Dark bars refer to the baseline state with AQP4 water channels polarized on the endfoot, whereas light bars refer to the depolarized state.

Just as in the model without water secretion by capillaries, AQP4 deletion leads to a reduction in flow rate through periarterial IEG, as long as the capillaries' contribution does not exceed 80% of the overall inflow into the parenchyma. On the venous side, the capillary secretion rate influences the change in flow rate through IEG from baseline to AQP4 knock-out only slightly. It should be noted that the behavior of an incomplete astrocyte network as described in Section 3.2 is more sensitive to variations in capillary water secretion. This is discussed in Supplementary Information S3.

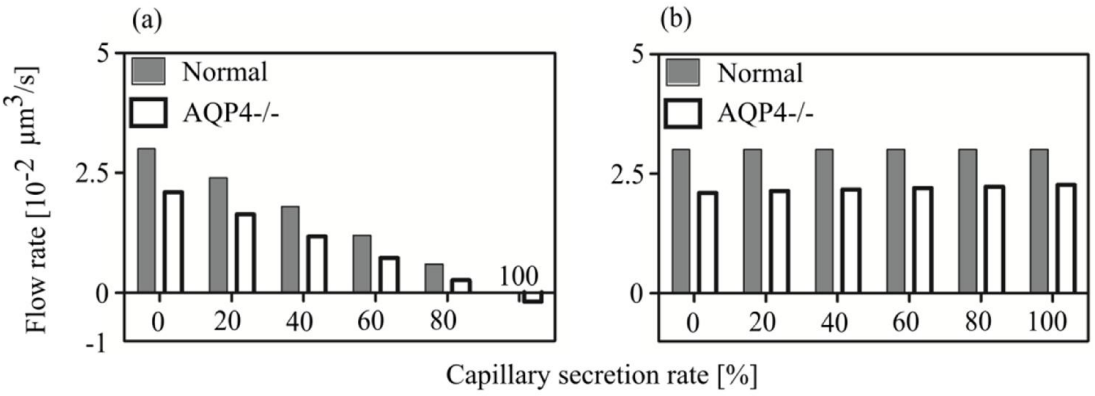

Figure 2.8: Effect of capillary water secretion rate on the water flow rate through inter-endfeet gaps connecting the perivascular AUs to the (a) arterial and (b) venous PVS, respectively. The left most pair of bars in both panels show values for zero water secretion, whereas the right most pairs bars give the values for the case where all of the water inflow into the domain stems from capillary secretion. The white bars represent the AQP4 deletion state, in which next to the removal of the corresponding pathway in the AUs, a reduction of the capillary water secretion by 31% is imposed [47].

Sensitivity analysis

To evaluate the sensitivity of the reported results on the choice of parameter values, we assessed the model output for parameter variations within realistic bounds. Results of the sensitivity analysis are reported in Supplementary Information S3. Consistent behaviours were noted in all cases, namely a significant contribution of the intracellular pathway to total water transport and a reduction in both endfoot and IEG flow rates after AQP4 deletion.

Discussion

We have shown how parallel extracellular and intracellular pathways established by astrocyte networks may facilitate bulk fluid flow between adjacent arterial and venous paravascular spaces. The unintuitive changes in tracer distribution upon AQP4 deletion observed in vivo can be explained by the inhibition of the connection between these parallel pathways.

The high polarization of AQP4 on astrocyte endfeet may distract from the presence of these water channels on the remainder of the cell. The entire astrocyte plasma membrane including all processes constitutes an exchange surface that is approximately 400 times larger than the endfoot membrane, allowing for substantial water exchange between intra- and extracellular spaces even though the AQP4 density is ten times lower there than on the endfoot [52]. The importance of such water exchange derives from the fact that a) the resistance of the ECS to water flow is higher than that of the intracellular space (Table 2.1), and that b) two thirds of the fluid exiting the arterial PVS enter the extracellular space (Figure 2.3). To follow the lower resistance intracellular route, water has to first pass from the ECS into the cells, which is facilitated by AQP4 expressed on the entire astrocyte plasma membrane.

The significance of this continuous water exchange within the tissue is evidenced when astrocytes in the central AUs are progressively replaced by generic cells that do not express AQP4 (Figure 2.4). In the situation with only two perivascular AUs (i.e. omitting the contribution of the central astrocytes), the total flow rate is cut to 46%, clearly demonstrating the function of the astrocytes in reducing the effective resistance of brain tissue to water flow and facilitating fluid transit between adjacent PVS.

The water exchange between the parallel intra- and extracellular routes explains observations by Iliff et al. who report that AQP4 knock-out mice had a lower rate of tracer penetration from the PVS into the brain tissue than their wild type counterparts [15]. This implies reduced flow rate through IEG upon AQP4 deletion, since tracers cannot pass through AQP4. If intra- and extracellular routes served as disconnected parallel fluid pathways, deletion of AQP4 would not reduce tracer influx from the PVS through the IEG, and the flow rate through IEG would be $1.68 * 10^{-2}\,\mu m^3/s$ (dashed line in Figure 2.3) irrespective of the presence or absence of AQP4. In contrast, deletion of AQP4 in the complete network of astrocytes reduces the flow rate through IEG (Figure 2.5a). This is in line with the experimental observations.

The tracer distribution observed in vivo does not only depend on fluid flow through PVS and brain tissue, but also on diffusion. To assess the relative contributions of diffusion and advection to tracer movement, we consider the Péclet number [64],

$$Pe = \frac{Lu}{D}, \qquad (2.1)$$

where L and u are characteristic length and velocity, respectively, and D is the diffusion coefficient of the tracer. When this dimensionless number is larger than one, advection (i.e. transport of the tracer with the flow) is more important than diffusion.

Indirect measurements of ISF velocity via tracers have yielded a range of values from 0 to $14.5\ \frac{\mu m}{min}$ [44, 45]. For the calculation of Pe we consider a range of $1 - 5.5\frac{\mu m}{min}$, where the lower limit is the maximum for grey matter given by Rosenberg et al (Fig. 4 in [44]), and the upper limit the minimum given by [45, 65, 66] for the entire brain. With this, Pe in the parenchymal ECS is in the range of 0.005 to 0.275, while in the PVS it is 0.45 to 25 (see Supplementary Information S2). This means that while diffusion dominates tracer distribution in the parenchyma, supply of the tracer through the arterial and removal through the venous PVS depend on both advection and diffusion.

More relevant than the influx of artificial tracers is the fate of natural metabolites in the ISF. These are hypothesized to be cleared through the venous PVS [15]. For the baseline astrocyte network with functioning AQP4, the ratio of solute transport capacities between PVS and tissue is in the range of 0.045 to 0.61 for naturally occurring solutes (see Supplementary Information S2). This means that, under normal conditions, the solute transport capacity of the tissue (dominated by diffusion) is higher than that of the paravascular space (dependent on both advection and diffusion). Thus, the PVS appears to be the limiting segment in the solute transport pathway. In absence of AQP4, the solute transport capacity of the PVS is further diminished because the fluid flow rate through it is reduced (Figure 2.5a). Consequently, even though metabolites are transported largely by diffusion in the brain tissue, their removal is nevertheless dependent on bulk flow through the PVS, and in turn on the net flow of water through both intra- and extracellular routes in the tissue. This also explains in vivo experimental observations of reduced solute clearance from the tissue in AQP4 knock-out mice [15].

There are indications that the fluid flow rate through the PVS is increased during sleep [67], presumably due to reduced resistance in the ECS as a consequence of an increase in volume of this space [67]. In our model, the reported 60% increase in ECS volume [67] translates to a 46% reduction of ECS resistance. Even though increased ECS volume necessitates a decrease in intracellular volume and thus an increase in the corresponding water pathway's resistance (by 25%), the overall resistance between arterial and venous PVS drops, leading to a 36% increase in total flow rate. This in turn raises the ratio of solute transport capacity in the PVS to that in the tissue to a range of 0.048 to 0.77 for naturally occurring solutes (see Supplementary Information S2). This means that during

sleep, the clearance rates of larger metabolites such as amyloid beta are closer to their limit set by diffusion in the brain tissue.

Para-arterial water inflow and water secretion from capillaries into the parenchyma may coexist. Under the here investigated conditions, the observations of reduced tracer influx into the ISF in animals lacking AQP4 are reproduced as long as the arterial PVS is the main source of water influx into the parenchyma. Under nominal conditions (Figure 2.8), this is even the case for ratios of capillary secretion to inflow from PVS of up to 4:1. At higher ratios, water is drained through the arterial PVS rather than supplied, and AQP4 deletion increases drainage.

The relevance of this work derives from the fact that it is currently not possible to measure interstitial fluid flow directly in vivo, but that flow rates have to be inferred from the evolution of tracer distribution patterns. This also implies that direct quantitative experimental validation of our model will be extremely challenging. However, our results are in agreement with qualitative experimental observations:

We show that deletion of AQP4 channels results in a reduction of IEG flow rate and increase in the flow rate through GJs, both of which have also been observed in vivo in AQP4 knock-out rodents [15, 63]. Our parametric variations of the number of astrocytes and AQP4 distribution provide a rationale for the makeup of the fluid pathway structures, demonstrating that both AQP4 polarization on the astrocyte endfeet and a dense astrocyte network are required for optimal water transport between paravascular spaces.

The flow distribution between intra- and extracellular pathways is determined by the resistances of the individual routes. Inadequate choices of resistance values could yield incorrect results. To reduce this possibility, we performed a sensitivity analysis as documented in Supplementary Information S3. This analysis shows that our model is robust with respect to variation of parameters within realistic bounds.

Our model considers a pressure gradient between the arterial and venous PVS as the driving force behind the observed fluid flow. This gradient can be viewed as the result of the superposition of all driving forces acting on water on its way from arterial to venous PVS, including possible hydrostatic pressure caused by arterial wall pulsation [20, 68]. Since the magnitude of the gradient is unknown, we prescribe a value that yields a baseline extracellular fluid flow velocity in line with experimental estimates in grey matter [44]. As a consequence, the absolute values of the here reported flow rates should also be seen as estimates. However, as discussed in Supplementary Information S3, the conclusions of the investigations are not affected by reasonable changes of the gradient magnitude.

More important than its value is the question whether such a gradient exists in the first place. The reduction of the rate of tracer distribution and metabolite clearance in mice lacking AQP4 appears to necessitate bulk flow from arterial to venous PVS, and with it a corresponding driving force gradient. Should it be the case that AQP4 deletion has secondary effects that influence fluid flow, other explanations for the observed tracer spread would have to be considered. These include flow-induced mixing and dispersion in the PVS, as well as increased effective tracer and metabolite diffusivity in the parenchyma due to Taylor dispersion [69]. Both effects could be caused by arterial pulsation and do not necessitate bulk flow.

In summary, while diffusion is the main mode of solute transport in brain tissue, it does not suffice to explain effective metabolite clearance into the venous paravascular space observed in tracer studies in vivo. Other modes of transport need to be taken into account as well. We have shown with this computational study that if there is bulk flow between arterial and venous paravascular spaces, astrocyte networks may serve as low resistance pathways to water flow that enhance metabolite clearance through a parallel, extracellular route. Observations of reduced metabolite clearance in animals lacking AQP4 may be explained by diminished bulk flow caused by inhibition of the interconnection between the astrocyte networks and the extracellular route.

Supplementary Information – Estimation of flow resistances

Parameters

Table 2.2 in the main text lists all parameters used, accompanied by the corresponding reference or associated equation for derived quantities. For ease of understanding, the most prominent spatial dimensions used to obtain the model parameters are illustrated in the Supplementary Fig. S1.

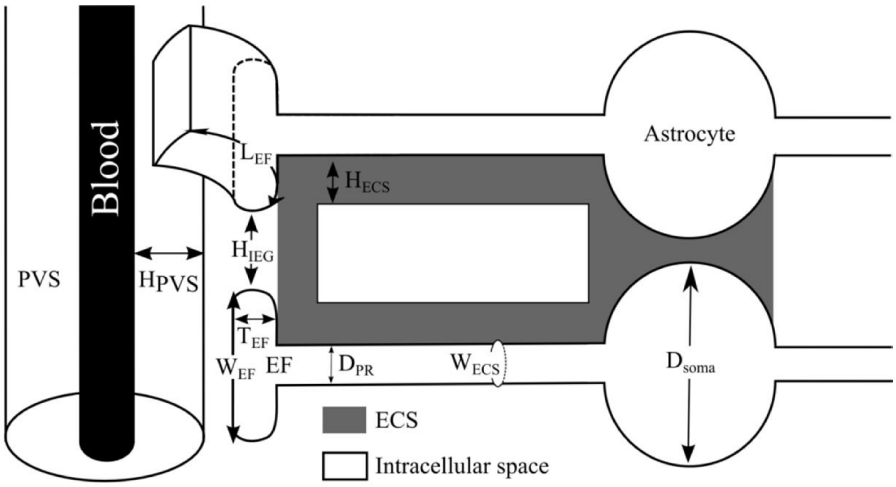

Supplementary Figure S1: Dimensions used to obtain the model parameters. Nomenclature and values of these dimensions are given in Table 2.2.

Pressure gradient between arterial and venous paravascular spaces

A pressure difference of 226 Pa (1.7 mmHg) between arterial and venous PVS is required to yield the baseline interstitial fluid flow velocity of $V_{ISF\_baseline} = 1\,\frac{\mu m}{min}$ (see Table 2.2). This pressure difference should be seen as the net value produced by the superposition of all relevant hydrostatic and osmotic pressure sources, including arterial wall pulsations[20, 68]. The stated 1.7 mmHg appear reasonable compared to the 17 mmHg blood pressure drop from arteriole to venule [70].

Estimation of the bulk flow resistance in channel structures of the brain micro-environment including extracellular and intra-cellular pathways.

Simplifications

Laminar flow is assumed in the ECS, which is supported by the low Reynolds number in that space,

$$Re = \frac{\rho u D_h}{\mu} < 5 * 10^{-8}, \qquad \text{(S1.1)}$$

where u is the expected flow velocity in the range of $5.5 - 14.5\ \frac{\mu m}{min}$ [45], D_h is the hydraulic diameter of the fluid path (taken to be equal to H_{ECS}), ρ and μ are, respectively, density and dynamic viscosity of the interstitial fluid.

The ECS can be viewed as a tortuous pathway that winds around cellular elements in the tissue. This may have two effects: first, tortuosity increases the effective length of a channel compared to a straight one, which is typically accounted for by correcting the straight length by a tortuosity coefficient; second, local curvatures may induce secondary flow structures that would dissipate energy and increase the effective resistance of the path. However, this second effect can be neglected herein, as demonstrated by the very low Dean number (Dn),

$$Dn = \frac{\rho u H_{ECS}}{\mu}\left(\frac{H_{ECS}}{R}\right)^{1/2} < 10^{-2}, \tag{S1.2}$$

where R is the characteristic radius of curvature of the pathway, which we considered to be equal to half of the cell process diameter (D_{PR}). Hence, we may retain the channel flow equations to derive the resistances of the different flow pathways, solely correcting them for the increase in effective path length.

Derivation of R_{ECS}

With the above simplifications, the resistance of one ECS pathway, $R_{ECS,s}$, can be obtained from the analytical expression for a straight channel [71],

$$R_{ECS,s} = \frac{12\mu\tau_{ECS}(\frac{D_{AU}}{2})}{H_{ECS}{}^{3}W_{ECS}} \tag{S1.3}$$

where τ_{ECS} is the ECS channel tortuosity, with the product $\tau_{ECS}(\frac{D_{AU}}{2})$ representing the effective length of an ECS channel spanning half of one AU. The resistance value for one ECS pathway obtained using Equation (S1.3) corresponds to a single route through the ECS. In practice, there are multiple ECS routes within a single astrocyte unit (AU). Using the ECS volume fraction φ_{ECS} and characteristic dimensions reported in Table 2.2, we can determine the volume of characteristic single ECS route, $V_{ECS,s}$, and deduce the total number of routes, n_{ECS}, required to match the total ECS volume, $V_{ECS,T}$, from the ratio of the two volumes

$$n_{ECS} = \frac{V_{ECS,T}}{V_{ECS,s}}. \tag{S1.4}$$

Assuming that these individual ECS routes carry water in parallel, the overall ECS resistance of half the length of one AU can be approximated as:

$$R_{ECS} = \frac{R_{ECS,s}}{n_{ECS}}. \quad \text{(S1.5)}$$

Estimation of the inter-endfeet gap resistance, R_{IEG}

Applying the analytical expression for the resistance of a straight channel (Equation (S1.3)), and assuming the length, height and width of the IEG to be given by the endfoot thickness, T_{EF}, ECS channel thickness, H_{ECS}, and characteristic length of the endfoot contact area, L_{EF}, we obtain:

$$R_{IEG} = \frac{12\mu T_{EF}}{{H_{ECS}}^3 L_{EF}}. \quad \text{(S1.6)}$$

Tortuosity is assumed to be 1, since the IEG is very short. Based on the observation that astrocyte endfeet can completely enwrap individual capillaries [42], the characteristic endfoot length is given the same value as the circumference of a capillary,

$$L_{EF} = \pi\, D_{capillary}. \quad \text{(S1.7)}$$

Estimation of the capillary basement membrane resistance, R_{BM}

To calculate the overall resistance of the capillary basement membrane layers in one AU, we need an approximation of the number of capillaries available in the astrocyte domain volume, $n_{capillary}$. To this end, we consider the capillary volume fraction $\varphi_{capillary}$ in brain tissue:

$$n_{capillary} = \frac{\varphi_{capillary} * V_{AU}}{V_{capillary,s}}, \quad \text{(S1.8)}$$

where V_{AU} is the astrocyte domain volume and $V_{capillary,s}$ the characteristic volume of a single capillary segment of the length of one AU. $n_{capillary}$ evaluates to approximately 1, which means that the overall capillary segment length in an AU sized volume of brain tissue has the length of one AU. When we state in the description of our model that each AU is associated with one capillary, we refer to this situation.

The capillary basement membrane is rather dense. For half the length of one AU, its resistance can be calculated as

$$R_{BM} = \frac{\frac{D_{AU}}{2}\,\mu}{K_{BM}\, A_{BM}\, n_{capillary}}, \quad \text{(S1.9)}$$

where K_{BM} is the permeability of the capillary basement membrane and A_{BM} is its cross-sectional area of this membrane calculated based on the characteristic dimensions reported in Table 2.2.

Estimation of intra-cellular resistances, R_{PR}

Following a similar approach, the intracellular resistance of an astrocyte process spanning half the length of one AU is obtained from resistance of cylindrical pipe of diameter, D_{PR}, and effective length $\tau_{PR}(\frac{D_{AU}}{2})$:

$$R_{PR} = \frac{128\mu\tau_{PR}(\frac{D_{AU}}{2})}{\pi {D_{PR}}^4} = 2.56 * 10^1 \ \frac{Pa}{\mu m^3/_s}. \quad \text{(S1.10)}$$

The above equation assumes free fluid flow through the entire intra-cellular space. In practice, the volume fraction of the cytosol of retinal glial cells is > 50% [72]. Inferring a similar distribution for astrocytes would bring the intracellular pathway resistance up to $6.45 * 10^1 \ \frac{Pa}{\mu m^3/_s}$. However, as demonstrated in our sensitivity analysis (Supplementary Information S3), this has hardly any impact on the reported results due to the dominant effect of the plasma and endfoot membrane resistances.

Estimations of the cell membrane resistances

Contribution of AQP4 channels to the membrane resistance

In our model, we divide the plasma membrane resistance into two components, each representing the plasma membrane in half of the astrocyte unit. Knowing the conductivity of a single AQP4 channel, C_{AQP4}, to be $24*10^{-14}$ cm^3/s [51], the contribution of AQP4 to the plasma membrane resistance is given by

$$R_{PM\_AQ} = \frac{1}{d_{AQP4\_PM}\left(\frac{S_{PM}}{2}\right) C_{AQP4}}, \quad \text{(S1.11)}$$

where d_{AQP4_PM} is the density of AQP4 over the plasma membrane (not including the endfoot) and $S_{PM}/2$ is the surface area of the plasma membrane in half of an AU. The AQP4 contribution to the resistance of the endfoot plasma membrane, R_{EF_AQ}, is obtained according to equation (S1.11) as well, using the density of AQP4 on the endfoot, d_{AQP4_PM}, and estimating the endfoot surface area as

$$S_{EF} = L_{EF}\, W_{EF} = \left(\pi D_{capillary}\right) D_{capillary}. \quad \text{(S1.12)}$$

This estimation makes use of the observation that astrocyte endfeet can completely enwrap individual capillaries with approximately the same width as the capillary diameter [42].

Overall membrane resistance and its change after AQP4 deletion

The overall resistance of the astrocyte plasma membrane in one astrocyte unit is given by

$$R_{PM} = \frac{R_{PM\_AQ} R_{PM\_mb}}{R_{PM\_AQ} + R_{PM\_mb}}, \quad \text{(S1.13)}$$

where R_{PM_AQ} is the resistance of AQP4 channels on the plasma membrane obtained from equation (S1.11) and R_{PM_mb} is the resistance of the membrane itself. While the contribution of the AQP4 channels was estimated above, that of the membrane still needs to be determined. We make use of the fact that after AQP4 deletion, the overall resistance $R_{PM_{AQ-/-}}$ is seven times higher than the resistance in the presence of AQP4 channels [62], R_{PM}. Together with equation (S1.13), this yields the following relationships:

$$R_{PM_{AQ-/-}} = R_{PM\_mb}, \quad \text{(S1.14)}$$

$$R_{PM_{AQ-/-}} = 7R_{PM}, \quad \text{(S1.15)}$$

from which we can deduce

$$R_{PM} = \frac{6}{7} R_{PM\_AQ}. \quad \text{(S1.16)}$$

The overall resistance of the endfoot membrane, R_{EF}, can be derived similarly.

Gap junction resistance

The typical hydraulic diameter of a gap junction channel, D_{GJ}, is 2.5-4.5 nm [43]. As GJ channels connect two plasma membranes of 4-6 nm thickness, $H_{membrane}$ [54], their length is approximately in the range of 8-12 nm. Navier-Stokes equations are principally only valid for continuum fluids. Nevertheless, they have been shown to provide good estimates for water dynamics in nanochannels [73], with diameters as small as 5-10 times the width of an individual fluid molecule's diameter [74]. Accordingly, we estimate the resistance of single GJ channel based on the assumption of Hagen-Poiseuille flow through a circular cylindrical channel with diameter D_{GJ} and length $2H_{membrane}$:

$$R_{GJ,s} = \frac{128\mu(2H_{membrane})}{\pi {D_{GJ}}^4}. \quad \text{(S1.17)}$$

The total resistance of a gap junction is obtained by considering the density of GJ channels d_{GJ} of $200\ \mu m^{-2}$ over a contact area S_{GJ} of $1\ \mu m^2$ estimated from the figures in the reference [55]:

$$R_{GJ} = \frac{R_{GJ,s}}{d_{GJ} * S_{GJ}}. \quad \text{(S1.18)}$$

Water secretion by capillaries

To assess the effect of possible water secretion by capillaries[5], we introduce an expanded version of the model described in the manuscript. This is shown below in Supplementary Fig. S2. Water secretion by capillaries is enforced by flow sources (or current sources in the electric analogue). There is one source per AU length of capillary, thus 6 sources with the same secretion rate in total. The secretion rate and the pressure drop from arterial to venous PVS are set such that the baseline parenchyma flow rate (combination of the total influx through arterial PVS, including IEG, EF and BM, and secretion by capillaries) is always maintained. Thus when the secretion rate is step-wise increased from its nominal value of zero, the pressure drop from arterial to venous PVS is decreased to keep the baseline parenchyma flow rate (Supplementary Table S1). Even when capillary secretion accounts for the entire parenchymal water influx, a pressure gradient from arterial and venous PVS is still necessary to ensure the prescribed ISF flow velocity. In absence of this gradient, there would be outflow through both arterial and venous PVS, yielding zero net ISF velocity.

When the effect of AQP4 deletion is studied, the secretion rate is reduced by 31%[47] without further adjustment of the above-determined inter-PVS pressure drop (Supplementary Table S1). This 31% reduction is based on observations in glial-conditional AQP4 knockout mice after systemic hypoosmotic stress[47]. Under normal osmotic conditions, one can expect less reduction in the secretion rate upon AQP4 deletion, since water secretion is an active process that can be upregulated. We investigate the effects of both higher and lower rates of secretion reduction in the sensitivity analysis in Supplementary Information S3.

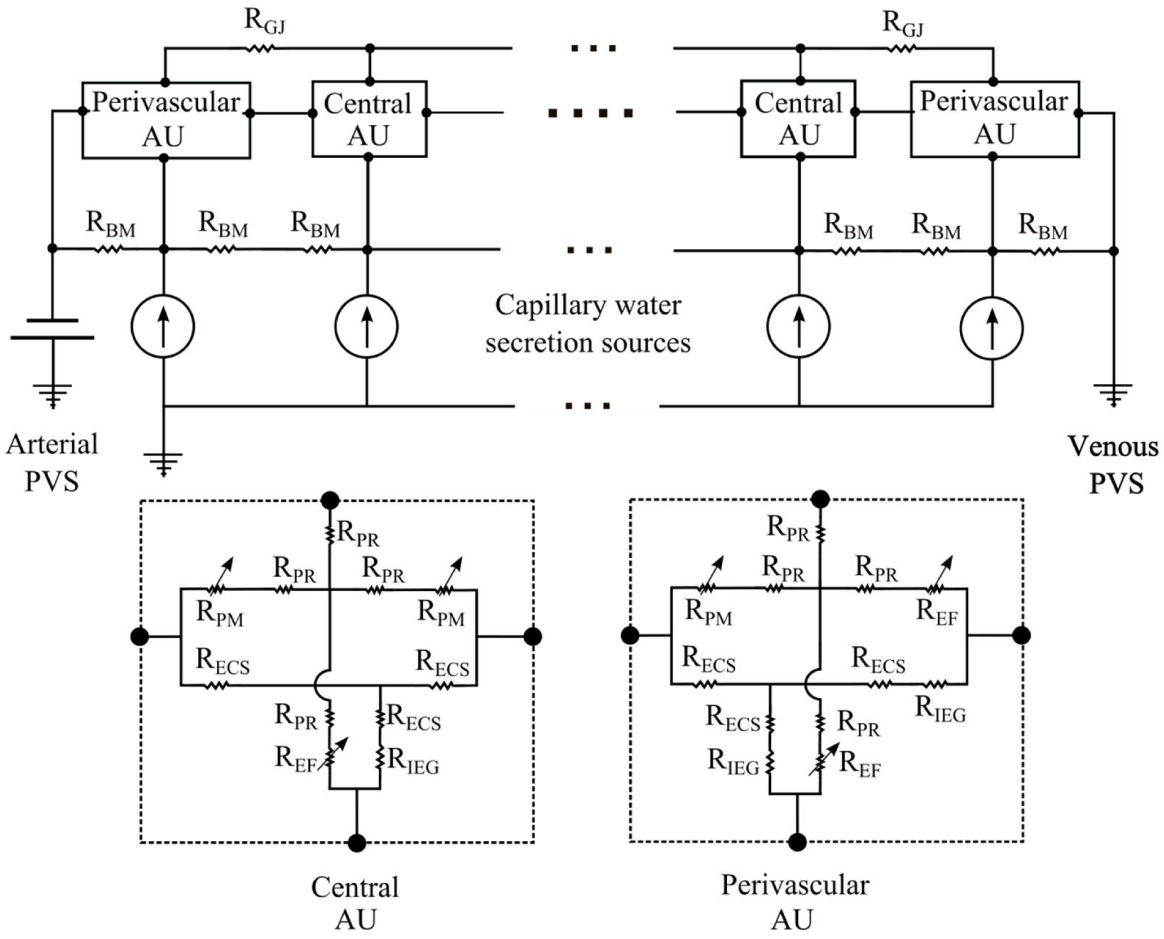

Supplementary Figure S2: Electrical analogue model of cerebral water transport between arterial and venous paravascular spaces (PVS) including water secretion sources at the capillary level in addition to the elements described in Figure 2.2 (main text). Definitions of the abbreviations referring to the physical model domain are given in Figure 2.1 (main text). Arterial and venous paravascular spaces are connected by resistances (R) representing the resistance to fluid flow of capillary basement membrane (BM) segments and astrocyte units (AU). Each astrocyte unit (AU) includes resistances of both intracellular (cell processes, PR) and extracellular (ECS) pathways which are linked by membrane resistances, namely those of the astrocyte endfoot membrane (EF) and the remainder of the astrocyte plasma membrane (PM). Since these membrane resistances are dependent on the AQP4 expression level, they are indicated as variable resistances (arrows). Gap junction (GJ) resistances connect the intracellular spaces of two neighbouring astrocytes.

Supplementary Table S1: Rates of water secretion from capillaries in normal and AQP4 knock-out cases for different levels of contribution of secretion to overall water influx. The corresponding pressure drop between arterial and venous paravascular spaces is also reported.

Capillary secretion rate as fraction of overall water inflow rate [%]	Inter-PVSs pressure drop [Pa]	Capillary secretion rate in normal case $[10^{-2}\ \frac{\mu m^3}{s}]$	Capillary secretion rate in AQP4 knock-out case $[\ 10^{-2}\ \frac{\mu m^3}{s}]$
0	226	0	0
20%	202.98	0.91	0.63
40%	180.09	1.82	1.26
60%	157.71	2.72	1.88
80%	134.32	3.63	2.5
100%	111.94	4.54	3.13

Supplementary Information – Solute transport analysis

Relative role of diffusion and advection in solute transport in the tissue and PVS

To evaluate the relative contribution of advection and diffusion to solute transport in the ECS, we consider the non-dimensional Péclet number:

$$Pe = \frac{Lu}{D}, \tag{S1.19}$$

where L is the characteristic length, u is the flow velocity and D is the diffusion coefficient of the solute. For naturally occurring solutes and tracers commonly used to study ISF flow in the brain, D ranges between $5*10^{-11}$ and $5*10^{-10}$ m^2/s [35]. As these solutes are either produced throughout the tissue or injected at a given location in the tissue, we set the diffusion length to half the distance between arterial and venous PVS, namely $L_{AV}/2$. For the ISF flow velocity, there is a range of reported values from $0 - 1\ \frac{\mu m}{min}$ specifically for grey matter[44] to brain averaged values of $5.5 - 14.5\ \frac{\mu m}{min}$ [45]. For the calculation of Pe we consider a range of $1 - 5.5\frac{\mu m}{min}$, where the lower limit is the maximum for grey matter given by Rosenberg et al (Fig. 4 in [44]), and the upper limit the minimum given by [45, 65, 66] for the entire brain. This yields Pe in the range of 0.005 to 0.275 in the ECS. Solute transport in the ECS is thus dominated by diffusion.

For the corresponding analysis in the PVS, we need to determine the bulk flow velocity therein based on the integrated value of water transfer between PVS and parenchyma. We consider a PVS segment

of length corresponding to that of a penetrating arteriole in the rodent cortex, $L_{PVS} = 500\mu m$ [49]. Considering the flow rate from PVS to tissue through a single astrocyte endfoot and its neighbouring inter-endfeet-gap and integrating this value over the length of considered paravascular space using the characteristic dimensions reported in Table 2.2, we obtain

$$u_{PVS} = \frac{L_{PVS}}{(W_{EF}+H_{IEG})} \frac{\pi D_{arteriole}}{L_{EF}} \frac{Q_{unit}}{D_{arteriole}\, H_{PVS}}. \quad \text{(S1.20)}$$

This yields fluid flow velocity between $0.9 - 5\,\frac{\mu m}{s}$ in the PVS velocities of 1 - 5.5 $\boldsymbol{\frac{\mu m}{min}}$ in the ECS. Accordingly, the Péclet number ranges between 0.45 and 25 in the PVS for a diffusion length of half the PVS length, ${L_{PVS}}/{2}$. Advection must thus not be neglected in the PVS, and is the dominant factor in the transport of large solutes such as amyloid beta.

Solute transport capacity in ECS and PVS

We use the metrics of convective and diffusive fluxes to calculate the upper limit of solute transport through ECS and PVS, referring to this limit as solute transport capacity. Convective and diffusive fluxes are defined as:

$$\begin{aligned} J_c &= uAC, \\ J_d &= DA\frac{\partial C}{\partial x}, \end{aligned} \quad \text{(S1.21)}$$

where D is the solute's diffusion coefficient, A the surface area perpendicular to the desired flux direction, C the solute concentration, $\frac{\partial C}{\partial x}$ the concentration gradient in the flux direction and u the fluid velocity.

To compare the PVS and tissue transport capacities, let us consider a segment of PVS of length L_{PVS} as illustrated in Supplementary Fig. S3, and the solute fluxes in and out of that segment. Since solutes could enter the PVS segment from whole the length of it, the diffusion length in PVS is taken as ${L_{PVS}}/{2}$, then the flux of solutes through this segment of PVS is governed by advection and diffusion as follows:

$$J_{PVS} = J_{c\_PVS} + J_{d\_PVS} = u_{PVS}\, P_{PVS}\, H_{PVS}\, C + D\, P_{PVS}\, H_{PVS}\, \frac{C}{{L_{PVS}}/{2}}, \quad \text{(S1.22)}$$

where u_{PVS} is the velocity in the PVS and P_{pvs} and H_{pvs} are the PVS circumference and thickness, respectively. Solutes (metabolites) are produced throughout the tissue and enter the PVS through IEG. Their diffusion length is thus taken as ${L_{AV}}/{2}$. The solute flux from tissue to PVS is then written as:

$$J_{ECS} = J_{c\_ECS} + J_{d\_ECS} = u_{ECS}\, r_{IEG}\, P_{PVS}\, L_{PVS}\, C + D\, r_{IEG}\, P_{PVS}\, L_{PVS}\, \frac{C}{L_{AV}/2}, \qquad \text{(S1.23)}$$

where the product $P_{PVS}L_{PVS}$ is the surface of the PVS segment under consideration and r_{IEG} the proportion of PVS surface covered by IEG which allows the movement of solutes between PVS and tissue.

The ratio of the solute transport capacity in PVS to tissue becomes:

$$\sigma = \frac{J_{PVS}}{J_{ECS}} = \frac{u_{PVS}\, P_{PVS}\, H_{PVS}\, C + D\, P_{PVS}\, H_{PVS}\, \frac{C}{L_{PVS}/2}}{u_{ECS}\, r_{IEG}\, P_{PVS}\, L_{PVS}\, C + D\, r_{IEG}\, P_{PVS}\, L_{PVS}\, \frac{C}{L_{AV}/2}}. \qquad \text{(S1.24)}$$

Since we have already discussed the Péclet number in PVS and ECS, we rewrite the above equation based on this number definition for PVS and ECS:

$$\sigma = \frac{J_{PVS}}{J_{ECS}} = \frac{u_{PVS}\, H_{PVS}\, \left(1 + \frac{1}{Pe_{PVS}}\right)}{\frac{2\, L_{PVS}}{L_{AV}}\, D\, r_{IEG}\, (1 + Pe_{ECS})}. \qquad \text{(S1.25)}$$

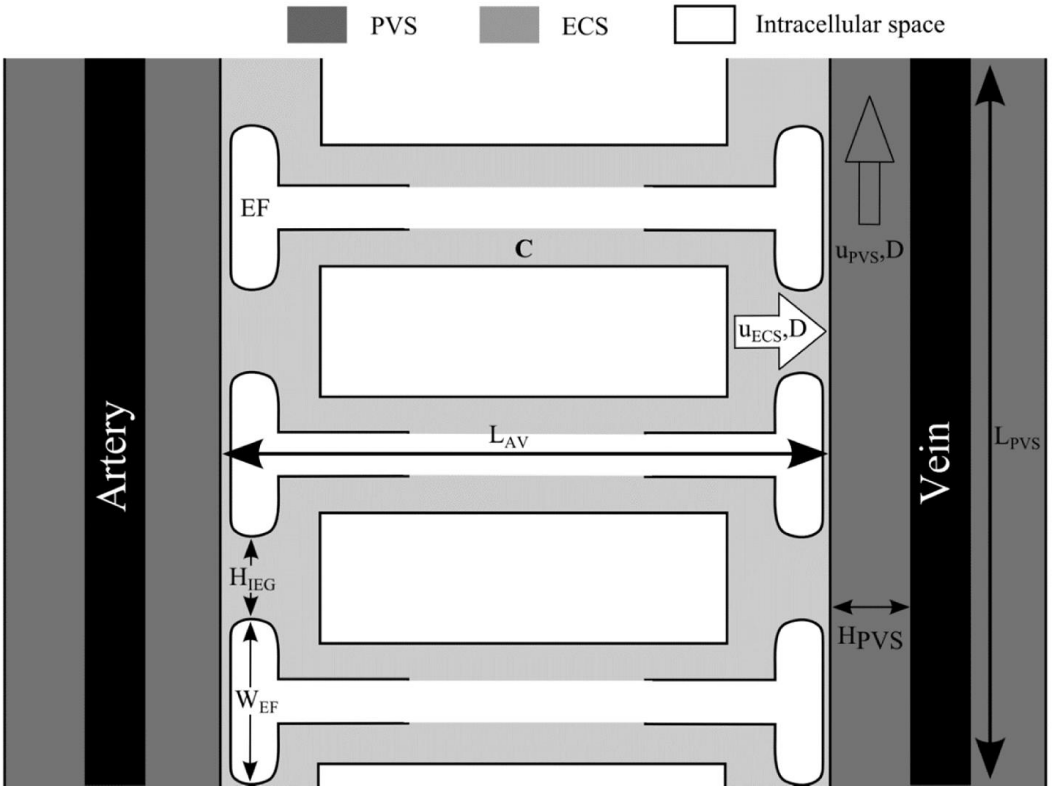

Supplementary Figure S3: Dimensions used to obtain the solute transport capacity ratio in equation (S1.24) and (S1.25). C represents the solute concentration in the center of the tissue.

Solute transport capacity in the awake state

Here we consider the thickness of paravascular space, H_{PVS}, to be 1 µm [19], r_{IEG}=1/25 referring to Table 2.2, $u_{PVS} = 0.9 - 5\ \frac{\mu m}{s}$ as estimated in S2.1, and the diffusion coefficients of natural solutes in the brain and of common tracers, D, to be in the range of $5{*}10^{-11} - 5 * 10^{-10}\frac{m^2}{s}$ [35]. With these values, theadvective to diffusive transport rate ratio ranges between:

$$\sigma = 0.045 - 0.61. \tag{S1.26}$$

In the case of AQP4 knock-out, this ratio decreases due to the 44% reduction in overall water flow rate from PVS to tissue (see Results section):

$$\sigma_{AQP4-/-} = 0.038 - 0.39. \tag{S1.27}$$

Solute transport capacity during sleep

It has been reported that ECS volume increases by 60% in mice during sleep. Based on a 1:4 initial ratio of ECS to intracellular space volume, this translates to a 15% reduction of intracellular volume during sleep. Under the assumption that the volume changes are caused by equal relative changes in all relevant dimensions, the ECS resistance decreases by 46% (equation (S1.3)) while the resistance of the intracellular pathway increases by 25%. The combined effect is an increase of the total flow rate from PVS to tissue by 36% (see Supplementary Fig. S4). The solute transport capacity then ranges between 0.048 – 0.77.

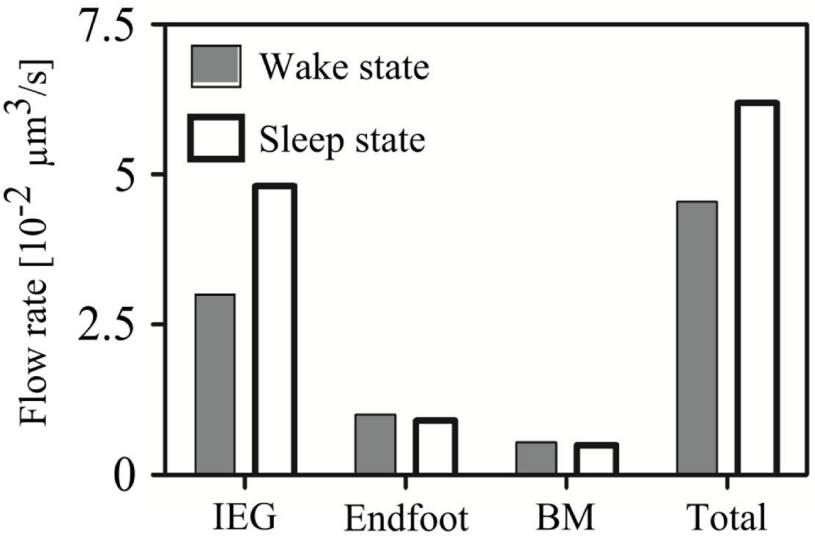

Supplementary Figure S4: Flow rates from PVS to tissue through IEG, endfoot, capillary basement membrane and in total during wake (dark bars) and sleep states (light bars).

Supplementary Information – Sensitivity analyses

We performed sensitivity analyses to ensure that the conclusions drawn in this work are not biased by the choice of model parameter values. Analyses for resistances are summarized in Supplementary Table S2, where flow rates under normal and AQP4 knock-out conditions are reported for the listed upper and lower bounds of parameters. The reported flow rates are normalized by the total flow rate under normal conditions. For the GJ resistance, the upper parameter bound was set to infinity, modelling the absence of GJs, while the lower bound was set to the endfoot membrane resistance, as this is the most water conductive part of the plasma membrane. The intracellular space is not just a fluid filled void; the volume fraction occupied by cell organelles and other solid components that offer resistance to water flow have to be taken into account. Thus, the upper bound of intracellular resistance was set based on the reported approximations of the cytosol volume fraction in glial cells (the corresponding calculations are described in Supplementary Information S1). Other resistances were varied by one order of magnitude in either direction of their respective nominal value.

Supplementary Table S3 summarizes the results of the sensitivity analyses for changes in the baseline ISF velocity based on which the pressure drop between arterial and venous PVS is derived. Since the nominal ISF velocity used in the main text is at the very lower end of the values reported in the literature, we analysed increased velocities up to $5.5\ \frac{\mu m}{min}$. We do not consider higher values to be representative of grey matter, as they are derived from measurements on the entire brain and thus

include the effects of white matter as well as paravascular spaces. While absolute flow rates change, normalized values and their relative change upon AQP4 deletion are not affected. This is due to the linearity of the model for the nominal ISF velocity and inter-PVS pressure drop (in the absence of capillary secretion described in Supplementary Information S1).

Supplementary Table S4 shows the results of sensitivity analyses for different values of capillary water secretion reduction after AQP4 deletion in the expanded model described in Supplementary Information S1. The nominal value for the secretion reduction is 31% based on experimental evidence [47]. As mentioned in the model description, this nominal value is likely too high. We have thus set the lower bound in the sensitivity analysis to 0%, i.e. no reduction in water secretion. The upper bound is set to 50%. The expected reduction of flow rate through the periarterial IEG in the full network of astrocytes after AQP4 deletion and its increase in the incomplete network are reproduced with all levels of secretion reduction as long as the PVS is responsible for at least 60% of the water supply to the parenchyma.

The conclusions drawn in this work are that a) flow rate through IEG is reduced upon AQP4 deletion in a complete astrocyte network and b) that the flow rate is not reduced in an incomplete network without central astrocytes when AQP4 is deleted. The sensitivity analyses reported in Supplementary Tables S2, S3 and S4 show that both observations hold for all considered parameter variations as long as the PVS is the main source of water flux into the parenchyma.

Supplementary Table S2: Sensitivity of the results to changes in resistance values. Results for both full and incomplete networks are provided as flow rates normalized by the corresponding total flow rate under normal conditions.

Resistance		Value $[\frac{Pa}{\mu m^3/s}]$	**Model condition:** Normal or AQP4-/-	Normalized flow rates							
				Full network of astrocytes (6AU)				Incomplete network (2 perivascular AU)			
				IEG	End-foot	BM	Total	IEG	End-foot	BM	Total
R_{ECS} R_{PM} R_{EF} R_{GJ} R_{PR} R_{IEG} R_{BM}	Baseline resistance values	$1.12 * 10^3$ $3.2 * 10^2$ $6.43 * 10^3$ $1.35 * 10^4$ $2.56 * 10^1$ $9.5 * 10^1$ $7.1 * 10^3$	Normal AQP4-/-	0.66 0.46	0.22 0.024	0.11 0.08	1 0.57	0.67 0.76	0.21 0.038	0.12 0.13	1 0.93
R_{ECS}	lower bound	$1.12 * 10^2$	Normal AQP4-/-	0.93 0.83	0.043 0.006	0.27 0.02	1 0.87	0.93 0.95	0.043 0.007	0.03 0.03	1 0.983
	upper bound	$1.12 * 10^4$	Normal AQP4-/-	0.17 0.13	0.53 0.068	0.3 0.18	1 0.37	0.17 0.28	0.04 0.011	0.04 0.05	1 0.90
R_{PM} R_{EF}	lower bound	$3.2 * 10^1$ $6.43 * 10^2$	Normal AQP4-/-	0.25 0.2	0.69 0.095	0.05 0.04	1 0.33	0.25 0.5	0.69 0.23	0.06 0.1	1 0.85
	upper bound	$3.2 * 10^3$ $6.43 * 10^4$	Normal AQP4-/-	0.82 0.73	0.03 0.005	0.14 0.12	1 0.86	0.82 0.84	0.026 0.004	0.14 0.14	1 0.99
R_{GJ}	lower bound	$6.43 * 10^3$	Normal AQP4-/-	0.65 0.47	0.22 0.026	0.12 0.08	1 0.58				
	upper bound	$\rightarrow \infty$	Normal AQP4-/-	0.67 0.45	0.22 0.022	0.12 0.08	1 0.54				
R_{PR}	upper bound	$6.45 * 10^1$	Normal AQP4-/-	0.66 0.48	0.22 0.023	0.12 0.08	1 0.59	0.67 0.76	0.21 0.04	0.12 0.13	1 0.93
R_{IEG}	lower bound	9.5	Normal AQP4-/-	0.67 0.48	0.21 0.021	0.11 0.07	1 0.56	0.68 0.78	0.2 0.038	0.12 0.13	1 0.94
	upper bound	$9.5 * 10^2$	Normal AQP4-/-	0.57 0.42	0.25 0.03	0.16 0.12	1 0.575	0.57 0.68	0.26 0.04	0.17 0.18	1 0.9
R_{BM}	lower bound	$7.1 * 10^2$	Normal AQP4-/-	0.35 0.27	0.13 0.013	0.52 0.41	1 0.7	0.32 0.35	0.1 0.01	0.58 0.59	1 0.96
	upper bound	$7.1 * 10^4$	Normal AQP4-/-	0.74 0.51	0.24 0.026	0.01 0.01	1 0.54	0.75 0.86	0.24 0.04	0.01 0.02	1 0.92

Supplementary Table S3: Sensitivity of the reported flow rates to changes in nominal ISF flow velocity and corresponding inter-PVS pressure drop. Results for both full and incomplete networks are provided as flow rates normalized by the corresponding total flow rate under normal conditions.

V_{ISF}	Inter-PVS Pressure drop [Pa]	**Model condition:** Normal or AQP4-/-	Normalized flow rates							
			Full network of astrocytes (6 AUs)				Incomplete network (2 perivascular AUs)			
			IEG	End-foot	BM	Total	IEG	End-foot	BM	Total
Baseline value $1\ \frac{\mu m}{min}$	226	Normal	0.66	0.22	0.11	1	0.67	0.21	0.12	1
		AQP4-/-	0.46	0.024	0.08	0.57	0.76	0.038	0.13	0.93
$2.5\ \frac{\mu m}{min}$	565	Normal	0.66	0.22	0.11	1	0.67	0.21	0.12	1
		AQP4-/-	0.46	0.024	0.078	0.57	0.76	0.04	0.13	0.93
$5.5\ \frac{\mu m}{min}$	1243	Normal	0.66	0.22	0.11	1	0.67	0.21	0.12	1
		AQP4-/-	0.46	0.024	0.078	0.57	0.76	0.04	0.13	0.93

Supplementary Table S4: Sensitivity of the reported IEG flow rates to changes in capillary water secretion reduction after AQP4 deletion. Results for different capillary secretion rates and for both full and incomplete networks are provided.

			Flow rates through arterial IEG [$\mathbf{10^{-2}}\ \frac{\mu m^3}{s}$]											
			Full network of astrocytes (6 AUs)						Incomplete network (2 perivascular AUs)					
Reduction in capillary water secretion after AQP4-/- [%]		Capillary secretion as fraction of total inflow [%]	0	20	40	60	80	100	0	20	40	60	80	100
		Model condition: Normal or AQP4-/-												
	0	Normal	3	2.4	1.8	1.2	0.6	0	1.4	0.95	0.52	0.08	-0.36	-0.79
		AQP4-/-	2.1	1.53	0.97	0.4	-0.17	-0.73	1.6	1.08	0.57	0.05	-0.47	-0.99
Nominal value	31	Normal	3	2.4	1.8	1.2	0.6	0	1.4	0.95	0.52	0.08	-0.36	-0.79
		AQP4-/-	2.1	1.64	1.18	0.73	0.27	-0.18	1.6	1.19	0.78	0.38	-0.03	-0.44
	50	Normal	3	2.4	1.8	1.2	0.6	0	1.4	0.95	0.52	0.08	-0.36	-0.79
		AQP4-/-	2.1	1.7	1.32	0.93	0.54	0.15	1.6	1.26	0.92	0.58	0.24	-0.1

Chapter 3 Glymphatic solute transport does not require bulk flow

This chapter has been published as:

Asgari, Mahdi, Diane de Zélicourt, and Vartan Kurtcuoglu. "Glymphatic solute transport does not require bulk flow." *Scientific Reports* 6 (2016): 38635.

Abstract

Observations of fast transport of fluorescent tracers in mouse brains have led to the hypothesis of bulk water flow directed from arterial to venous paravascular spaces (PVS) through the cortical interstitium. At the same time, there is evidence for interstitial solute transport by diffusion rather than by directed bulk fluid motion. It has been shown that the two views may be consolidated by intracellular water flow through astrocyte networks combined with mainly diffusive extracellular transport of solutes. This requires the presence of a driving force that has not been determined to date, but for which arterial pulsation has been suggested as the origin. Here we show that arterial pulsation caused by pulse wave propagation is an unlikely origin of this hypothetical driving force. However, we further show that such pulsation may still lead to fast para-arterial solute transport through dispersion, that is, through the combined effect of local mixing and diffusion in the para-arterial space.

Keywords

Computational modeling, dispersion, paravascular transport, glymphatic system, cerebrospinal fluid

Introduction

Recent observations of fast paravascular transport of exogenous fluorescent tracers in the mouse cortex have led to debates about the existence of bulk fluid flow through the brain's extracellular space (ECS) [75]. Such bulk flow, directed from arterial to venous paravascular spaces, has been suggested to play an important role in cerebral metabolite clearance, with more efficient removal of solutes during sleep, and reduced clearance in aquaporin-4 (AQP4) deficient animals [15, 67].

Since cerebral water flow cannot be observed directly *in vivo* with sufficiently high resolution, the spatial and temporal variation of tracers is used as a surrogate marker for fluid motion. If a given tracer distributes more quickly than predicted by its diffusion coefficient, and if the distribution pattern is non-uniform, directed transport of the tracer by bulk water flow is usually suspected [9]. However, similar distribution patterns can also be caused by dispersion without directional bulk flow. Here, dispersion refers to transport of solutes by the combined effect of diffusion and macroscopic fluid motion with zero mean (see Figure 3.1). For instance, cyclic deformation of the human brain induced by cardiovascular and respiratory action induces ventricular cerebrospinal fluid (CSF) motion with close to zero net flow that leads to substantial dispersion [30]. Similarly, dispersion occurs in the spinal canal through oscillatory CSF motion [29].

In the absence of tools for measuring water flow directly, it is not straight forward to determine whether fast solute transport is the result of bulk flow or dispersion. Computational modeling can be used to assess the plausibility of either mode. We have shown previously that under the assumption of a para-arterial to para-venous driving force, the observed fast transport of solutes can be explained by bulk water motion, provided that there is substantial intracellular water flow through astrocytes [76]. It has been suggested, but not demonstrated, that arterial pulsation could generate the required driving force [20, 68].

Here we show using a new set of computational models that arterial pulsations caused by pulse wave propagation are unlikely to generate such driving force. Much rather than being the origin of bulk flow, we demonstrate that arterial pulsation may lead to fast paravascular solute transport by dispersion.

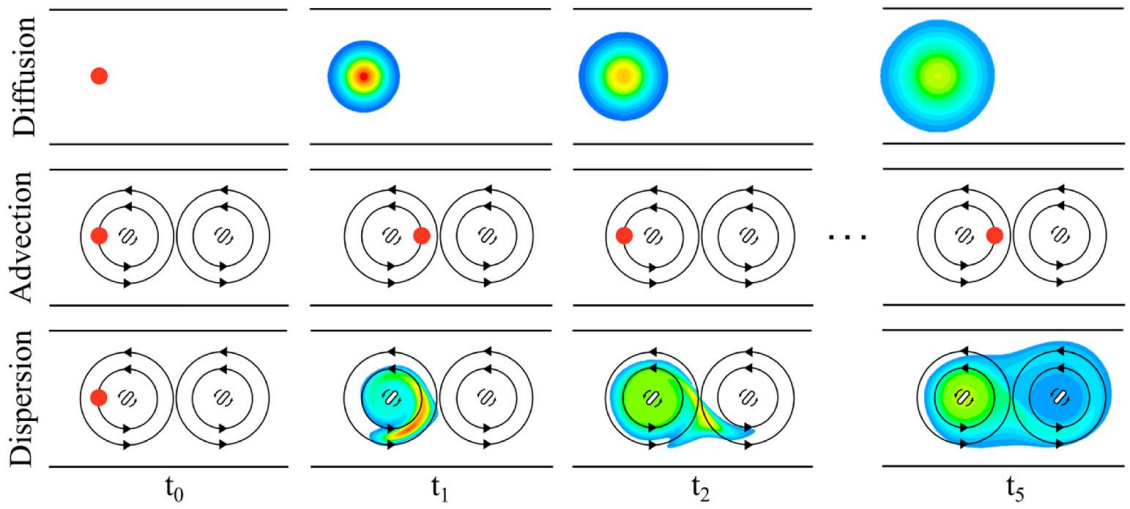

Figure 3.1: Illustration of the differences between solute transport by diffusion, advection and dispersion in the absence of net flow. In this hypothetical setup, which is not meant to represent paravascular transport, a drop of solute (red circle) is injected into a fluid filled channel at time t_0 (left column). In the top row, the fluid is still and the solute may solely be transported by diffusion, whereas in the two other conditions (advection, middle row, and dispersion, bottom row), two stir bars rotating counterclockwise induce a continuous fluid motion with zero net flow. The temporal evolution of the solute concentration (red: high, blue: low concentration, white: no solute) is illustrated in the following columns at equally spaced time points, $t_{i=0\ldots5}$. Pure diffusion leads to slow solute transport. Advection by itself moves the solute much faster, but, in absence of any diffusion, confines the drop to the influence region of the first stir bar. In contrast, the combined effects of advection and diffusion, i.e. dispersion, result in fast solute transport from left to right, even though there is no (time-averaged) net flow of the liquid.

Methods

We designed two distinct computational models: The first one was used to assess the impact of arterial pulsation alone on water and solute dynamics in the para-arterial space. With the second model we explored solute transport from the para-arterial to the para-venous space through the cortical interstitium. All model parameters are listed in Table 3.1.

Table 3.1: Model parameters.

Parameter	Value	Unit	Reference
3D Axisymmetric model of water and solute dynamics in arterial PVS			
Arterial wall distension wave			
Wave amplitude	0.5	μm	[68]
Wave propagation velocity	1	m/s	[28]
Wave frequency	10	$1/s$	[68]
Wavelength	0.1	m	
Dimensions			
Cortical arteriole diameter	23	μm	[68]
PVS model domain length (L)	150-250	μm	[77]
PVS model domain width (W)	10	μm	[15]
PVS domain properties			
PVS hydraulic permeability (K)	$2 \cdot 10^{-12}$	$m^4/N \cdot s$	[28]
PVS porosity (ε)	0.2	-	[28]
Cerebrospinal fluid properties			
Density (ρ)	1000	kg/m^3	[34]
Dynamic viscosity (μ)	0.001	$Pa \cdot s$	[34]
1D model of solute transport in PVS and ECS			
Half-length of the paravascular space of a penetrating vessel	250	μm	[49]
Thickness of the glia limitans	1	μm	[42]
Characteristic distance between arteriole and venule PVS	300	μm	[24]
IEG width	20	nm	[15, 41]
Characteristic ECS channel width	20	nm	[56]
ECS volume fraction (α)	0.2	-	[35]

Model of water and solute dynamics in the para-arterial space

We consider a three-dimensional axisymmetric channel with a pulsating boundary as a simplified representation of a bifurcation free segment of cortical para-arterial space. A two-dimensional illustration of the correspondence between the channel – henceforth referred to as the model domain – and the represented paravascular space segment is shown in Figure 3.2.

The domain length corresponds to the characteristic bifurcation free length of a penetrating arteriole in the mouse cerebral cortex. The total length of a cortical penetrating arteriole is approximately 500 μm [49] (Table 3.1), but the longest bifurcation free segment is clearly shorter [49, 77]. According to Yoshihara et al. [77] and private communications with the senior author of that study, Dr. Kazuto Masamoto, arterioles in the diameter range of 24.2 ± 2.4 μm have an average segment length of 234 μm. To account for variability and to probe the influence of segment length on the reported results, we consider a range of domain lengths from 150 to 250 μm.

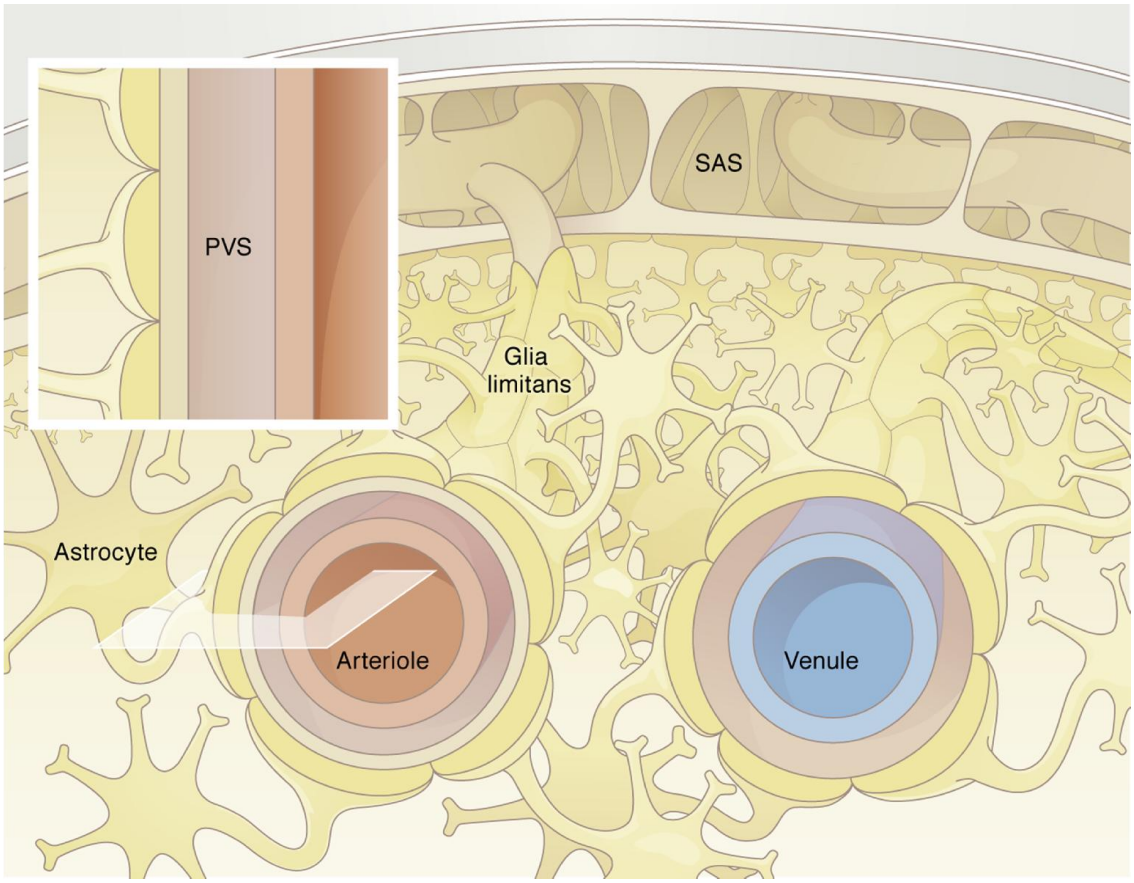

Figure 3.2: Schematic of cerebral arterial and venous paravascular spaces. The arterial PVS extends from the subarachnoid space (SAS) and follows the penetrating vessel into the tissue. This space is restricted on the one side by the vascular wall (endothelial and smooth muscle cells) and on the other side by the glia limitans. Glial endfeet processes almost completely cover the PVS of the larger vessels. The glia limitans of the arterial PVS is attached to the pia matter that extends from the SAS into the parenchyma. The inset shows the section of the arterial PVS retained for the axisymmetric computational model domain.

The model domain is treated as a CSF-filled porous medium. The domain outer boundary, bordered by the glia limitans, is considered stationary. The inner PVS boundary, bordered by the arterial wall, deforms transiently with the passage of pulse waves. The arterial wall motion is derived by normalizing the arterial distension wave function from Fujikura et al. [78] with respect to the diameter of the considered cortical arteriole and applied to the inner boundary of the model domain (Figure 3.3d). To characterize the sensitivity of our findings to the shape of the pulse wave, an alternative, asymmetric motion is derived from this first one by only considering the positive boundary displacements (Figure 3.3e), thereby providing the most favorable condition for pulse wave-induced net flow in the PVS. The hydraulic resistance of the glia limitans layer is three to four orders of magnitude higher than that of the PVS [76]. Accordingly, the outer boundary of the axisymmetric domain is considered impermeable. Zero slip and zero solute flux are imposed on both the inner and outer boundaries. Zero velocity gradient, constant zero pressure and constant solute concentration are imposed at the axial boundaries.

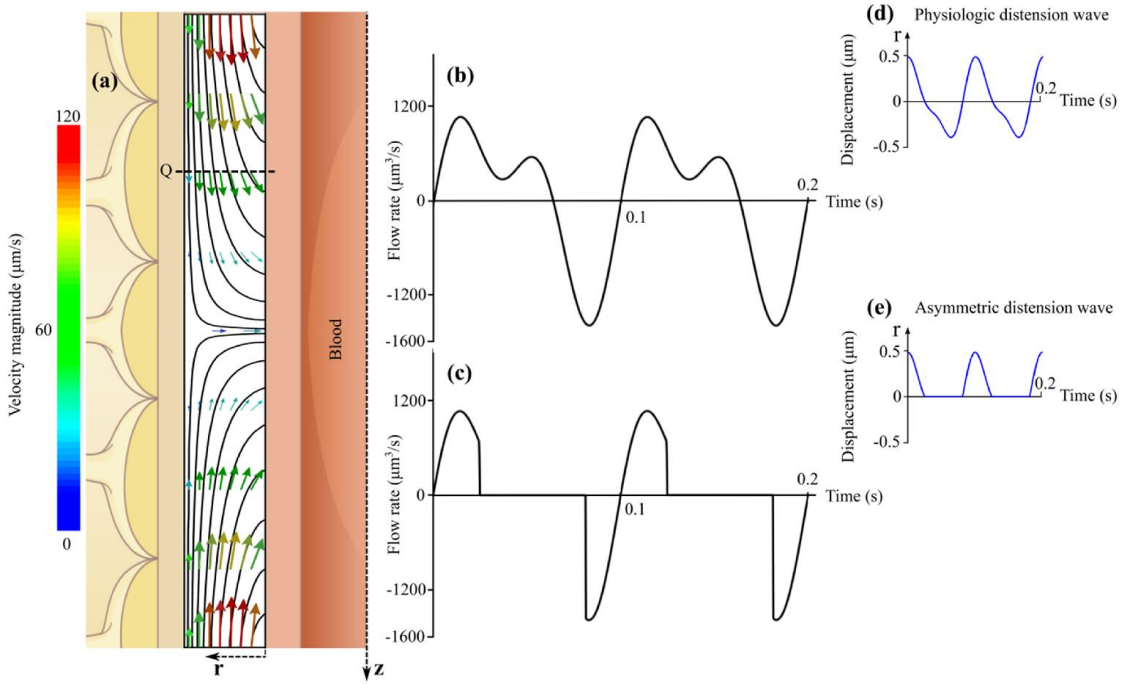

Figure 3.3: Fluid motion induced by vascular pulsation in a representative segment of arterial PVS of 150 μm length and 10 μm width. (a) Illustration of instantaneous flow field in the segment at the beginning of the pulsation cycle as shown in panel d. Depicted are streamlines and velocity vectors color coded according to velocity magnitude. While the highest speed shown in this figure is 120 μm/s, the maximum value reached throughout the cycle is 276 μm/s. (b) Flow rate induced by physiologic arterial pulsation measured at plane Q indicated in panel a. While instantaneous flow rates of up to $1590\ \mu m^3/s$ are observed, the net flow rate averaged over one cycle is only $0.372\ \mu m^3/s$. (c) Flow rate induced by an artificial, asymmetric distension wave as shown in panel e. This wave was derived from the physiologic one shown in panel d by setting all negative displacements to zero. The goal was to obtain the highest possible flow rate without changing the wave amplitude, frequency and length. The net flow rate measured at plane Q is $1.179\ \mu m^3/s$, thus still very small.

The time-dependent equations governing fluid motion and solute transport, namely modified Navier-Stokes with Darcy's law for the porous medium, continuity and advection-diffusion equations, are solved numerically using the open source finite volume code OpenFOAM [79]:

$$\frac{\partial \mathrm{u}}{\partial \mathrm{t}} + (\mathrm{u} \cdot \nabla)\mathrm{u} - \frac{\mu}{\rho}\nabla^2 \mathrm{u} = -\frac{1}{\rho}\nabla \mathrm{P} - \frac{\mu \varepsilon}{\mathrm{K}\rho}\mathrm{u}, \qquad (3.1)$$

$$\nabla \cdot \mathrm{u} = 0, \qquad (3.2)$$

$$\frac{\partial \mathrm{C}}{\partial \mathrm{t}} = (\mathrm{u} \cdot \nabla)\mathrm{C} + \mathrm{D}\nabla^2 \mathrm{C}, \qquad (3.3)$$

where the unknowns u, P and C are fluid velocity, pressure, and solute concentration, respectively. The parameters μ and ρ are, respectively, the dynamic viscosity and density of the cerebrospinal fluid, ε and K the porosity and permeability of the paravascular space, and D the diffusion coefficient of the respective solute. The parameter values are reported in Table 3.1.

Equations (3.1) to (3.3) are discretized using an implicit Euler scheme for the temporal derivatives and central differencing for the first and second order spatial derivatives. All calculations were conducted with a time step size of $5 \cdot 10^{-5}$ s and spatial resolution of $0.25\ \mu m \times 0.5\ \mu m$ along the axial and radial directions, respectively. Grid and time step independence was confirmed.

Dispersion coefficient determination

We postulate that the effect of arterial pulsation on solute transport in a model domain of length L can be approximated by the dispersion equation

$$\frac{\partial \mathrm{C}(x,t)}{\partial \mathrm{t}} = \frac{\partial}{\partial \mathrm{x}}\left(D_L^* \frac{\partial \mathrm{C}(x,t)}{\partial \mathrm{x}}\right), \qquad (3.4)$$

where x is the spatial coordinate in axial direction and D_L^* is the dispersion coefficient in a segment of length L. This equation is structurally equivalent to the well-known diffusion equation in one dimension [35]. To evaluate how closely the dispersion equation captures transport in the arterial PVS, we consider the analytical solution of equation (3.4) in a semi-infinite domain,

$$\frac{\mathrm{C(x,t)}}{\mathrm{C_0(x)}} = \mathrm{erfc}\left(\frac{\mathrm{x}}{2\sqrt{D_L^* \mathrm{t}}}\right), \qquad (3.5)$$

where $\mathrm{C_0}$ is the initial concentration. For a finite domain, this approximation is valid as long as the penetration Fourier number for the domain length remains small [80]. The value of D_L^* is determined by fitting Equation (3.5) to the results of the axisymmetric simulations at t=10s. Using other time points that still fulfill the above Fourier criterion results in the same value of D_L^* (maximum deviation of 1%).

As shown in Figure 3.4, the dispersion equation captures the transport characteristics very well (coefficient of determination: R^2>0.99).

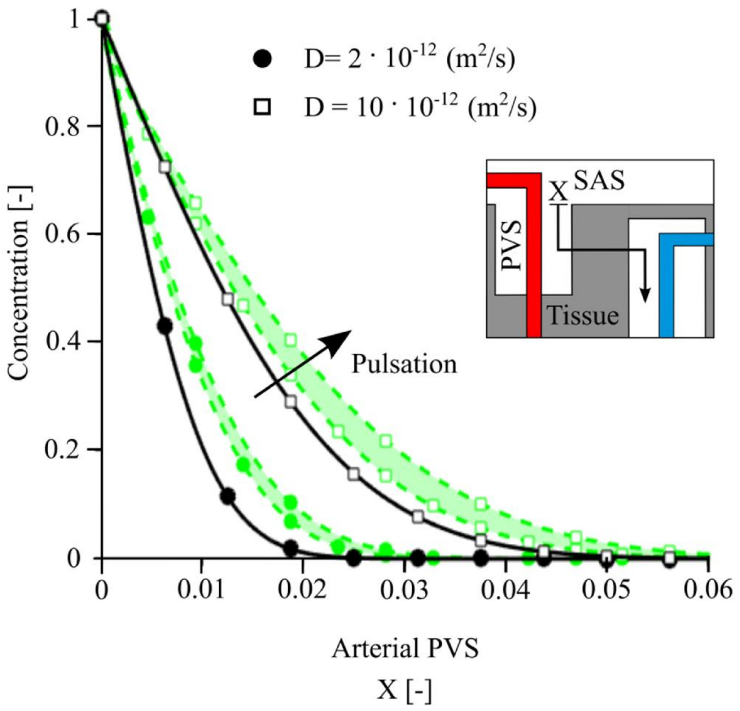

Figure 3.4: Transport of solutes in the arterial PVS in the presence (green lines and symbols) and absence (black lines and symbols) of arterial pulsation. Solutes with diffusion coefficients of 2 · and $10 \cdot 10^{-12}$ m^2/s are considered (circles and squares, respectively). Symbols show the concentration profiles obtained from the 3D axisymmetric simulations 10 seconds after the entrance of solutes from the arterial PVS-SAS interface at X=0. Lines illustrate the best fit curves obtained for the diffusion (continuous black lines) and dispersion (dotted green lines) cases. As dispersion effects depend on domain length, dispersion results are reported for a bifurcation-free arteriole segment length spanning 150 µm (lower bound of the shaded area) to 250 µm (upper bound). The effect of arterial pulsation can be approximated by the analytical solution of the dispersion equation (equation (3.5)) without having to account for pulsation explicitly. Corresponding dispersion curves (dotted lines) obtained using dispersion coefficients of 3.5 · and 4.2 $\cdot 10^{-12}$ m^2/s (lower and upper green circles) and 12.7 · and 17.0 · 10^{-12} m^2/s (lower and upper green squares) accurately reproduce the effect of pulsation (coefficient of determination: R^2>0.99).

Model of solute transport from arterial to venous paravascular space

In the second model, we consider a one-dimensional representation of the solute transport between arterial and venous PVS. Our domain consists of a 250 μm long segment of para-arterial space, associated 1 μm thick segment of glia limitans, 300 μm of cerebral cortical tissue separating the artery-vein pair, and again a 1 μm thick segment of glia limitans and 250 μm of para-venous space. All distances are normalized by the total domain length, where X=0 and 1 correspond to the points where the para-arterial and para-venous spaces, respectively, are exposed to the subarachnoid space (see X-axes of Figures 3.5 and 3.6).

Based on the observations that 1) arterial pulsations yield negligible bulk flow in the physiological regime (Figure 3.3) and 2) the dispersion equation provides a very good approximation of solute transport in the arterial PVS (Figure 3.4), we use equation (3.4) to describe solute transport inside our one-dimensional domain. Across the glia limitans and in the cortical ECS, diffusion dominates due to the high hydraulic resistance of the interstitial pathways [35, 76]. In the venous PVS, pulsations propagating in axial direction are expected to be small, since arterial pulse waves are damped in the capillary bed. Accordingly, we assume that the dispersion coefficient reduces to the effective diffusion coefficient of solutes across the glia limitans and in the cortical ECS and para-venous spaces. In the para-arterial space, we use the dispersion coefficient determined from the axisymmetric simulations.

Large brain metabolites (such as amyloid beta) or tracers (such as Dextran 70) are comparable in size to the characteristic width of the ECS and gaps between astrocyte endfeet (inter-endfeet gaps or IEG) [35] through which they have to pass on their way from PVS to ECS. As a consequence, the effective diffusion coefficient of these larger solutes in their passage through IEG and ECS is lower than that for free diffusion in the same fluid. The relation between effective and free diffusion coefficients is given according to Deen et al. [81] by

$$\frac{\mathrm{D}}{\mathrm{D}'} = \frac{1}{{\lambda_{\theta_0}}^2}(1-\theta)(1-1.004\theta+0.418\theta^3+0.21\theta^4-0.169\theta^5), \qquad (3.6)$$

where D is the effective diffusion coefficient, D' is the corresponding free diffusion coefficient, θ is the size ratio of the solute to the relevant channel or ECS dimension and λ_{θ_0} is the path tortuosity determined for a vanishingly small molecule. This equation is used to determine changes in the effective diffusion coefficient of solutes when dimensions of IEG or ECS are altered, e.g. due to the effects of AQP4 deletion. The equation for solute transport is solved using finite difference discretization in Matlab with a forward Euler time stepping scheme, second order central differences for the spatial second derivatives, a time step size of 0.01 s and a spatial resolution of 1 μm.

Dirichlet boundary conditions for concentrations are imposed on the proximal arterial and distal venous PVS interfaces. The exact anatomical configuration of the venous and arterial PVS is still a matter of debate and investigation. While artery-vein pairs have been depicted to penetrate the cortex from the cranial SAS in close proximity to each other[16], they have, in contrast, also been suggested to have distinctively different starting and end points, with artery and vein penetrating the cortex from different regions of the SAS or only the artery reaching from the SAS into the cortex [13].

We take into account these two anatomical configurations separately to study three distinct cases of solute transport concisely illustrated in the insets of Figure 3.5. Case A represents the second configuration with the vein returning to the SAS at a distinctively different location than where the artery penetrates the cortex. Consequently, there may be different solute concentrations at the arterial PVS inlet and venous PVS outlet. For Cases B and C, the first configuration is used, where the SAS entry and exit locations of the artery and vein PVS are next to each other, and inlet and outlet solute concentrations are thus assumed to be equal at all times.

Cases A and B consider the transport of solutes originating in the cisterna magna, e.g. due to tracer injection. While the solute concentrations at the arterial and venous PVS-SAS interface are equal in Case B, there are different concentrations in the arterial and venous interfaces in Case A due to the mentioned difference in vascular configuration. In both cases, the initial tracer concentration is set to 0 throughout the domain and to 1 at the arterial PVS-SAS interface. Concentration at the venous PVS-SAS interface is set to 0 and 1 in Cases A and B, respectively.

Case C considers the transport of solutes originating in the parenchymal interstitial space. To mimic interstitial tracer injection, the initial solute concentration is set as a rectangular function with the value of 1 in a 50 μm wide section at the center of the considered parenchymal segment and 0 elsewhere. Given the difference in volume between PVS and SAS, solute concentration in the former is assumed to not affect the latter, and the solute concentration is maintained at zero at both arterial and venous PVS boundaries.

Results

Impact of arterial pulsation on water dynamics in the PVS

We interrogated the first model to evaluate whether arterial pulsation may induce bulk flow in the PVS. To this end, we prescribed the axially propagating distension wave shown in Figure 3.3d to the inner boundary of the model domain, and calculated the resulting fluid flow. A representation of the flow field by streamlines and velocity vectors is shown in Figure 3.3a. While rather high instantaneous axial flow rates of up to $1590\ \mu m^3/s$ are reached (Figure 3.3b), their temporal average

over a cardiac cycle is three orders of magnitude lower. This is because the ratio of axial PVS length to the wavelength of the distension wave is very small, approximately $1.5 \cdot 10^{-3}$. Consequently, the arterial wall motion is perceived on a local scale as a uniform radial displacement rather than a peristaltic motion driving CSF forward, and the resulting bulk CSF flow rate in the PVS is $0.372\ \mu m^3/s$. This flow rate is insensitive to variations of the arterial pulsation characteristics within a reasonable range. A change in the distension wave characteristic shape (to make it more asymmetric and thus more likely to produce net flow, Figure 3.3c and Figure 3.3e) only increases the bulk flow rate to $1.179\ \mu m^3/s$. Even when considering the maximum conceivable domain length of 500 μm, which corresponds to the total characteristic length of a penetrating arteriole, considering the lower bound of the wave propagation velocity ($0.1\ m/s$), the upper bound of the mouse heart rate (660 bpm) and high displacement amplitude of 1 μm, we obtain a net bulk flow rate of 3.56 $\mu m^3/s$, which is still negligibly small.

Solute transport in the arterial PVS

We used again the first model to compare the speed of solute transport through the arterial PVS by pure diffusion, pure advection (bulk water flow) and dispersion. We considered solutes with cerebral diffusion coefficients in the range of $2 \cdot 10^{-12}$ to $10 \cdot 10^{-12}\ m^2/s$, which corresponds to larger brain metabolites and to tracers used to study paravascular flow [15, 35].

Table 3.2 lists the distribution length of these solutes determined by first setting the normalized solute concentration to 0 inside the model domain and to 1 at the interface with the SAS, and then measuring after 10 seconds the distance at which the solute concentration in the PVS has reached 50% of the initial SAS value. In the context of pure advection, distribution lengths after 10 seconds are independent of tracer size and two orders of magnitude smaller than with diffusion, reflecting the slow mean bulk flow reported above. In contrast, dispersion yields distribution lengths that are 16% to 50% longer than those obtained with diffusion alone. The effect of dispersion is more pronounced for larger solutes with smaller diffusion coefficients.

Figure 3.4 illustrates the concentration profiles of the two tracers (D= $2 \cdot$ and $10 \cdot 10^{-12}\ m^2/s$) at 10 seconds in the context of dispersion and pure diffusion. This figure re-emphasizes that solutes spread farther under the effect of dispersion than with diffusion alone. Equation (3.5) (dashed lines) provides an excellent approximation of the model results (symbols; coefficient of determination: R^2>0.99). The dispersion coefficient obtained through equation (3.5) depends on the solute considered, but also on the periodic flow induced by the arterial distension wave. The latter is a function of PVS segment length. Calculated dispersion coefficients are given in Table 3.2, and used in the second model to extend our study of solute transport to the brain tissue and venous PVS.

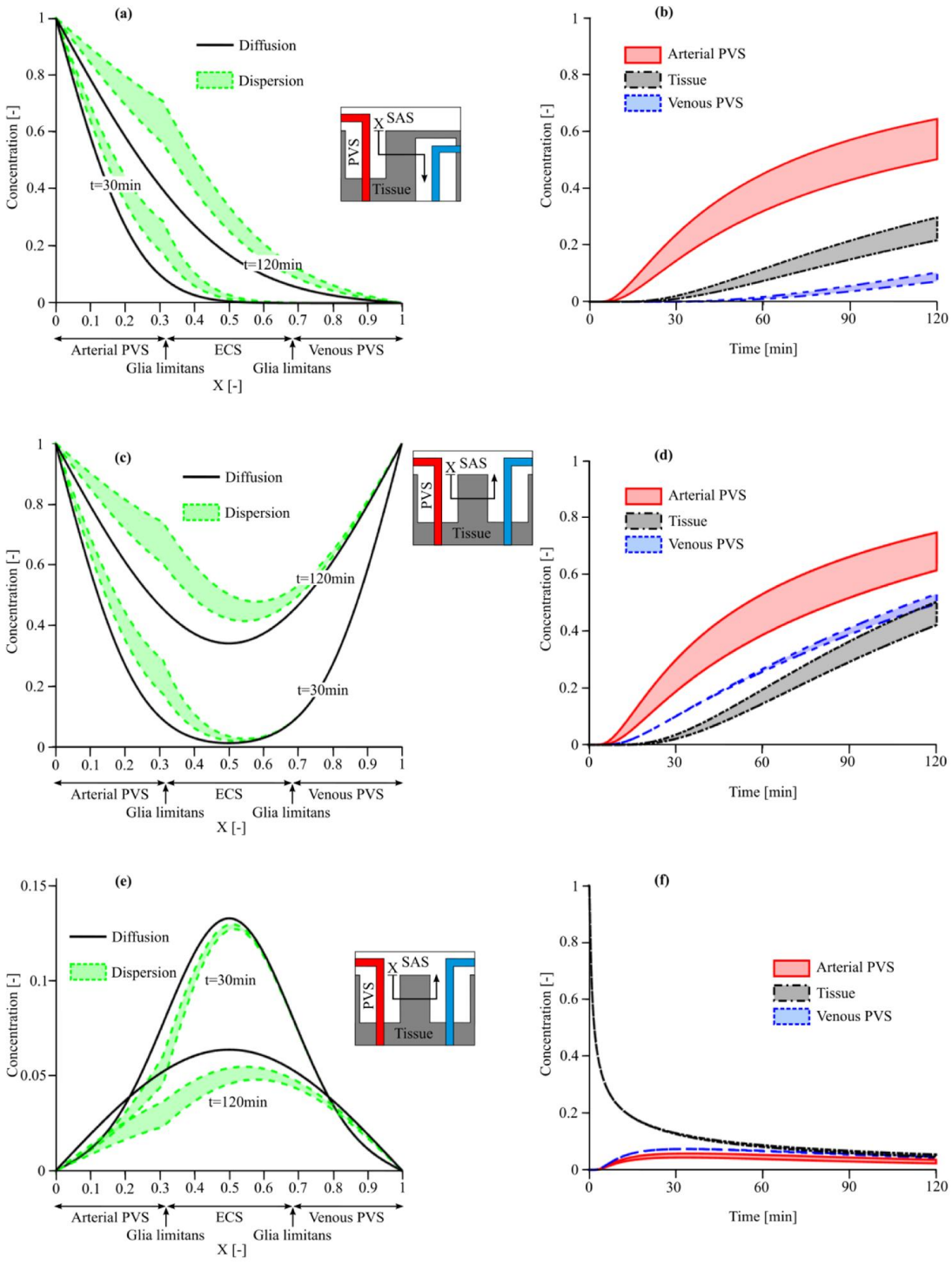

Figure 3.5: Solute transport in the brain for particles of 14 nm size (Dextran 70) with a diffusion coefficient of $6 \cdot 10^{-12}$ m^2/s under three different injection scenarios: (a-b) Case A, cisternal injection with a concentration gradient between arterial and venous PVS interfaces, (c-d) Case B, cisternal injection with no concentration gradient, and (e-f) Case C, interstitial injection. Left column: comparison of the concentration profiles at 30 and 120 mins with dispersion and pure diffusion. Dispersion results (colored bands) represent a range of plausible dispersion coefficients as reported in Table 3.2. Right column: Time evolution of the solute concentration due to dispersion in the arterial PVS (at X=0.3), ECS (X=0.5), and venous PVS (X=0.7).

Table 3.2: Dispersion coefficients and distribution lengths of the three solutes considered in the study. The dispersion coefficient values are reported for PVS segment lengths, L, of 150 and 250 μm. The distribution lengths are determined in the context of pure diffusion, pure advection and dispersion by first setting the normalized solute concentration to 0 in the arterial PVS and 1 in the SAS, and then measuring after 10 seconds the distance at which the solute concentration in the PVS has reached 50% of the initial SAS value.

Diffusion coefficient (m^2/s)	Dispersion coefficient (m^2/s)		Distribution length (μm)			
	L=150 μm	L=250 μm	Diffusion	Advection	Dispersion, L=150 μm	Dispersion, L=250 μm
$2 \cdot 10^{-12}$	$3.5 \cdot 10^{-12}$	$4.2 \cdot 10^{-12}$	4	0.24	5.4	6.0
$6 \cdot 10^{-12}$	$8.1 \cdot 10^{-12}$	$10.7 \cdot 10^{-12}$	7	0.24	8.4	9.3
$10 \cdot 10^{-12}$	$12.7 \cdot 10^{-12}$	$17.0 \cdot 10^{-12}$	9	0.24	10.4	12.0

Solute transport from para-arterial to the para-venous space

We interrogated the second model to assess whether dispersion in the arterial PVS may enhance overall cortical solute transport despite the absence of bulk flow. To that end, we investigated two different injection scenarios: into the cisterna magna (Cases A and B), and directly into the parenchymal interstitium (Case C).

Dispersion caused by arterial pulsation leads, as expected, to faster solute transport in the para-arterial space than pure diffusion (Figure 3.5a). As a result, solutes reach the interface between PVS and tissue faster, which in turn enhances solute transport through the glia limitans and ECS. The higher resistance of glia limitans and ECS to solute passage breaks the smoothness of the graph at the location of the glia limitans. Figure 3.5b shows the corresponding time evolution of the solute concentration in the arterial PVS, tissue and venous PVS. The directionality of the solute transport from arterial PVS to tissue and then venous PVS is reflected by the time shift between the different curves.

The difference in para-arterial and para-venous transport is best seen in Cases B and C (Figure 3.5c-f), where identical concentrations are imposed on the arterial and venous interfaces. When considering pure diffusion, the symmetry of the boundary conditions results in symmetric concentration profiles (Figure 3.5c and e). For cisternal injection, dispersion results in faster penetration along the arterial PVS (Figure 3.5c and d). The slower diffusion in the tissue leads to a large concentration gradient between arterial PVS and tissue for the entire simulated period of 120 minutes. In contrast, solute concentrations in the venous PVS and tissue remain of the same order (Figure 3.5d). For interstitial

injection, dispersion results in faster solute clearance in the arterial PVS (Figure 3.5e) and longer tracer residence times in the venous PVS (Figure 3.5f).

Impact of glia limitans morphology on solute transport

The glia limitans plays a critical role in the system considered. As suggested by *in vivo* observations in AQP4 deficient animals, it may modulate solute transport and fluid fluxes between parenchyma and PVS [15].

Under normal conditions, the inter-endfeet gap between adjacent astrocytes allows for the passage of solutes of up to 20nm hydraulic diameter, while blocking larger ones (see Figure 3.6a). Amiry-Moghaddam et al.[82] and Manley et al.[83] report that AQP4 deletion or depolarization also induce changes in astrocyte endfoot morphology, possibly due to changes in the balance of osmotic forces in intra- and extracellular spaces. Should these morphological changes yield an increase in astrocyte endfeet volume or coverage area, they may concurrently reduce IEG width and thereby the permeability of the glia limitans. To assess whether such hypothetical changes could yield significant changes in the overall rates and patterns of tracer transport, we performed a supplementary set of calculations with reduced permeability of the glia limitans corresponding to a 30% reduction of IEG width from 20 nm to 14 nm. As shown in Figure 3.6b, such reduction in permeability leads to a remarkable reduction of solute transport through the ECS, while transport through PVS stays high. This is in line with observations in AQP4 deficient animals [15].

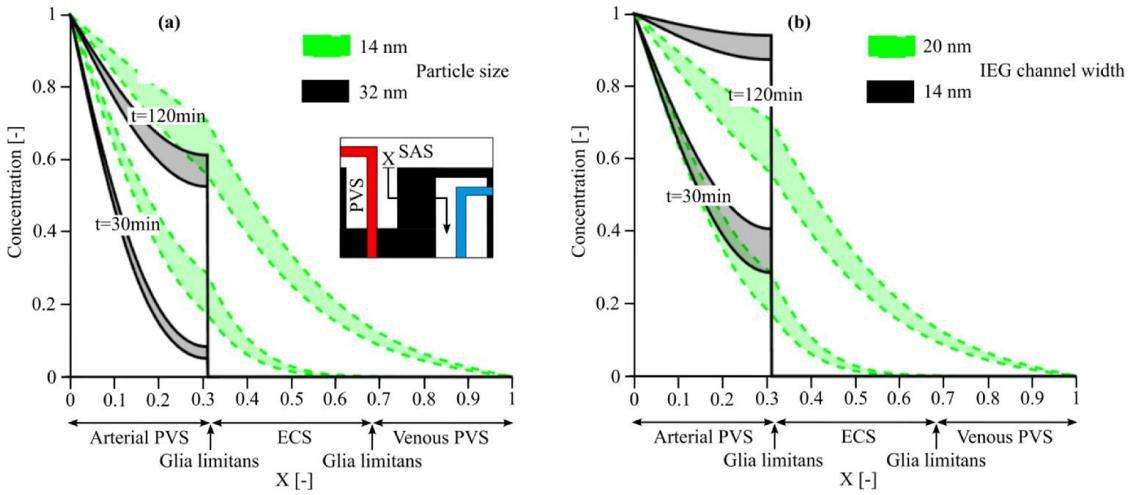

Figure 3.6: Spatial and temporal distribution of the solute concentrations in the brain (a) for two different particle sizes, 14 and 32nm, respectively, assuming an IEG width of 20nm (b) and for the 14nm particle under the effect of IEG width reduction from 20 nm to 14 nm. Results represent a range of plausible dispersion coefficients as reported in Table 3.2. In both cases, the particles enter the arterial PVS from the arterial PVS-SAS interface. While in the normal glia limitans morphology (a) the larger particles (32nm in size) are already trapped by this layer and cannot pass into the parenchyma, reduction of IEG width (b) also inhibits passage of the smaller solute.

Discussion

Cerebral water dynamics cannot be measured *in vivo* with sufficient resolution to support or challenge the hypothesis of cortical paravascular bulk flow. We designed two computational models to fill this gap. The first one was created to test whether arterial pulsations, which have been suggested as possible driving mechanism for bulk flow, can convey solutes at rates demonstrated by tracer studies [15, 18, 21, 84]. The second model was designed to test whether dispersion induced by arterial pulsation may be responsible for the observed fast para-arterial solute transport.

The possibility of pulsation-driven bulk flow through the arterial PVS has been investigated before by computational [26] and analytical modelling [28]. The analytical solution of Wang et al. [28] yields unrealistically high mean PVS velocities on the order of cm/s, and is independent of the distension wavelength. In contrast, Bilston and co-workers came to the conclusion that bulk flow is possible for short distension wavelengths of 20 to 300 μm and decreases as the wavelength increases. However, they did not extend their study to physiologic wavelengths, which are three to four orders of magnitude longer [85]. Our results show that under physiologic conditions, arterial pulsations alone are unlikely to produce notable bulk flow. The absence of bulk flow in the PVS does not imply absence of substantial local fluid motion. Indeed, our results show that arterial pulsation-induced local fluid motion leads to fast solute transport by dispersion even though there is close to zero directed bulk flow. This is in line with observations of reduced solute transport in the PVS after aortic occlusion [20] or internal carotid artery ligation [68], which reduce cerebral arterial pulsation and may thereby reduce dispersion.

The hypothesis of paravascular bulk flow directed from the arterial to the venous side has not yet been reconciled with reports of solute movement in the opposite direction: Both tracers injected into the parenchyma [18, 21] and large endogenous proteins [86] have been shown to spread diffusely through the parenchyma and then drain out along the arterial wall towards the SAS. Arterial paravascular solute transport by dispersion can account for this behavior: Depending on the origin of the solute, fast transport can occur towards (Figure 3.5e) or away (Figure 3.5a, c) from the SAS. Since dispersion is caused by arterial wall pulsation, transport is faster in the arterial than in the venous PVS. This results in faster tracer penetration along the arterial PVS after cisternal injection (Figure 3.5d) or faster clearance of the para-arterial space and longer tracer residence time in the venous PVS after interstitial injection (Figure 3.5f), both of which are in line with *in vivo* observations [15]. Another indication for pulsation-mediated para-arterial transport is the increased deposition of amyloid-beta in the arterial basement membrane of old brains [86]. As arteries stiffen with age, their distension amplitude decreases, thereby reducing dispersion in the arterial PVS and increasing

protein residence time, which may lead to increased deposition. The observation that deposition occurs on the arterial rather than venous side (where transport is slower to begin with) might be explained by higher affinity of amyloid beta to structures in the arterial wall.

The main pillar of the bulk flow hypothesis is that in mice lacking AQP4, tracer transport in the ECS is substantially reduced compared to their wild type counterparts. However, the corresponding experiments also show that transport in the PVS is affected much less [15]. If there is bulk flow from the para-arterial space through the ECS into the venous PVS, the question arises as to how flow in one segment of this chain (ECS) can be reduced substantially while flow in another segment (para-arterial space) is affected only marginally. Indeed, we have shown previously that reduced flow through the ECS necessitates reduced flow in the PVS to be in line with the bulk flow hypothesis [76].

While the alternative hypothesis of paravascular solute transport by dispersion is consistent with observations of limited change in tracer spread in the para-arterial space in AQP4-deficient animals, it does pose challenges with respect to reduced extracellular transport: under the assumption that the deletion of AQP4 has no other effect than increasing trans-membrane resistance to water flux, our model does not predict any reduction in the speed of tracer spread in the ECS because diffusion is dominant in that region [35, 45, 76].

Since neither the bulk flow nor the dispersion hypothesis can fully account for the transport behavior in absence of AQP4, it is necessary to question the premise of no secondary effects caused by the deletion of these water channels. As a matter of fact, there are several reports of changes in parenchymal diffusion and ECS volume fraction caused by AQP4 deletion [87, 88]. However, these studies show increased extracellular diffusion fluxes and ECS volume fraction in animals lacking AQP4, conflicting with studies showing markedly reduced rates of tracer penetration into the parenchyma [15]. This conflict may be resolved by considering how the corresponding studies were carried out: while local ECS diffusion was determined with brain surface photo-bleaching [87] and TMA^+ iontophoresis [88], tracer transport was recorded on a larger scale[15], where the passage of solutes between ECS and PVS through the glia limitans becomes relevant.

The relevant structures for such solute transfer are the astrocyte inter-endfeet gaps. Beyond global changes in ECS volume fraction, there are indications that the endfoot morphology may also be affected by AQP4 deletion or depolarization [82, 83], possibly due to the changed balance of osmotic forces and intra-/extra-cellular volume regulation [89]. These morphological changes may reduce the permeability of the glia limitans. The remarkable reduction of ECS solute transport shown in Figure 3.6 indicates that reasonable morphological changes may limit the transport of small solutes past the

glia limitans, just as this structure limits the transport of larger solutes such as FITC-d2000 under normal conditions [15].

As any model, the two computational representations used in this study have their limitations. First and foremost, we have simplified the cerebral anatomy substantially to three dimensional axisymmetric and one dimensional representations, respectively, and considered the PVS as a homogenous porous medium. It is principally possible that anisotropies in the PVS may act as one-way valves, enabling bulk flow together with arterial pulsation. However, such valves, while introduced as a hypothetical concept [27], have not been found to date. Furthermore, the still debated matter of the venous drainage site limits the definition of exact boundary conditions. To address that difficulty, we characterized solute transport under two extreme scenarios where the solute concentration on the distal venous PVS interface is either null or equal to the proximal arterial one.

Next to anatomical approximations, the issue of uncertain parameters is a recurring challenge in biophysical modeling. We have dealt with it by performing sensitivity analyses to ensure that the conclusions of our study hold within a reasonable parameter range. In particular, the reported dispersion coefficients are independent of the PVS hydraulic conductivity, but depend on instantaneous flow rates and thereby on PVS segment geometry as well as wave characteristics. Importantly, dispersion increases with increasing segment length. We have accounted for this by reporting results for a range of bifurcation free segment lengths of 150-250 μm. While there are both shorter and longer segments in the mouse cerebral cortex, their average length in the diameter range considered here is 234 μm. We chose the upper value of the segment length range purposefully close to this average in order not to overstate the dispersion effect on solute transport in the PVS.

While very limited data exist on the exact pulse waveform in mouse cortical arterioles, our sensitivity analysis indicates that even an extreme asymmetric arterial distension waveform does not produce notable bulk flow. Other waveforms not caused by arterial pulse wave propagation but due to, for example, local cyclic vascular contraction could principally cause bulk flow [90], provided that their wavelengths are orders of magnitude smaller than that of the arterial pulse wave [26]. Otherwise, they would simply increase dispersion. No such waves have been identified to date.

Finally, the modeled effects of possible glia limitans permeability reduction due to AQP4 knock-out need to be viewed as exploratory until corresponding changes to astrocyte endfeet have been shown conclusively *in vivo*. In general, a better characterization of differences in paravascular, interstitial,

intracellular and cerebrospinal fluid pathways between wild type and AQP4 deficient mice is necessary to correctly interpret the results of tracer studies.

In summary, we have shown that arterial pulsations may lead to fast transport along the arterial PVS due to dispersion, but not due to bulk flow. This may reconcile a number of apparently conflicting experimental observations, notably transport in opposite directions in the PVS, i.e. either from the SAS to the parenchyma or the reverse, and faster transport in the arterial PVS compared to the venous one, which the net water flow assumption could not. While the existence of dispersion does not exclude the possibility of bulk flow, the latter would require a yet unidentified driving force as well as substantial intracellular flow through astrocyte networks [76]. Our study shows that arterial pulsation is unlikely to function as that driving force.

Chapter 4 Barrier dysfunction or drainage reduction: Differentiating causes of CSF protein increase?

This chapter has been submitted in the form of a manuscript to the journal of Fluids and Barriers of the CNS

Abstract

Cerebrospinal fluid (CSF) protein analysis is an important element in the diagnostic chain for various central nervous system (CNS) pathologies. Among multiple existing approaches to interpreting measured protein levels, the Reiber diagram is particularly robust with respect to physiological inter-individual variability, as it uses multiple subject-specific anchoring values. Beyond the reliable identification of abnormal protein levels, the Reiber diagram has the potential to elucidate their pathophysiological origin. In particular, both reduction of CSF drainage from the cranio-spinal space as well as dysfunction of the blood-CNS barriers have been suggested as possible causes of increased concentration of blood-derived proteins. However, there is disagreement on which of the two is the true cause. Here we show that high levels of albumin identified in the Reiber diagram are likely to originate from a barrier dysfunction rather than from a reduction in CSF drainage.

Keywords

Computational modeling, cerebrospinal fluid flow, barrier dysfunction, inflammatory diseases, immunoglobulin G, albumin

Introduction

Despite continued advances in non-invasive medical imaging, cerebrospinal fluid (CSF) analysis in general and CSF protein analysis in particular have remained important tools for the diagnosis of various disorders of the central nervous system (CNS) [91]. Yet while it is accepted that abnormal changes in CSF protein content are indicative of pathological conditions, the reasons leading to the measured protein concentrations are often a matter of debate [92].

While some proteins found in the CSF are synthesized within the CNS (choroid plexus, brain and spine) or the meninges, most of them originate in the blood serum under normal conditions [92-94]. They pass through blood-CNS barriers (either the blood-brain barrier, BBB, or blood-CSF barrier, BCSFB) into CNS fluids [95]. Equilibrium between the rate-limited influx of serum derived proteins through these barriers and their efflux with CSF drainage determines the protein content of the CSF [96]. Changes in the concentrations of these proteins may thus reflect alterations in either 1) serum protein levels, 2) intrathecal protein synthesis [97], 3) barrier properties [98], or 4) CSF dynamics and drainage [92].

Since protein levels in the CSF show normal fluctuations as serum protein concentrations change, and since there are inter-individual variations, it is helpful to use relative values for diagnostic purposes. The Reiber diagram constitutes a standardized approach to assessing such values. Should, for example, the immunoglobulin G (IgG) concentration in a patient's CSF sample be analyzed, its relative value with respect to serum IgG concentration (IgG quotient) is compared to the corresponding relative concentration of albumin (albumin quotient). Since albumin is not synthesized in the mature CNS [92], a higher than expected IgG quotient for the given albumin quotient is seen as evidence for intrathecal synthesis of IgG and thus for an inflammatory process in the CNS. When there is no intrathecal immunoglobulin synthesis, Reiber noted a hyperbolic relationship between immunoglobulin and albumin quotients as shown in Figure 4.1, and stated that the albumin quotient should remain below 0.01 for normal subjects [92]. He further defined upper and lower bounds for the relationship between the two quotients, both of which also follow a hyperbolic function, and noted that the relative spread of these bounds, as quantified by a population variation coefficient, remains constant over the entire range of investigated albumin levels (Figure 4.1b).

Of the four possible causes for changes in CSF protein concentration listed above, the Reiber diagram corrects for variations in serum protein levels and identifies intrathecal protein synthesis (see Figure 4.1a). However, it cannot distinguish between changes in CNS barrier properties and changes in CSF dynamics and drainage, both of which have been hypothesized as possible causes for abnormal

albumin quotients [92, 98, 99]. In this study, we have employed a set of computational tools to test these two competing hypotheses.

To this end, we have analysed how changes in barrier function, CSF drainage rates and pulsatility translate to changes of albumin and IgG quotients in the Reiber diagram, where IgG was chosen from the family of immunoglobulins arbitrarily as a common biomarker for inflammatory neurological disorders [100]. Our models reproduce the empirical mathematical relationship between the two quotients given by Reiber, quantify the effect of CSF pulsation on protein distribution and show that barrier dysfunction rather than decreased cerebrospinal fluid drainage is the likely cause of abnormally high albumin values in the Reiber diagram.

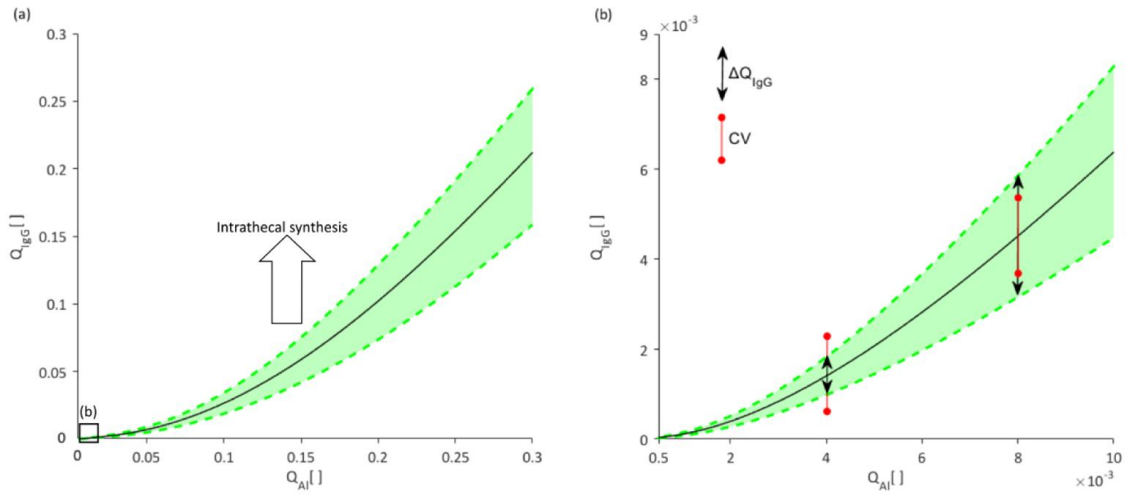

Figure 4.1: Variation of the Immunoglobulin G quotient with that of albumin as depicted in Reiber diagrams. Empirically established relationship between the concentration of IgG in CSF relative to its concentration in blood serum (IgG quotient, Q_{IgG}) and the correspondingly defined albumin quotient (Q_{Al}). Panel (b) depicts the normal range of albumin quotients, corresponding to the area in panel (a) marked with the black square. Reiber demonstrated that the average quotient variation (black line) and upper and lower bounds (green dashed lines) follow the hyperbolic function $Q_{IgG} = \frac{a}{b}\sqrt{{Q_{Al}}^2 + b^2} - c$ [32]. He also showed that the population variation coefficient (CV), defined for a given albumin quotient as $CV = \frac{\Delta Q_{IgG}}{0.5 \cdot \left(Q_{IgG_{upper\ limit}} + Q_{IgG_{lower\ limit}}\right)}$, remains constant over the entire range of investigated albumin quotients. Q_{IgG} values above the upper bound are indicative of a blood-CNS barrier dysfunction.

Methods

We designed two computational models (Figure 4.2) to investigate the mechanisms governing protein distribution in the spinal CSF and underlying reasons for pathological changes in protein levels. With a one-dimensional model (presented second), we evaluate the distribution of albumin and IgG in the spinal CSF, accounting for the protein transport rate across blood-CNS barriers, CSF dynamics (including both dispersion induced by CSF pulsations and advection by mean CSF flow) and CSF drainage from the cranio-spinal space. We also study the impact of pathological changes in barrier permeability, CSF dynamics and drainage on these distributions. The dispersion coefficients used in this one-dimensional model to account for CSF pulsations are determined a priori by computing the axisymmetric three-dimensional CSF dynamics and solute transport in a representative segment of the spinal canal.

Three-dimensional model of protein dispersion induced by CSF pulsation

Dispersion as the combined effect of diffusion and advection by pulsatile fluid motion with zero net flow is the governing mechanism for the faster transport of solutes in the CSF compared to pure diffusion [29, 30, 40, 101]. To determine dispersion coefficients of albumin and IgG along the spine, we first solve the axisymmetric three-dimensional Navier-Stokes equations and associated advection-diffusion equation for protein transport in a segment of the spinal canal.

Model characteristics: The geometry of the spinal canal is idealized as an axisymmetric annular pipe (Figure 4.3c) with dimensions based on statistical geometrical values reported in the literature [102, 103]. The thickness of the spinal subarachnoid space varies from cervical region to lumbar space within the range of 3.5-4.5mm [104]. We have used the mean measured value for this thickness in the model, 4mm [104]. The segment length is chosen to be long enough to avoid the influence of boundary conditions on protein transport rates. All geometrical parameters used are reported in Table 4.1.

The model domain is treated as porous, with permeability and porosity metrics according to literature values for the subarachnoid space [105]. A velocity (flow) boundary condition derived from MRI measurements of spinal CSF [106] is imposed at the inlet boundary (proximal site), while a constant pressure boundary condition is imposed at the outlet (distal site). Both the inner and outer boundaries of the spinal canal are treated as impermeable walls with zero slip and zero solute flux conditions. Constant solute concentration is imposed at the axial boundaries.

Solution methodology: The time-dependent equations governing fluid motion and solute transport, namely modified Navier-Stokes with Darcy's law for the porous medium, continuity and advection-

diffusion equations, are solved numerically using the open source finite volume code OpenFOAM [79]:

$$\frac{\partial \mathrm{u}}{\partial \mathrm{t}} + (\mathrm{u} \cdot \nabla)\mathrm{u} - \frac{\mu}{\rho}\nabla^2 \mathrm{u} = -\frac{1}{\rho}\nabla \mathrm{P} - \frac{\mu\ \varepsilon}{\mathrm{K}\,\rho}\mathrm{u}, \tag{4.1}$$

$$\nabla \cdot \mathrm{u} = 0, \tag{4.2}$$

$$\frac{\partial \mathrm{C}}{\partial \mathrm{t}} = (\mathrm{u} \cdot \nabla)\mathrm{C} + \mathrm{D}\nabla^2 \mathrm{C}, \tag{4.3}$$

where the unknowns u, P and C are, respectively, the fluid velocity, pressure, and protein concentration. The parameters μ and ρ are the dynamic viscosity and density of the cerebrospinal fluid, respectively, ε and K the porosity and permeability of the spinal canal, and D the diffusion coefficient of the respective protein. The permeability of the spinal subarachnoid space is derived using the solution presented by Gupta et al. [107]. The parameter values are reported in Table 4.1.

Equations (4.1) to (4.3) are discretized using an implicit Euler scheme for the temporal derivatives and central differencing for the first and second order spatial derivatives. All calculations are conducted with a time step size of $10^{-4}s$ and spatial resolution of $100\mu m$ in both axial and radial directions. Grid and time-step independence were confirmed.

Evaluation of the dispersion coefficient: The dispersion coefficient may be derived from the above three-dimensional model by fitting the simulated axial concentration with the analytical solution of the dispersion equation in a semi-infinite domain [101]:

$$\frac{\mathrm{C(x,t)}}{\mathrm{C_0(x)}} = \mathrm{erfc}\left(\frac{\mathrm{x}}{2\sqrt{D_L^* \mathrm{t}}}\right), \tag{4.4}$$

where x is the spatial coordinate in axial direction, t is time, $\mathrm{C_0}$ is the initial concentration, and D_L^* is the dispersion coefficient in a segment of length L. For a finite domain, this approximation is valid as long as the penetration Fourier number for the domain length remains small [80]. The value of D_L^* is determined by fitting Equation (4.4) to the results of the axisymmetric simulations at t=8s (10 cycles of pulsations). For further details of the dispersion coefficient evaluation, we refer the reader to [101].

One dimensional model of protein distribution in the spinal CSF

Our one-dimensional domain represents protein transport in the spinal CSF between the lumbar and cervical region. The model domain is illustrated in Figure 4.3, panel (a). We solve the one-

dimensional advection-diffusion equation modified to include sink and source terms representing protein drainage and influx, respectively, as schematically shown in Figure 4.3, panel (b):

$$\frac{\partial C}{\partial t} = \frac{\partial^2 \mathrm{D}^* C}{\partial x^2} + \frac{\partial \mathrm{u} C}{\partial x} + S_i - S_o, \tag{4.5}$$

where C(x,t) is the CSF protein concentration at time t and in axial location x, and u is the CSF bulk flow velocity. D^* is the protein dispersion coefficient induced by CSF pulsation obtained from our three-dimensional model. The source term, S_i, represents the influx of serum proteins into the CSF, while the sink term, S_o, represents protein efflux due to CSF drainage [108]. The dimensions of the domain are reported in Table 4.1.

Evaluation of the dispersion coefficient D:* The dispersion coefficient depends on both the solute considered and the amplitude of the CSF pulsations. The latter has been shown to increase from zero in the lumbar space [109] to a maximum of about 10 mm/s in the cervical region [6]. Accordingly, we applied our three-dimensional model to characterize the dispersion coefficients of albumin and IgG for CSF pulsation amplitudes ranging between 0 and 10 mm/s. The corresponding dispersion values are reported in results section. Expectedly, dispersion equals to diffusion for the pulsation amplitude of zero (i.e. in the lumbar space) and increases for the higher pulsation amplitudes, reaching a maximum for 10 mm/s velocity (i.e. in the cervical space). Since there is an almost linear relation between the imposed velocity and calculated dispersion coefficient, we consider a linear increase of the dispersion coefficient from D^*_{min} equal to the pure diffusion coefficient in the lumbar space to a value of D^*_{max} in the cervical region.

Evaluation of the source term: In absence of active transporters in the blood vessel wall for albumin and immunoglobulins, the only transport mechanism for these larger proteins through the barrier is slow paracellular diffusion [110]. Therefore, the source term for the CSF concentration could be written as:

$$S_i = P_b \cdot (C_{blood} - C), \tag{4.6}$$

where P_b stands for the diffusive permeability of the blood-CNS barriers for the protein under consideration and C_{blood} is the serum protein concentration. The permeability of the barrier to albumin molecules in different regions of the CSF compartments has been measured with radioactive studies [111]. However, it is not known how this permeability might change due to barrier opening. In order to model such permeability variations in pathological situations, we use the membrane pore model described in [96], which was demonstrated to accurately capture barrier permeability for different proteins. In this model, permeability depends on the ratio of protein size to pore size:

$$P_b \propto \left(1-(a/r)\right)^2 \cdot [1-2.1\cdot(a/r)+2.09\cdot(a/r)^3-0.95\cdot(a/r)^5], \quad (4.7)$$

where a and r are protein hydrodynamic radius and pore radius, respectively. These values are reported in Table 4.1. Barrier permeability to IgG molecules can be described in the same way. .

Evaluation of the sink term: Since protein efflux occurs by CSF drainage [108], the protein efflux pathways are the same as for CSF [112]. These include the arachnoid granulations mainly expressed in the cranial space but to a minor extent also in the spinal subarachnoid space, and outflow paths along nerves in both cranial and spinal spaces [113]. Thus, the drainage sink term can be written as

$$S_o = F \cdot C, \quad (4.8)$$

where F is the CSF drainage rate. The total CSF turn-over rate has been estimated to 500 ml/day in humans [5]. However, the distribution of the corresponding drainage between cranial and spinal compartments is not fully known [5], let alone its distribution along the spinal axis. To address this issue, we leverage available data on the spatial distribution of albumin concentrations at steady state, namely the known relative concentrations of albumin in the cisterns, lumbar and cortical subarachnoid spaces, and reported albumin concentration gradients along the spinal subarachnoid space.

At steady state, the average concentration in a given compartment can be derived from Equation (4.5) and is established by the balance of the source and sink terms. Equating the source and sink terms given in Equations (4.6) and (4.8), we obtain the following expression for the albumin quotient, Q_{Al}, in a given CSF compartment [96]:

$$Q_{Al} = \frac{P_{bc}}{P_{bc}+\overline{F_c}}, \quad (4.9)$$

where the subscript c represents the CSF compartment for which Q_{Al} is known, namely the cisterns, cortical or spinal subarachnoid spaces, P_{bc} stands for the barrier permeability in that compartment and $\overline{F_c}$ for the mean CSF drainage rate to be determined. The corresponding results are reported in Table 4.3. The obtained mean drainage characteristics for the spinal compartment, $\overline{F_{spinal}}$, are then employed as baseline for other tested scenarios.

Having calculated the mean CSF drainage rate for the spinal compartment, we determine its local value by making use of reported albumin concentration gradients along the neuraxis. Due to the low CSF turnover rate, sequential sampling of CSF through a lumbar puncture allows one to sequentially access CSF portions from the lumbar, thoracic and finally cervical subarachnoid spaces. Using this

method, a decrease of Q_{Al} was observed from the first 0-3 ml of CSF to the last 27–30 ml of CSF obtained by lumbar puncture [114]. Having an opposite gradient in CSF drainage has been hypothesized as the most probable mechanism for these changing CSF protein concentrations [96]. Accordingly, we assume spinal CSF drainage to increase linearly from zero in the lumbar sac (end of lumbar region) to twice $\overline{F_{spinal}}$ in the cervical region, thereby ensuring that the average spinal drainage matches the above determined value, $\overline{F_{spinal}}$.

Solution method: Equation (4.5) for solute transport is discretized using finite differences in Matlab with a forward Euler time stepping scheme and second order central differences for the spatial second derivatives. Neumann boundary conditions of zero flux for concentrations are imposed on the proximal end of the cervical region and the distal end of the lumbar space. These zero flux boundary conditions are reasonable due to the closed end of the lumbar and the steady-state equilibrium between protein influx and efflux in the lumped compartment of cranial space. The equation is solved with a time-step size of 6s and a spatial resolution of 3.5mm, with confirmed time-step and grid independence.

The Reiber diagram

Reiber showed that a hyperbolic function can describe the relationship between albumin and immunoglobulin quotients seen in a population of patients without intrathecal production of immunoglobulins [32]:

$$Q_{IgG} = \frac{a}{b}\sqrt{{Q_{Al}}^2 + b^2} - c, \tag{4.10}$$

where a, b and c are parameters appropriately chosen to fit the measured patient values. We use this empirical relationship as a reference for the output of the protein distribution.

Reiber further showed that the population variation coefficient, CV, stays constant as the albumin quotient changes. CV is defined as the ratio of the IgG variation to its mean value [32]:

$$\mathrm{CV} = \frac{Q_{IgG_{upper\ limit}} - Q_{IgG_{lower\ limit}}}{0.5 \cdot \left(Q_{IgG_{upper\ limit}} + Q_{IgG_{lower\ limit}}\right)}, \tag{4.11}$$

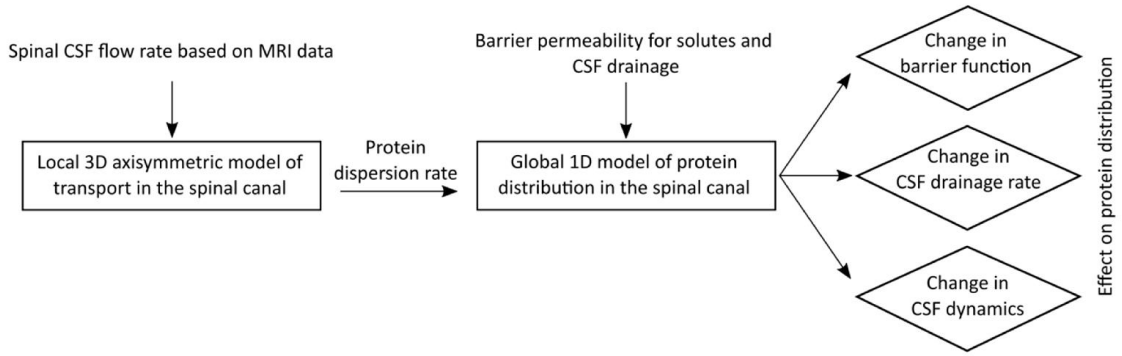

Figure 4.2: Study flow chart. This flow chart describes the application of the two computational models developed to test hypothesis about the cause of increased CSF albumin quotients. The modeling steps and hypotheses are framed by rectangles and rhombi, respectively, while model inputs and outputs are shown without bounding boxes.

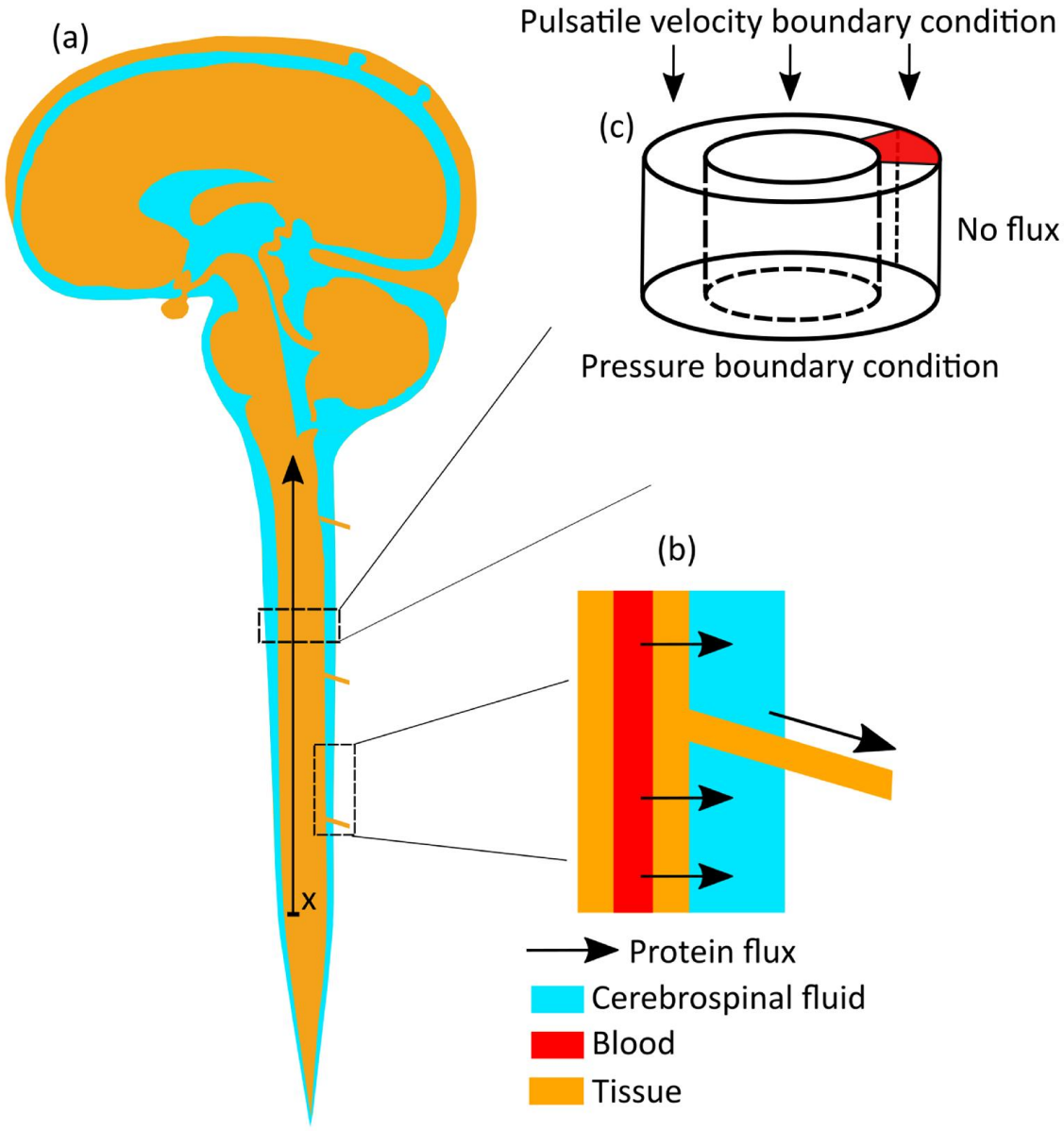

Figure 4.3: Schematic of the model domains. Panel (a) shows a representation of the cerebrospinal fluid compartments. The x and arrow parallel to the spinal cord indicate the anatomic correspondence and orientation of the one-dimensional model. Panel (b) shows protein efflux locations in the spine. Blood-derived proteins pass from blood by diffusion into the CSF space and exit it along nerve roots. Panel (c) shows a representation of the three-dimensional model domain as an annular channel. The boundary conditions for this model are shown on the domain surfaces.

Table 4.1: Model parameters.

Parameter	Value	Reference
Barrier permeability for albumin P_b $[\mu g/min]$		
In the cortical subarachnoid space	29.4	[111]
In the ventricular space	7.6	[111]
In the spinal space	4.8	[111]
CSF compartments volume $[ml]$		
Ventricular space	30	
Cortical subarachnoid space	90	
Spinal subarachnoid space	30	
Protein and pore size used in membrane pore model for barrier permeability $[nm]$		
Pore radius, r	19.4	[96]
Albumin hydrodynamic radius, a_{Al}	3.58	[96]
Immunoglobulin G hydrodynamic radius, a_{IgG}	5.34	[96]
CSF production and drainage rate		
CSF total production and drainage rate, F $[ml/day]$	500	[5]
CSF pulsation		
CSF pulsation amplitude in the cervical region $[mm/s]$	10	[6]
CSF pulsation amplitude in the lumbar region $[mm/s]$	0	[109]
CSF pulsation time period $[s]$	0.8	[6]
CSF physical properties		
Density, ρ $[kg/m^3]$	1000	
Viscosity, μ $[Pa.s]$	0.001	
Spinal canal porosity and permeability		
Porosity, ε	0.99	[107]
Permeability in the longitudinal direction, $K_{longitudinal}$ $[m^2]$	$1.45 \cdot 10^{-7}$	[107]
Permeability in the radial direction, K_{radial} $[m^2]$	$2.36 \cdot 10^{-8}$	[107]
CSF albumin concentrations		
Albumin concentration in the lumbar CSF $[mg/ml]$	0.363	[111]
Albumin CSF/blood quotient in the lumbar space	0.002	[114]
Albumin quotient ratio (lumbar to cisternal)	2	[111]
Albumin quotient ratio (cortical SAS to cisternal)	3	[111]
Dimensions		
Spinal cord diameter in the second model $[mm]$	10	[103, 104]
Spinal subarachnoid space thickness in the second model, w $[mm]$	4	[103, 104]
Spinal segment length in the 3D model domain $[mm]$	100	
Spine length between cistern and lumbar space $[mm]$	700	
Protein properties		
Albumin diffusion coefficient, D_{Al} $[m^2/s]$	$6 \cdot 10^{-11}$	
Immunoglobulin G diffusion coefficient, D_{IgG} $[m^2/s]$	$2.4 \cdot 10^{-11}$	

Results

Transport of the molecules in the spinal canal

We interrogated the 3D axisymmetric model to evaluate protein transport resulting from pulsatile spinal CSF motion. The diffusion coefficients of albumin and IgG in CSF are $6 \cdot 10^{-11}$ and $2.4 \cdot 10^{-11}$ m^2/s, respectively. A peak CSF velocity of 10 mm/s was considered as reference [6]. The resulting dispersion coefficients are summarized in Table 4.2. Since the CSF pulsation amplitude reduces along the spinal canal towards the lumbar space [109], we also calculated the dispersion coefficient for lower velocities. Puy et al. showed that CSF pulsations can change in pathological situations [33], demonstrating an up to four fold increase in amplitude. To evaluate the impact of such pathological variations on protein distribution, we also calculated dispersion coefficients for accordingly increased velocities. We observed an almost linear increase in the dispersion coefficients with increasing velocity amplitude.

Table 4.2: Calculated protein dispersion coefficients.

Molecule	Diffusion coefficient (m^2/s)	Maximum CSF velocity (mm/s)	Dispersion coefficient (m^2/s)
Immunoglobulin G	$2.4 \cdot 10^{-11}$	10	$4.0 \cdot 10^{-8}$
Albumin	$6.0 \cdot 10^{-11}$	2.5	$2.8 \cdot 10^{-9}$
		5	$2.2 \cdot 10^{-8}$
		10	$6.0 \cdot 10^{-8}$
		20	$1.3 \cdot 10^{-7}$
		40	$2.7 \cdot 10^{-7}$

Distribution of albumin and IgG in the spinal CSF: baseline condition

We first determined the distribution of CSF drainage between cortical and spinal spaces as outlined in the Methods section and then calculated albumin and IgG quotients using the one-dimensional model. Drainage distribution and albumin quotients in different regions of the CSF space are summarized in Table 4.3. The distribution of albumin and IgG quotients in the spinal canal between lumbar and cervical regions is shown in Figure 4.4.

Table 4.3: CSF drainage distribution and albumin quotients in different CSF compartments.

CSF drainage distribution	
Cortical region	82%
Spinal region	18%
Albumin quotients in different CSF compartments	
Lumbar spine	0.002
Cortical SAS	0.003
Cistern	0.001

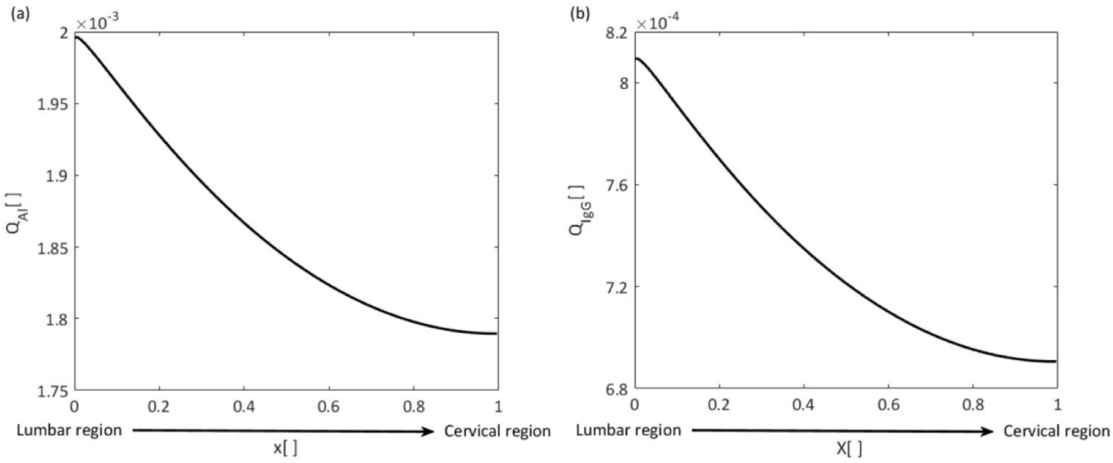

Figure 4.4: Albumin and IgG quotient distribution in the spinal cerebrospinal fluid. x is the normalized location on the rostro-caudal axis from lumbar (x=0) to cervical space (x=1) as illustrated in Figure 4.3, panel (a). Quotients are obtained using spinal CSF drainage rates calculated as outlined in the Methods section. Permeability of the blood-CNS barrier to IgG is obtained using equation (4.7).

Impact of CSF pulsation amplitude change on protein distribution

We employed the 1D model of albumin distribution in conjunction with the dispersion rates obtained using the 3D model of protein transport in the spinal space to assess the effect of changes in CSF pulsation amplitude. We investigated the effect of a factor of four increase in CSF pulsation amplitude observed in chronic hydrocephalus patients [33] and used the corresponding dispersion coefficient calculated in the previous section. Figure 4.5 shows the impact of CSF pulsation amplitude change on the steady state albumin distribution in the spinal CSF. An increase in CSF velocity amplitude results in a more even albumin distribution in the spinal canal, whereas a decrease intensifies the concentration gradient.

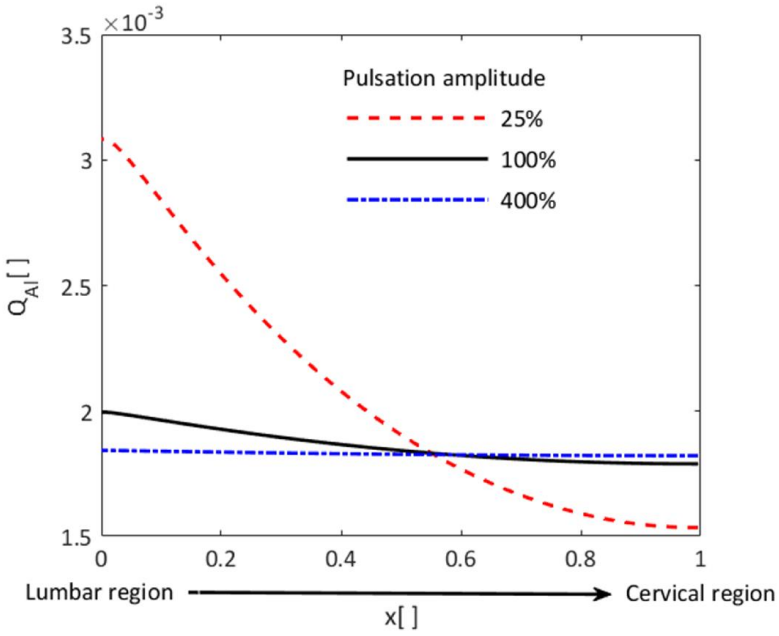

Figure 4.5: Impact of changes in CSF pulsation amplitude on the steady state albumin quotient distribution. x is the normalized location on the rostro-caudal spinal axis from lumbar (x=0) to cervical space (x=1) in Figure 4.3, panel (a). The solid black line represents the nominal condition with CSF velocity amplitude of 10 mm/s (dispersion coefficient of $6 \cdot 10^{-8}\ m^2/s$), the red dashed and blue dashed-dotted lines represent conditions with a factor of four velocity amplitude reduction or increase, respectively (dispersion coefficients: $6 \cdot 10^{-9}\ m^2/s$ and $3.6 \cdot 10^{-7}\ m^2/s$, respectively). Higher CSF velocity amplitudes reduce albumin gradients in the spinal cerebrospinal fluid space.

Impact of barrier dysfunction and CSF drainage on protein quotients

We used the 1D model to investigate the effect of changes in blood-CNS barrier permeability and CSF drainage on albumin and IgG quotients in the lumbar cerebrospinal fluid. Figure 4.6 panel (a) shows the relationship between IgG and albumin quotients in the cases of barrier permeability change (circles) and CSF drainage rate change (solid black line). An albumin quotient of 0.002 is taken as the nominal value. Decrease in CSF drainage and increase in barrier permeability lead to increased IgG and albumin quotients, and vice versa. The empirical hyperbolic relation between albumin and IgG quotients derived by Reiber [92] from measurements in patients' CSF samples is shown to match well with our calculations for barrier permeability change (solid red line).

Figure 4.6 panel (b) illustrates the effect of change in barrier permeability for three different constant CSF drainage rates. The center (dashed) curve corresponds to nominal drainage, while the upper and lower solid curves correspond to 30% increased and decreased drainage rates, respectively. All three curves are hyperbolic. We used the upper and lower curves to calculate representations of the population variation coefficient, obtaining values of 0.48, 0.44 and 0.4 for albumin quotients of 0.001, 0.002 and 0.003, respectively. Note that the population variation coefficient determined by Reiber based on patient data is constant over a range of albumin quotients.

Figure 4.6 panel (c) illustrates the effect of change in barrier permeability for three different baseline IgG permeabilites, reflecting the variation of the barrier permeability to IgG to different extent than for albumin as shown by Seyfert et al. [115]. The center (dashed) curve corresponds to nominal baseline IgG permeability, while the upper and lower solid curves correspond to 30% increased and decreased baseline IgG permeability, respectively. The representation of the population variation coefficient is in this case 0.6 for all albumin quotients.

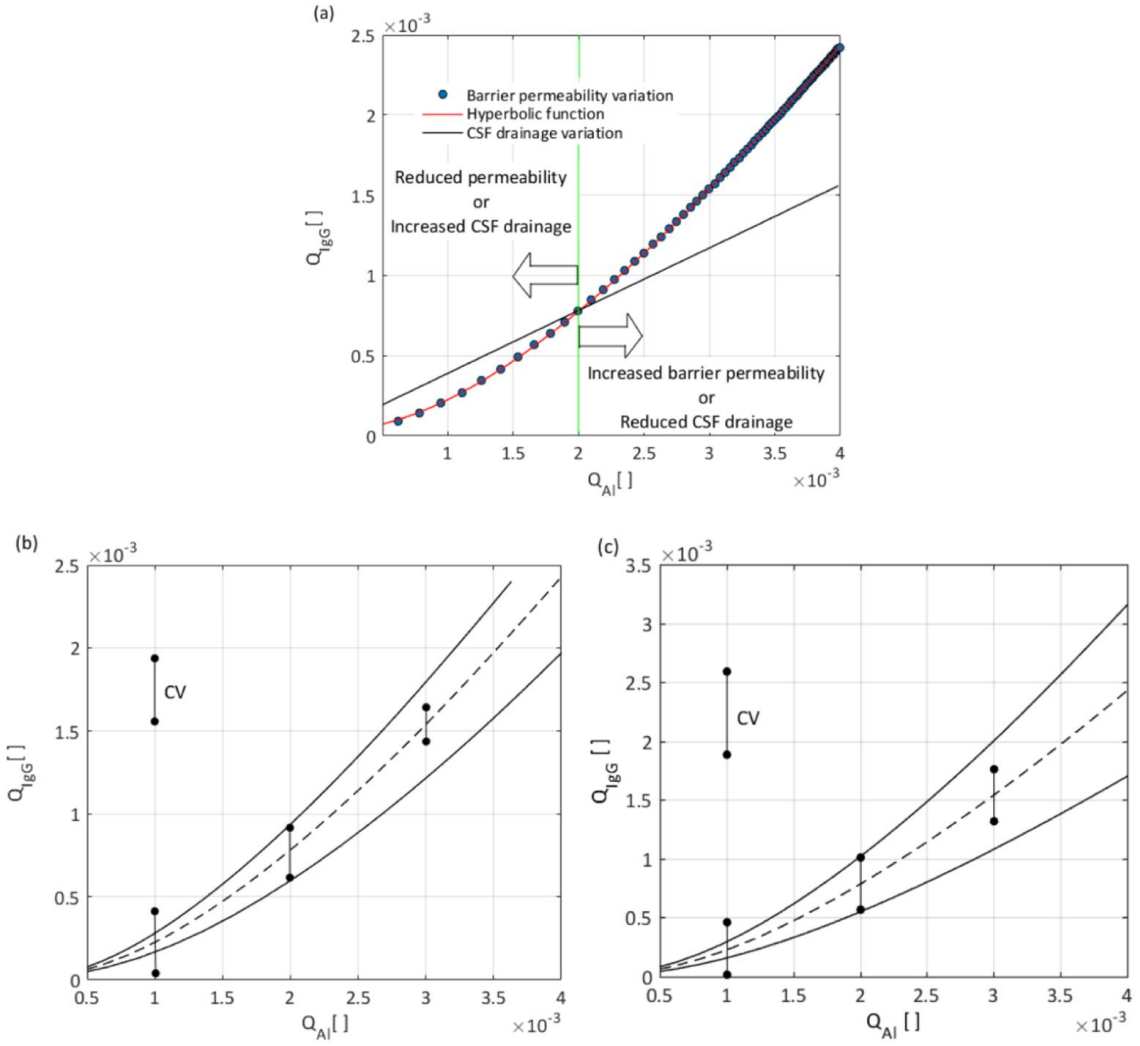

Figure 4.6: Relationship between IgG quotient and albumin quotient as commonly shown in the Reiber diagram. Panel (a): Blue circles show how isolated changes in barrier permeability shape the relation between IgG and albumin quotients, while the black solid line demonstrates the corresponding effect of isolated changes in CSF drainage rate. The albumin quotient of 0.002 is taken as the nominal value. Decrease in CSF drainage and increase in barrier permeability lead to increased IgG and albumin quotients, and vice versa. Quotient variations due to changes in barrier permeability are perfectly described by the hyperbolic function (Eq. 10) empirically derived by Reiber (red solid line, $R_{square} = 1$). In contrast, quotient variations due to changes in CSF drainage follow a linear trend. Panel (b) shows quotient variation due to barrier permeability change. The dashed line represents nominal CSF drainage conditions, while the upper and lower solid lines are representative of 30% increased and decreased CSF drainage rates, respectively. The population variation coefficient for albumin quotients of 0.001, 0.002, 0.003 is, respectively, 0.48, 0.44 and 0.4. Panel (c) shows the effect of barrier permeability change for three different baseline IgG permeabilities. The dashed line represents the nominal IgG permeability and upper and lower solid lines represent 30% increased and decreased IgG baseline permeability, respectively. The calculated variation coefficient is constant (with a value of 0.6) for all albumin quotients.

Discussion

The biochemical analysis of the cerebrospinal fluid is an important diagnostic tool for pathologies of the CNS. For example, changes in CSF immunoglobulin content can be indicative of inflammatory reactions in the brain. To account for inter-individual and normal intra-individual variability, it is advantageous to assess relative rather than absolute values of protein concentration as done in the Reiber diagram. While the Reiber diagram can indicate intrathecal synthesis of proteins, it is debated whether higher than normal readings of relative albumin concentrations are indicative of CNS barrier dysfunction or reduction in CSF drainage. Here we have employed a set of computational models to assess which one of these two changes is the more likely cause of increased albumin concentration in CSF relative to that in the blood plasma.

The Reiber diagram features a hyperbolic relationship between albumin quotient and, for example, IgG quotient, where 'quotient' refers to the concentration of the respective protein in CSF relative to its concentration in blood plasma. Reiber derived this empirical relationship from measurements in a large set of patients in which intrathecal synthesis of the protein of interest could be excluded. He hypothesized that this non-linear relationship was caused by inter-patient variability in CSF drainage rates [32]. However, as shown in Figure 4.6, panel (a), our models indicate that variations in the rate of CSF drainage would yield a linear relationship between the quotients rather than the experimentally determined hyperbolic one. Reiber also calculated the variation coefficient for his patient database and found it to be constant for a large range of albumin quotients. Our calculations show that the variation coefficient does not stay constant for different baseline CSF drainage values (Figure 4.6 panel (b)), indicating that inter-patient variability in CSF drainage alone may not result in the protein quotient relationship observed by Reiber. One should thus not, without further case-dependent evidence, attribute abnormally high albumin quotients identified in the Reiber diagram to reduced CSF drainage.

Others have attributed increased albumin quotients to blood-CNS barrier dysfunction. Indeed, as shown in Figure 4.6, panel (a), variation in barrier permeability leads to the expected hyperbolic relationship between protein quotients. This is further confirmed by a constant population variation coefficient as illustrated in panel (c) for different baseline IgG permeabilities. Consequently, high albumin quotients identified in the Reiber diagram may be seen as indicative of a CNS barrier dysfunction.

Our calculations of the distribution of CSF efflux indicate 18% drainage in the spinal compartment and 82% drainage in the cranial compartment. This distribution matches well with the measurements of Marmarou et al. [116] in cats, where absorption in the spinal space accounted for 16% of the total

CSF drainage and the cranial space contributed 84%. Similar results were obtained by Gehlen et al. using a lumped parameter model of coupled cardiovascular and CSF dynamics [117]. Albumin quotients calculated based on this drainage distribution are within the range of values obtained experimentally in healthy subjects [114].

Seyfert et al. measured albumin and immunoglobulin concentration gradients in the spinal CSF by sequential CSF sampling through lumbar puncture. They showed a decreasing protein concentration profile from lumbar to cervical space [114]. It was hypothesized that this concentration gradient results from the variation of CSF drainage along the spine [96]. Our calculations show that the hypothesized drainage gradient along the spinal canal with minimum drainage rate in the lumbar space would, indeed, result in a longitudinal concentration gradient for albumin and IgG (Figure 4.4). Therefore, our results support the existence of rostro-caudally decreasing spinal CSF drainage.

Puy et al. correlated the magnitude of CSF pulsation with protein distribution in different CSF compartments [33]. We calculated the dispersion rate of albumin in the spinal CSF for different pulsation amplitudes as reported in Table 4.2, and employed these values in our global protein distribution model. Increased CSF pulsation diminishes the longitudinal concentration gradient, while reduced pulsation intensifies it in the spinal canal (Figure 4.5). These results are in line with the measurements of Puy et al. [33]. Therefore, changed CSF dynamics in pathologies such as hydrocephalus and Chiari malformation could have an impact on protein distribution in the spinal canal.

The two computational models developed in this study have the following main limitations: First and foremost, we have simplified the spinal canal anatomy substantially to a 3D axisymmetric annular conduit and a 1D representation, respectively, considering the spinal subarachnoid space as a porous medium. Both the macroscopic anatomy as well as the microanatomy of the CSF spaces as defined by, e.g., arachnoid trabeculae, could play an important role in fluid and solute dynamics. Neglecting the microanatomy can lead to discrepancies between computed and measured metrics of spinal CSF dynamics [106]. In our models, the effect of microstructures is approximated by the introduction of anisotropic permeability of the porous medium representing the spinal subarachnoid space.

The second main limitation pertains to the issue of parameter uncertainty. For instance, we have considered the overall CSF drainage rate to be equal to the estimated value of CSF production, which itself is only known approximatively [5]. We have dealt with parameter uncertainty by performing sensitivity analyses, which show that our main conclusions are robust with respect to reasonable variations of the model parameters. Concretely, we have shown that the hyperbolic protein quotient function in the Reiber diagram that results from variation in barrier permeability does not depend on

baseline CSF drainage (Figure 4.6, panel b) or IgG permeability values (Figure 4.6, panel c). We have also made sure that the population variation coefficient does not only stay constant for a 30% change in IgG baseline permeability (Figure 4.6 panel c), but also for much larger and smaller changes (up to 100% change). Finally, we checked that the derived dispersion coefficients do not depend on the computational domain length and hydraulic conductivity of the domain.

Chapter 5 Conclusion and outlook

The focus of this doctoral thesis is on the impact of the cerebrospinal fluid dynamics on solutes transport and distribution in the central nervous system. The first part of the thesis including chapters 2 and 3 was dedicated to micro-scale solutes transport mechanisms in the cerebral paravascular and extracellular pathways. The second part (chapter 4) discusses the macro-scale transport of proteins and their distribution in the spinal subarachnoid space.

As indicated in chapter 2, diffusion is the main mode of solutes transport in the parenchymal extracellular pathways. With the assumption of bulk flow between arterial and venous paravascular spaces, astrocyte networks could facilitate water flow that enhance metabolite clearance through a parallel, extracellular route. Reduced solutes clearance in animals lacking AQP4 may be explained by diminished bulk flow caused by inhibition of the interconnection between the astrocyte networks and the extracellular route. However, the question remains as to whether there exists any bulk flow in the brain parenchyma and paravascular network or not. The potential CSF bulk flow in the paravascular space requires the presence of a driving force that has not been determined to date, but for which arterial pulsation has been suggested as the origin. In chapter 3, we have shown that arterial pulsations may lead to fast solutes transport along the arterial PVS due to dispersion, but not due to bulk flow. Dispersion may also reconcile a number of apparently conflicting experimental observations, notably transport in opposite directions in the PVS, i.e. either from the SAS to the parenchyma or the reverse, and faster transport in the arterial PVS compared to the venous one, which the net CSF flow assumption could not. While the existence of dispersion does not exclude the possibility of bulk flow, the latter would require a yet unidentified driving force as well as substantial intracellular flow through astrocyte networks as shown in chapter 2.

In chapter 4, we extended our study to investigate the importance of the macro-scale cerebrospinal fluid dynamics for solutes transport and distribution in the spinal subarachnoid space. We showed that CSF protein levels depend on the characteristics of the blood-CNS barrier, i.e. its permeability and structure, but also rely on the dynamics of the cerebrospinal fluid in the vicinity of the barrier. Pathological changes including barrier dysfunction and CSF flow drainage change might result in the variation of proteins level. With the use of computational models, we also demonstrated that barrier dysfunction could explain the protein variation characteristics observed in the Reiber diagram.

This thesis underscores the capabilities of computational modeling to investigate the physiological aspects of water and solutes transport in the brain. The limitations of the state of the art experimental techniques sometimes hinder concrete conclusions about water and solutes transport pathways. One good example for such complication in the experiments interpretation is paravascular

solute transport. For long time in spite of pool of experimental observations, scientists have been questioning the direction and type of transport in the cerebral paravascular space. Part of this complication raises from the fact that single water molecules could not be traced experimentally. Thus, water movement is only inferred from the larger tracer molecules movement. As we showed in chapter 3, fast tracer movement has nothing to show about the bulk water dynamics as mostly interpreted from the experiments. This example and other parts of this thesis indicate that computational modelling could play an important role in filtering biological hypotheses and assess their feasibility with biophysical rules.

Outlook

There are still lots of aspects of our subject of interest "water and solutes dynamics in the central nervous system" which could potentially attract extensive research and scientific work. In spite of massive work done to understand the cerebral transport mechanisms which is partly referenced in this thesis, there is still lack of experimental data which hampers improving the computational models. In this section, I list some which may warrant further research to confirm or infirm hypotheses made herein and help advance models of water and solutes transport in the central nervous system.

Our developed computational models as any other model have their limitations which are clearly stated in each chapter. Simplification of the anatomy is a common aspect of biological models which is also employed in this study for astrocyte cells, extracellular pathways, paravascular spaces and also spinal subarachnoid space. Such simplifications are done due to lack of thorough anatomical knowledge of several features such as sophisticated geometry of astrocytes, three dimensional reconstruction of paravascular spaces and complex micro anatomy of arachnoid trabeculae in the spinal subarachnoid space. To address this difficulty we conducted throough sensitivity analyses to ensure that the conclusions derived in this thesis do not depend on the choice of model parameters and hold true for a reasonable variation of the parameters around the chosen value. However, there is this hope that with the progress in imaging techniques and resolution, it will be possible to resolve the complicated anatomical features such as the three-dimensional morphology of the cell and its processes. This progress would allow for the analysis of transport mechanisms in correct biological morphologies which might add to our knowledge about central nervous system and its functioning.

The available experimental data for micro-scale or cellular level transport pathways in the brain is very rare and mostly qualitative. Our numerical models indicate that cellular transport could be of high importance for the water and metabolites transport in the brain tissue. However, what happens to water and solutes moving through the intracellular pathways is not experimentally clear.

Concerning the new evidences raised in the literature on the significance of the molecular and cellular transport pathways, it seems crucial for the relevant scientific community to move in this direction and look at these aspects experimentally in more details. For instance, water and solutes transport in cellular networks in the brain as discussed for the astrocytes network in chapter 2 could be a potentially high impact research for the successors.

In addition to the having more detailed information on the morphology of biological structures, transport pathways and cellular networks in the central nervous system, a better understanding of the brain mechanics is also crucial for numerical modelling of the brain. As we demonstrated in chapter 4, brain tissue motion could affect brain water and solutes transport largely. However, brain motion in micro-scales is not thoroughly investigated. For instance, tissue motion in vicinity of the paravascular space in the glial endfeet layer could play an important role for solutes transport in the PVS. Since we did not have access to such data, we assumed no motion in this region and reported the rate of solutes dispersion only under arterial pulsations neglecting tissue pulsations in the perivascular region which should be a low extreme value for the dispersion rate.

References

1. WE Dandy and KD Blackfan. An experimental and clinical study of internal hydrocephalus. J Amer Med Assoc. 1913; 61:2216-2217.
2. LH Weed. Studies on Cerebro-Spinal Fluid. No. II : The Theories of Drainage of Cerebro-Spinal Fluid with an Analysis of the Methods of Investigation. J Med Res. 1914; 31(1):21-49.
3. JE Levine, JT Povlishock, and DP Becker. The morphological correlates of primate cerebrospinal fluid absorption. Brain Res. 1982; 241(1):31-41.
4. TH Milhorat. The third circulation revisited. J Neurosurg. 1975; 42(6):628-45.
5. T Brinker, E Stopa, J Morrison, and P Klinge. A new look at cerebrospinal fluid circulation. Fluids Barriers CNS. 2014; 11:10.
6. SH Pahlavian, AC Bunck, F Loth, RS Tubbs, T Yiallourou, et al. Characterization of the discrepancies between four-dimensional phase-contrast magnetic resonance imaging and in-silico simulations of cerebrospinal fluid dynamics. Journal of biomechanical engineering. 2015; 137(5):051002.
7. M Pollay and F Curl. Secretion of cerebrospinal fluid by the ventricular ependyma of the rabbit. Am J Physiol. 1967; 213(4):1031-8.
8. MW Bradbury. Physiopathology of the blood-brain barrier. Adv Exp Med Biol. 1976; 69:507-16.
9. H Cserr and C Patlak. Secretion and bulk flow of interstitial fluid, in: Physiology and pharmacology of the blood-brain barrier. Springer; 1992. p. 245-261.
10. JG McComb. Recent research into the nature of cerebrospinal fluid formation and absorption. J Neurosurg. 1983; 59(3):369-83.
11. A Louveau, I Smirnov, TJ Keyes, JD Eccles, SJ Rouhani, et al. Structural and functional features of central nervous system lymphatic vessels. Nature. 2015; 523(7560):337-41.
12. WG Bradley, Jr., D Scalzo, J Queralt, WN Nitz, DJ Atkinson, et al. Normal-pressure hydrocephalus: evaluation with cerebrospinal fluid flow measurements at MR imaging. Radiology. 1996; 198(2):523-9.
13. B Battal, M Kocaoglu, N Bulakbasi, G Husmen, HT Sanal, et al. Cerebrospinal fluid flow imaging by using phase-contrast MR technique. Brit J Radiol. 2011; 84(1004):758-765.
14. R Faubel, C Westendorf, E Bodenschatz, and G Eichele. Cilia-based flow network in the brain ventricles. Science. 2016; 353(6295):176-178.
15. JJ Iliff, M Wang, Y Liao, BA Plogg, W Peng, et al. A paravascular pathway facilitates CSF flow through the brain parenchyma and the clearance of interstitial solutes, including amyloid beta. Sci Transl Med. 2012; 4(147):147ra111.
16. ET Zhang, CB Inman, and RO Weller. Interrelationships of the pia mater and the perivascular (Virchow-Robin) spaces in the human cerebrum. J Anat. 1990; 170:111-23.
17. H Pollock, M Hutchings, RO Weller, and ET Zhang. Perivascular spaces in the basal ganglia of the human brain: their relationship to lacunes. Journal of anatomy. 1997; 191 (Pt 3):337-46.
18. RO Carare, M Bernardes-Silva, TA Newman, AM Page, JA Nicoll, et al. Solutes, but not cells, drain from the brain parenchyma along basement membranes of capillaries and arteries: significance for cerebral amyloid angiopathy and neuroimmunology. Neuropathol Appl Neurobiol. 2008; 34(2):131-44.
19. T Ichimura, PA Fraser, and HF Cserr. Distribution of extracellular tracers in perivascular spaces of the rat brain. Brain Res. 1991; 545(1-2):103-13.
20. ML Rennels, TF Gregory, OR Blaumanis, K Fujimoto, and PA Grady. Evidence for a 'paravascular' fluid circulation in the mammalian central nervous system, provided by the rapid distribution of tracer protein throughout the brain from the subarachnoid space. Brain Res. 1985; 326(1):47-63.
21. M Arbel-Ornath, E Hudry, K Eikermann-Haerter, S Hou, JL Gregory, et al. Interstitial fluid drainage is impaired in ischemic stroke and Alzheimer's disease mouse models. Acta Neuropathol. 2013; 126(3):353-64.

22. EA Nagelhus and OP Ottersen. Physiological roles of aquaporin-4 in brain. Physiol Rev. 2013; 93(4):1543-62.
23. EA Nagelhus, TM Mathiisen, and OP Ottersen. Aquaporin-4 in the central nervous system: cellular and subcellular distribution and coexpression with KIR4.1. Neuroscience. 2004; 129(4):905-13.
24. E Scemes and DC Spray. Astrocytes: Wiring the Brain. 2011: CRC Press.
25. M Nedergaard, B Ransom, and SA Goldman. New roles for astrocytes: redefining the functional architecture of the brain. Trends Neurosci. 2003; 26(10):523-30.
26. LE Bilston, DF Fletcher, AR Brodbelt, and MA Stoodley. Arterial pulsation-driven cerebrospinal fluid flow in the perivascular space: a computational model. Comput Methods Biomech Biomed Engin. 2003; 6(4):235-41.
27. D Schley, R Carare-Nnadi, CP Please, VH Perry, and RO Weller. Mechanisms to explain the reverse perivascular transport of solutes out of the brain. J Theor Biol. 2006; 238(4):962-74.
28. P Wang and WL Olbricht. Fluid mechanics in the perivascular space. J Theor Biol. 2011; 274(1):52-7.
29. HD Hettiarachchi, Y Hsu, TJ Harris, Jr., R Penn, and AA Linninger. The effect of pulsatile flow on intrathecal drug delivery in the spinal canal. Ann Biomed Eng. 2011; 39(10):2592-602.
30. V Kurtcuoglu, M Soellinger, P Summers, D Poulikakos, and P Boesiger. Mixing and modes of mass transfer in the third cerebral ventricle: a computational analysis. Journal of biomechanics. 2007; 129(5):695-702.
31. J Brettschneider, A Claus, J Kassubek, and H Tumani. Isolated blood-cerebrospinal fluid barrier dysfunction: prevalence and associated diseases. Journal of neurology. 2005; 252(9):1067-73.
32. H Reiber. Flow rate of cerebrospinal fluid (CSF)--a concept common to normal blood-CSF barrier function and to dysfunction in neurological diseases. Journal of the neurological sciences. 1994; 122(2):189-203.
33. V Puy, J Zmudka-Attier, C Capel, R Bouzerar, JM Serot, et al. Interactions between Flow Oscillations and Biochemical Parameters in the Cerebrospinal Fluid. Front Aging Neurosci. 2016; 8.
34. V Kurtcuoglu, M Soellinger, P Summers, K Boomsma, D Poulikakos, et al. Computational investigation of subject-specific cerebrospinal fluid flow in the third ventricle and aqueduct of Sylvius. J Biomech. 2007; 40(6):1235-45.
35. E Sykova and C Nicholson. Diffusion in brain extracellular space. Physiol Rev. 2008; 88(4):1277-340.
36. JE Rash. Molecular disruptions of the panglial syncytium block potassium siphoning and axonal saltatory conduction: pertinence to neuromyelitis optica and other demyelinating diseases of the central nervous system. Neuroscience. 2010; 168(4):982-1008.
37. JC Vardakis, BJ Tully, and Y Ventikos. Exploring the Efficacy of Endoscopic Ventriculostomy for Hydrocephalus Treatment via a Multicompartmental Poroelastic Model of CSF Transport: A Computational Perspective. Plos One. 2013; 8(12).
38. B Tully and Y Ventikos. Cerebral water transport using multiple-network poroelastic theory: application to normal pressure hydrocephalus. Journal of Fluid Mechanics. 2011; 667:188-215.
39. KM Tangen, Y Hsu, DC Zhu, and AA Linninger. CNS wide simulation of flow resistance and drug transport due to spinal microanatomy. J Biomech. 2015; 48(10):2144-54.
40. B Siyahhan, V Knobloch, D de Zelicourt, M Asgari, M Schmid Daners, et al. Flow induced by ependymal cilia dominates near-wall cerebrospinal fluid dynamics in the lateral ventricles. J R Soc Interface. 2014; 11(94):20131189.
41. AW Morris, RO Carare, S Schreiber, and CA Hawkes. The Cerebrovascular Basement Membrane: Role in the Clearance of beta-amyloid and Cerebral Amyloid Angiopathy. Front Aging Neurosci. 2014; 6:251.

42. TM Mathiisen, KP Lehre, NC Danbolt, and OP Ottersen. The perivascular astroglial sheath provides a complete covering of the brain microvessels: an electron microscopic 3D reconstruction. Glia. 2010; 58(9):1094-103.
43. PA Weber, HC Chang, KE Spaeth, JM Nitsche, and BJ Nicholson. The permeability of gap junction channels to probes of different size is dependent on connexin composition and permeant-pore affinities. Biophys J. 2004; 87(2):958-73.
44. GA Rosenberg, WT Kyner, and E Estrada. Bulk flow of brain interstitial fluid under normal and hyperosmolar conditions. Am J Physiol. 1980; 238(1):F42-9.
45. C Nicholson. Diffusion and related transport mechanisms in brain tissue. Reports on Progress in Physics. 2001; 64(7):815-884.
46. CE Johanson, JA Duncan, 3rd, PM Klinge, T Brinker, EG Stopa, et al. Multiplicity of cerebrospinal fluid functions: New challenges in health and disease. Cerebrospinal Fluid Res. 2008; 5:10.
47. NN Haj-Yasein, GF Vindedal, M Eilert-Olsen, GA Gundersen, O Skare, et al. Glial-conditional deletion of aquaporin-4 (Aqp4) reduces blood-brain water uptake and confers barrier function on perivascular astrocyte endfeet. Proceedings of the National Academy of Sciences of the United States of America. 2011; 108(43):17815-20.
48. F Cassot, F Lauwers, C Fouard, S Prohaska, and V Lauwers-Cances. A novel three-dimensional computer-assisted method for a quantitative study of microvascular networks of the human cerebral cortex. Microcirculation. 2006; 13(1):1-18.
49. PS Tsai, JP Kaufhold, P Blinder, B Friedman, PJ Drew, et al. Correlations of neuronal and microvascular densities in murine cortex revealed by direct counting and colocalization of nuclei and vessels. J Neurosci. 2009; 29(46):14553-70.
50. V Williams, RG Grossman, and SM Edmunds. Volume and surface area estimates of astrocytes in the sensorimotor cortex of the cat. Neuroscience. 1980; 5(7):1151-9.
51. B Yang and AS Verkman. Water and glycerol permeabilities of aquaporins 1-5 and MIP determined quantitatively by expression of epitope-tagged constructs in Xenopus oocytes. J Biol Chem. 1997; 272(26):16140-6.
52. EA Nagelhus, ML Veruki, R Torp, FM Haug, JH Laake, et al. Aquaporin-4 water channel protein in the rat retina and optic nerve: polarized expression in Muller cells and fibrous astrocytes. J Neurosci. 1998; 18(7):2506-19.
53. I Ostby, L Oyehaug, GT Einevoll, EA Nagelhus, E Plahte, et al. Astrocytic mechanisms explaining neural-activity-induced shrinkage of extraneuronal space. PLoS Comput Biol. 2009; 5(1):e1000272.
54. C Huang and TE Thompson. Properties of lipid bilayer membranes separating two aqueous phases: determination of membrane thickness. J Mol Biol. 1965; 13(1):183-93.
55. JI Nagy and JE Rash. Connexins and gap junctions of astrocytes and oligodendrocytes in the CNS. Brain Res Brain Res Rev. 2000; 32(1):29-44.
56. RG Thorne and C Nicholson. In vivo diffusion analysis with quantum dots and dextrans predicts the width of brain extracellular space. Proceedings of the National Academy of Sciences of the United States of America. 2006; 103(14):5567-72.
57. AW Morris, RO Carare, S Schreiber, and CA Hawkes. The Cerebrovascular Basement Membrane: Role in the Clearance of beta-amyloid and Cerebral Amyloid Angiopathy. Frontiers in aging neuroscience. 2014; 6:251.
58. WG Robison, Jr., PF Kador, and JH Kinoshita. Retinal capillaries: basement membrane thickening by galactosemia prevented with aldose reductase inhibitor. Science. 1983; 221(4616):1177-9.
59. MA Katz, T Barrette, and M Krasovich. Hydraulic conductivity of basement membrane with computed values for fiber radius and void volume ratio. Am J Physiol. 1992; 263(5 Pt 2):H1417-21.
60. J Satoh, H Tabunoki, T Yamamura, K Arima, and H Konno. Human astrocytes express aquaporin-1 and aquaporin-4 in vitro and in vivo. Neuropathology. 2007; 27(3):245-56.

61. MM Thi, DC Spray, and M Hanani. Aquaporin-4 water channels in enteric neurons. J Neurosci Res. 2008; 86(2):448-56.
62. E Solenov, H Watanabe, GT Manley, and AS Verkman. Sevenfold-reduced osmotic water permeability in primary astrocyte cultures from AQP-4-deficient mice, measured by a fluorescence quenching method. Am J Physiol Cell Physiol. 2004; 286(2):C426-32.
63. S Strohschein, K Huttmann, S Gabriel, DK Binder, U Heinemann, et al. Impact of aquaporin-4 channels on K+ buffering and gap junction coupling in the hippocampus. Glia. 2011; 59(6):973-80.
64. S Vogel. Life in moving fluids : the physical biology of flow. 2nd ed. 1994, Princeton, N.J.: Princeton University Press. xiii, 467 p.
65. HF Cserr, DN Cooper, PK Suri, and CS Patlak. Efflux of radiolabeled polyethylene glycols and albumin from rat brain. Am J Physiol. 1981; 240(4):F319-28.
66. I Szentistvanyi, CS Patlak, RA Ellis, and HF Cserr. Drainage of interstitial fluid from different regions of rat brain. Am J Physiol. 1984; 246(6 Pt 2):F835-44.
67. L Xie, H Kang, Q Xu, MJ Chen, Y Liao, et al. Sleep drives metabolite clearance from the adult brain. Science. 2013; 342(6156):373-7.
68. JJ Iliff, M Wang, DM Zeppenfeld, A Venkataraman, BA Plog, et al. Cerebral arterial pulsation drives paravascular CSF-interstitial fluid exchange in the murine brain. J Neurosci. 2013; 33(46):18190-9.
69. MK Sharp, RD Kamm, AH Shapiro, E Kimmel, and GE Karniadakis. Dispersion in a Curved Tube during Oscillatory Flow. Journal of Fluid Mechanics. 1991; 223:537-563.
70. MP Blaustein, JPY Kao, DR Matteson, and MP Blaustein. Cellular physiology and neurophysiology: Mosby Physiology Monograph Series. 2nd ed. 2012: Elsevier Health Sciences. 337 p.
71. BJ Kirby. Micro- and nanoscale fluid mechanics : transport in microfluidic devices. 2010, New York: Cambridge University Press. xxiii, 512 p.
72. A Reichenbach. Organelle-free cytoplasmic volume fraction of rabbit retinal Muller (glial) cells. J Hirnforsch. 1989; 30(5):513-6.
73. A Popadic, JH Walther, P Koumoutsakos, and M Praprotnik. Continuum simulations of water flow in carbon nanotube membranes. New Journal of Physics. 2014; 16.
74. KP Travis, BD Todd, and DJ Evans. Poiseuille flow of molecular fluids. Physica A. 1997; 240(1-2):315-327.
75. SB Hladky and MA Barrand. Mechanisms of fluid movement into, through and out of the brain: evaluation of the evidence. Fluids and Barriers of the CNS. 2014; 11:26.
76. M Asgari, D de Zélicourt, and V Kurtcuoglu. How astrocyte networks may contribute to cerebral metabolite clearance. Scientific Reports. 2015; 5:15024.
77. K Yoshihara, H Takuwa, I Kanno, S Okawa, Y Yamada, et al. 3D analysis of intracortical microvasculature during chronic hypoxia in mouse brains. Adv Exp Med Biol. 2013; 765:357-63.
78. K Fujikura, J Luo, V Gamarnik, M Pernot, R Fukumoto, et al. A novel noninvasive technique for pulse-wave imaging and characterization of clinically-significant vascular mechanical properties in vivo. Ultrason Imaging. 2007; 29(3):137-54.
79. H Jasak. OpenFOAM: Open source CFD in research and industry. Int J Nav Arch Ocean. 2009; 1(2):89-94.
80. SM Pineda, G Diaz, and CFM Coimbra. Approximation of Transient 1D Conduction in a Finite Domain Using Parametric Fractional Derivatives. J Heat Trans-T Asme. 2011; 133(7).
81. WM Deen. Hindered transport of large molecules in liquid-filled pores. AIChE Journal. 1987; 33(9):1409-1425.
82. M Amiry-Moghaddam, T Otsuka, PD Hurn, RJ Traystman, FM Haug, et al. An alpha-syntrophin-dependent pool of AQP4 in astroglial end-feet confers bidirectional water flow between blood and brain. Proc Natl Acad Sci U S A. 2003; 100(4):2106-11.

83. GT Manley, M Fujimura, T Ma, N Noshita, F Filiz, et al. Aquaporin-4 deletion in mice reduces brain edema after acute water intoxication and ischemic stroke. Nat Med. 2000; 6(2):159-63.
84. ML Rennels, OR Blaumanis, and PA Grady. Rapid solute transport throughout the brain via paravascular fluid pathways. Adv Neurol. 1990; 52:431-9.
85. S Gladdish, D Manawadu, W Banya, J Cameron, CJ Bulpitt, et al. Repeatability of non-invasive measurement of intracerebral pulse wave velocity using transcranial Doppler. Clinical Science. 2005; 108(5):433-439.
86. CA Hawkes, N Jayakody, DA Johnston, I Bechmann, and RO Carare. Failure of perivascular drainage of beta-amyloid in cerebral amyloid angiopathy. Brain Pathol. 2014; 24(4):396-403.
87. DK Binder, MC Papadopoulos, PM Haggie, and AS Verkman. In vivo measurement of brain extracellular space diffusion by cortical surface photobleaching. J Neurosci. 2004; 24(37):8049-56.
88. XM Yao, S Hrabetova, C Nicholson, and GT Manley. Aquaporin-4-deficient mice have increased extracellular space without tortuosity change. Journal of Neuroscience. 2008; 28(21):5460-5464.
89. BJ Jin, H Zhang, DK Binder, and AS Verkman. Aquaporin-4-dependent K(+) and water transport modeled in brain extracellular space following neuroexcitation. J Gen Physiol. 2013; 141(1):119-32.
90. LY Di Marco, E Farkas, C Martin, A Venneri, and AF Frangi. Is Vasomotion in Cerebral Arteries Impaired in Alzheimer's Disease? Journal of Alzheimer's disease: JAD. 2015.
91. SV Frankfort, LR Tulner, JP van Campen, MM Verbeek, RW Jansen, et al. Amyloid beta protein and tau in cerebrospinal fluid and plasma as biomarkers for dementia: a review of recent literature. Current clinical pharmacology. 2008; 3(2):123-31.
92. H Reiber. Proteins in cerebrospinal fluid and blood: barriers, CSF flow rate and source-related dynamics. Restor Neurol Neurosci. 2003; 21(3-4):79-96.
93. H Reiber, B Padilla-Docal, JC Jensenius, and AJ Dorta-Contreras. Mannan-binding lectin in cerebrospinal fluid: a leptomeningeal protein. Fluids and barriers of the CNS. 2012; 9(1):17.
94. H Rosen, KS Sunnerhagen, J Herlitz, C Blomstrand, and L Rosengren. Serum levels of the brain-derived proteins S-100 and NSE predict long-term outcome after cardiac arrest. Resuscitation. 2001; 49(2):183-91.
95. B Engelhardt and L Sorokin. The blood-brain and the blood-cerebrospinal fluid barriers: function and dysfunction. Semin Immunopathol. 2009; 31(4):497-511.
96. SI Rapoport. Passage of proteins from blood to cerebrospinal fluid, in: Neurobiology of Cerebrospinal Fluid 2. Springer; 1983. p. 233-245.
97. JB Winfield, M Shaw, LM Silverman, RA Eisenberg, HA Wilson, 3rd, et al. Intrathecal IgG synthesis and blood-brain barrier impairment in patients with systemic lupus erythematosus and central nervous system dysfunction. Am J Med. 1983; 74(5):837-44.
98. MK Sharief, M Ciardi, and EJ Thompson. Blood-brain barrier damage in patients with bacterial meningitis: association with tumor necrosis factor-alpha but not interleukin-1 beta. J Infect Dis. 1992; 166(2):350-8.
99. H Zetterberg, J Jakobsson, M Redsater, U Andreasson, E Palsson, et al. Blood-cerebrospinal fluid barrier dysfunction in patients with bipolar disorder in relation to antipsychotic treatment. Psychiatry Res. 2014; 217(3):143-6.
100. T Akaishi, K Narikawa, Y Suzuki, S Mitsuzawa, K Tsukita, et al. Importance of the quotient of albumin, quotient of immunoglobulin G and Reibergram in inflammatory neurological disorders with disease-specific patterns of blood–brain barrier permeability. Neurology and Clinical Neuroscience. 2015; 3(3):94-100.
101. M Asgari, D de Zélicourt, and V Kurtcuoglu. Glymphatic solute transport does not require bulk flow. Scientific Reports. 2016; 6:38635.
102. MM Panjabi, T Oxland, K Takata, V Goel, J Duranceau, et al. Articular facets of the human spine. Quantitative three-dimensional anatomy. Spine (Phila Pa 1976). 1993; 18(10):1298-310.

103. MM Panjabi, K Takata, V Goel, D Federico, T Oxland, et al. Thoracic human vertebrae. Quantitative three-dimensional anatomy. Spine (Phila Pa 1976). 1991; 16(8):888-901.
104. M Zaaroor, G Kosa, A Peri-Eran, I Maharil, M Shoham, et al. Morphological study of the spinal canal content for subarachnoid endoscopy. Minim Invasive Neurosurg. 2006; 49(4):220-6.
105. S Gupta, M Soellinger, DM Grzybowski, P Boesiger, J Biddiscombe, et al. Cerebrospinal fluid dynamics in the human cranial subarachnoid space: an overlooked mediator of cerebral disease. I. Computational model. J R Soc Interface. 2010; 7(49):1195-204.
106. TI Yiallourou, JR Kroger, N Stergiopulos, D Maintz, BA Martin, et al. Comparison of 4D phase-contrast MRI flow measurements to computational fluid dynamics simulations of cerebrospinal fluid motion in the cervical spine. PLoS One. 2012; 7(12):e52284.
107. S Gupta, M Soellinger, P Boesiger, D Poulikakos, and V Kurtcuoglu. Three-dimensional computational modeling of subject-specific cerebrospinal fluid flow in the subarachnoid space. J Biomech Eng. 2009; 131(2):021010.
108. NJ Abbott. Evidence for bulk flow of brain interstitial fluid: significance for physiology and pathology. Neurochem Int. 2004; 45(4):545-52.
109. D Schellinger, D LeBihan, SS Rajan, CA Cammarata, NJ Patronas, et al. MR of slow CSF flow in the spine. AJNR Am J Neuroradiol. 1992; 13(5):1393-403.
110. JF Poduslo, GL Curran, TM Wengenack, B Malester, and K Duff. Permeability of proteins at the blood–brain barrier in the normal adult mouse and double transgenic mouse model of Alzheimer's disease. Neurobiology of disease. 2001; 8(4):555-567.
111. RW Cutler, JE Murray, and LR Cornick. Variations in protein permeability in different regions of the cerebrospinal fluid. Exp Neurol. 1970; 28(2):257-65.
112. K Bechter and B Schmitz. Cerebrospinal fluid outflow along lumbar nerves and possible relevance for pain research: case report and review. Croatian medical journal. 2014; 55(4):399-404.
113. K Bechter and H Benveniste. Quinckes' pioneering 19th centuries CSF studies may inform 21th centuries research. Neurology, psychiatry, and brain research. 2015; 21(2):79.
114. S Seyfert and A Faulstich. Is the blood-CSF barrier altered in disease? Acta Neurol Scand. 2003; 108(4):252-256.
115. S Seyfert, S Quill, and A Faulstich. Variation of barrier permeability for albumin and immunoglobulin G influx into cerebrospinal fluid. Clin Chem Lab Med. 2009; 47(8):955-8.
116. A Marmarou, K Shulman, and J LaMorgese. Compartmental analysis of compliance and outflow resistance of the cerebrospinal fluid system. J Neurosurg. 1975; 43(5):523-34.
117. M Gehlen, V Kurtcuoglu, and MS Daners. Patient Specific Hardware-in-the-Loop Testing of Cerebrospinal Fluid Shunt Systems. IEEE Trans Biomed Eng. 2016; 63(2):348-58.

List of publications

1) Asgari, M., de Zélicourt, D., & Kurtcuoglu, V. (2017). Barrier dysfunction or drainage reduction: Differentiating causes of CSF protein increase? This manuscript (chapter 4 of the thesis) has been submitted to the journal of Fluids and Barriers of the CNS.

2) Asgari, M., de Zélicourt, D., & Kurtcuoglu, V. (2016). Glymphatic solute transport does not require bulk flow. Scientific Reports, 6.

3) Asgari, M., de Zélicourt, D., & Kurtcuoglu, V. (2015). How astrocyte networks may contribute to cerebral metabolite clearance. Scientific reports, 5, 15024.

4) Siyahhan, B., Knobloch, V., de Zélicourt, D., Asgari, M., Daners, M. S., Poulikakos, D., & Kurtcuoglu, V. (2014). Flow induced by ependymal cilia dominates near-wall cerebrospinal fluid dynamics in the lateral ventricles. Journal of The Royal Society Interface, 11(94), 20131189.